

The Texas Medical Center Library

DigitalCommons@TMC

The University of Texas MD Anderson Cancer
Center UTHealth Graduate School of
Biomedical Sciences Dissertations and Theses
(Open Access)

The University of Texas MD Anderson Cancer
Center UTHealth Graduate School of
Biomedical Sciences

8-2011

Targeted Multistage Delivery of Nanoparticles to the Bone Marrow

Aman Mann

Follow this and additional works at: https://digitalcommons.library.tmc.edu/utgsbs_dissertations



Part of the [Biomaterials Commons](#), and the [Therapeutics Commons](#)

Recommended Citation

Mann, Aman, "Targeted Multistage Delivery of Nanoparticles to the Bone Marrow" (2011). *The University of Texas MD Anderson Cancer Center UTHealth Graduate School of Biomedical Sciences Dissertations and Theses (Open Access)*. 158.

https://digitalcommons.library.tmc.edu/utgsbs_dissertations/158

This Dissertation (PhD) is brought to you for free and open access by the The University of Texas MD Anderson Cancer Center UTHealth Graduate School of Biomedical Sciences at DigitalCommons@TMC. It has been accepted for inclusion in The University of Texas MD Anderson Cancer Center UTHealth Graduate School of Biomedical Sciences Dissertations and Theses (Open Access) by an authorized administrator of DigitalCommons@TMC. For more information, please contact digitalcommons@library.tmc.edu.

The
TMC LIBRARY
Health Sciences Resource Center

TARGETED MULTISTAGE DELIVERY OF NANOPARTICLES TO THE BONE
MARROW

By

Aman Preet Singh Mann, M.S.

APPROVED:

Mauro Ferrari, Ph.D. Supervisory Chair

David Gorenstein, Ph.D.

Steven Norris, Ph.D.

Gabriel Lopez-Berestein, M.D.

Takemi Tanaka, Ph.D.

APPROVED:

Dean, The University of Texas
Graduate School of Biomedical Sciences at Houston

**TARGETED MULTISTAGE DELIVERY OF NANOPARTICLES TO THE BONE
MARROW**

A

DISSERTATION

Presented to the Faculty of

The University of Texas Health Science Center at Houston

and

The University of Texas M. D. Anderson Cancer Center

Graduate School of Biomedical Sciences

in Partial Fulfillment

of the Requirements

for the Degree of

DOCTOR OF PHILOSOPHY

by

Aman Preet Singh Mann, M.S.

Houston, Texas

August, 2011

Dedication

To my grandfather, Nar Singh Mann

To my father Ranjit

To my mother Jatinder

To my lovely brother Darsh

To my beloved wife Rimmy

Acknowledgements

I would first like to express my gratitude to Dr. Mauro Ferrari for his unparalleled guidance and support that was crucial for the development of my project. His mentorship and inspiration over these years has been invaluable, and has molded every part of the researcher that I am today. I would also like to thank Dr. Takemi Tanaka for her continuous support and direction in all aspects of my research.

I would like to express many thanks to my committee members, Drs. David Gorenstein, Gabriel Lopez-Berestein, Steven Norris, and Takemi Tanaka for their time, and feedback that has helped my project reach to fruition.

I would like to thank the Graduate School of Biomedical Sciences and especially, Dr. Victoria Knutson for her helpful advice and Bunny Perez for always having their doors open to me to seek assistance when needed.

I would to thank my colleagues and friends, Adam Labaff and Erika Spaeth who helped me keep a balanced life and for all the fun things we did together. I would like to thank my wonderful roommate Rohan Bhavane for his patience and support outside of the laboratory.

Lastly, I would like to thank my family for their unconditional love, support and encouragement. My parents Jatinder and Ranjit Mann have always supported my aspirations. Thanks mom. Thanks dad. My brother Darsh has always motivated me and kept me focused and persistent towards my goal. A special thanks to my wife who recently joined me in this journey and has been beyond patient, understanding, and wholeheartedly supportive of this endeavor.

TARGETED MULTISTAGE DELIVERY OF NANOPARTICLES TO THE BONE MARROW

Publication No._____

Aman Preet Singh Mann, M.S.

Supervisory Professor: Mauro Ferrari, Ph.D.

Bone marrow is a target organ site involved in multiple diseases including myeloproliferative disorders and hematologic malignancies and metastases from breast and prostate. Most of these diseases are characterized with poor quality of life, and the treatment options are not very specific due to lack of delivery mechanisms which results in dose limitation to protect the healthy hematopoietic cells. Therefore, there is a critical need to develop effective therapeutic strategies that allow for selective delivery of therapeutic payload to the bone marrow. Nanotechnology-based drug delivery systems provide the opportunity to deliver drugs to the target tissue while decreasing exposure to normal tissues. E-selectin is constitutively expressed on the bone marrow vasculature, but almost absent in normal vessels, and therefore, E-selectin targeted drug delivery presents an ideal strategy for the delivery of therapeutic nanoparticles to the bone marrow.

The objective of this study was to develop a novel bone marrow targeted multistage vector (MSV) via E-selectin for delivery of therapeutics and imaging agents. To achieve this goal, Firstly, an E-selectin thioaptamer (ESTA) ligand was identified through a two-step screening from a combinatorial thioaptamer library. Next, ESTA-conjugated MSV (ESTA-MSV) were developed and evaluated for their stability and binding to E-selectin expressing endothelial cells.

Different types of nanoparticles including liposomes, quantum dots, and iron oxide nanoparticles were loaded into the porous structure of ESTA-MSV. *In vivo* targeting experiments demonstrated 8-fold higher accumulation of ESTA-MSV in the mouse bone marrow as compared to non-targeted MSV. Furthermore, intravenous injection of liposomes loaded ESTA-MSV resulted in a significantly higher accumulation of liposome in the bone marrow space as compared to injection of non-targeted MSV or liposomes alone. Overall this study provides first evidence that E-selectin targeted multistage vector preferentially targets to bone marrow vasculature and delivers larger amounts of nanoparticles. This delivery strategy holds potential for the selective delivery of large amounts of therapeutic payload to the vascular niches in the bone marrow for the treatment of bone marrow associated diseases.

Table of Contents

Dedication	iii
Acknowledgements	iv
Abstract	v
List of Figures	xi
List of Tables.....	xiii
Abbreviations	xiv
Chapter 1. Introduction	1
1.1 Bone marrow	1
1.1.1 Composition, function and structure	1
1.1.2 Anatomical properties of the bone marrow	2
1.1.3 Physiological properties of the bone marrow.....	4
1.1.4 Bone marrow associated diseases.....	4
1.1.5 Treatment of BM associated diseases	5
1.2 Nanotechnology	6
1.2.1 Nanomedicine.....	9
1.2.2 Passive vs. Active Targeting	10
1.2.3 Multistage Drug Delivery	14
1.2.3.1 Rational Design of MSVs	18
1.2.3.2 Loading of nanoparticles into MSVs	21
1.2.3.3 Biodegradation of MSVs	23
1.2.3.4 Biocompatibility of MSV	25
1.3. Adhesion molecules	26

1.3.1 E-selectin (CD62E, ELAM-1).....	26
1.3.2 Thioated Aptamer ligands.....	31
1.4 Objectives and Hypothesis.....	35
Chapter 2. Materials and Methods	37
2.1 Cell culture	37
2.2 Development of ES-Endo cells	37
2.3 Screening of E-selectin thioaptamer (ESTA-1)	40
2.3.1 Synthesis of thioaptamer library	40
2.3.2 Combinatorial selection of thioaptamers	41
2.3.3 TA binding to Endothelial cells	42
2.4 Hybridoma isolation.....	42
2.5 Cell viability studies.....	43
2.6 Development of Multistage vectors (MSVs).....	43
2.6.1 Fabrication of MSVs	43
2.6.2 Surface modification and characterization of MSVs	43
2.7 Conjugation of ESTA to MSV	44
2.8 Infrared Spectroscopy	45
2.9 Flow cytometry	45
2.10 Endothelial cell adhesion studies	46
2.11 Loading of nanoparticles into ESTA-MSV.....	46
2.12 Immunofluorescence.....	47
2.13 Animal studies.....	48
2.13.1 Animal tumor models.....	48
2.13.2 Targeting studies	48
2.14 Silicon content analysis.....	48

2.15 Statistical analysis	49
Chapter 3. Experimental Results.....	50
3.1. Properties of MSV	50
3.1.1 Physico-chemical properties of MSV	50
3.1.2 Biodistribution and biodegradation of MSV	54
3.1.3 Sustained delivery of siRNA contained in MSV	58
3.1.4 Biocompatibility of MSV loaded EphA2-siRNA.....	63
3.2. Identification of E-selectin thioaptamer	65
3.2.1 Synthesis of thioaptamer library	65
3.2.2 Screening with recombinant E-selectin protein	66
3.2.3. Cell-based TA screening	71
3.2.3.1 Development of E-selectin inducible endothelial system	71
3.2.3.2 TA selection using E-selectin inducible endothelial cells	79
3.2.4 Characterization of ESTA-1	87
3.2.5 Evaluation of binding affinity of ESTA-1 to E-selectin	89
3.2.6 ESTA-1 binding to vascular E-selectin <i>in vivo</i>	92
3.2.7 ESTA-1 binding to human tumor vasculature.....	97
3.2.8 Effect of ESTA-1 binding on cell adhesion	100
3.2.9 Effect of ESTA-1 on cell viability.....	100
3.3 Development of bone marrow targeted MSV	104
3.3.1 Conjugation and characterization of ESTA-MSV.....	104
3.3.2 Serum stability of ESTA-MSV.....	109
3.3.3 Adhesion of ESTA-MSV to E-selectin expressing endothelial cells	111
3.3.4 Development of ESTA-MSV loaded with nanoparticles	113
3.3.5 BM targeting of ESTA-MSV	116

Chapter 4. Discussion	120
4.1 Future work and directions.....	128
References	129
Vita	145

List of Figures

Figure 1. Vascular architecture of the bone marrow.....	3
Figure 2. Nanoscale size range relative to other familiar objects.	7
Figure 3. Different targeting strategies employed for drug delivery.	13
Figure 4. Three generation of nanovectors.....	15
Figure 5. Different types of MSVs.....	17
Figure 6. Steps in the vascular journey of a circulating particle.....	20
Figure 7. Loading of nanoparticles into MSV.....	22
Figure 8. Degradation kinetics of MSVs	24
Figure 9. Function of E-selectin in recruitment of circulating cells.....	29
Figure 10. E-selectin expression on bone marrow endothelium.....	30
Figure 11. Structure of thioaptamers: phosphate backbone substitution.....	34
Figure 12. Electrostatic surface of E-selectin protein.	34
Figure 13. Schematic outline of the fabrication protocol for MSV.....	51
Figure 14. SEM images of porous MSVs with different magnifications.	52
Figure 15. Size distribution of MSVs.....	53
Figure 16. Biodistribution of MSV.	55
Figure 17. Biodegradation of MSV.....	56
Figure 18. <i>In vivo</i> degradation of MSVs.....	57
Figure 19. Liposome loading into MSVs.	58
Figure 20. Systemic delivery of EphA2-siRNA using MSV.	60
Figure 21. Effect of sustained siRNA delivery on angiogenesis	61
Figure 22. Cytokine analysis of MSV loaded liposome-siRNA.	64
Figure 23. Schematic representation of the process to screen thioaptamers.....	67
Figure 24. ClustalW alignment of the selected sequences after 10 th round.	68

Figure 25. Cladogram of the selected sequences after round 10.....	69
Figure 26. Common sequence motifs among 14 TA candidates.....	70
Figure 27. Construction of E-selectin expression vector.	73
Figure 28. Immunofluorescence of E-selectin in endothelial cells.....	75
Figure 29. Development of tet-on E-selectin inducible endothelial cells.....	77
Figure 30. Doxycycline inducible E-selectin expression in ES-Endo.....	78
Figure 31. E-selectin dependent binding of ESTA-1.....	83
Figure 32. Competitive E-selectin binding of ESTA-1 and E-selectin antibody.	85
Figure 33. Colocalization of E-selectin expression and ESTA-1 binding.....	86
Figure 34. ESTA-1 sequence and the MFOLD predicted secondary structure.	88
Figure 35. Evaluation of binding affinity of ESTA-1 to E-selectin..	90
Figure 36. <i>In vivo</i> binding of ESTA-1 to bone marrow vasculature.....	94
Figure 37. <i>In vivo</i> binding of ESTA-1 to tumor vasculature	95
Figure 38. ESTA-1 binding to the human tumor vasculature.....	98
Figure 39. Effect of ESTA-1 binding on cell adhesion and cell viability.....	102
Figure 40. Conjugation of ESTA-1 to MSV.....	106
Figure 41. Physico-chemical characteristics of ESTA-MSV.	107
Figure 42: Stability of ESTA-MSV under physiological conditions.....	110
Figure 43. E-selectin dependent ESTA-MSV adhesion to endothelial cells..	112
Figure 44. Nanoparticle loading into ESTA-MSV.....	114
Figure 45. <i>In vivo</i> distribution of ESTA-MSV in mice.....	117

List of Tables

Table 1. List of primers	39
Table 2. Comparison of TA binding to E-selectin expressing ES-Endo.....	83

Abbreviations

ATCC American Type Culture Collection

APTES 3'-aminopropyltriethoxysilane

DOPC 1,2-dioleoyl-sn-glycero-3-phosphocholine

EDAC 1-Ethyl-3-[3-dimethylaminopropyl]carbodiimide hydrochloride

EGF epidermal growth factor

ELAM-1 endothelial-leukocyte adhesion molecule 1

ESTA-1 E-selectin thioaptamer 1

FACS flow assisted cell sorting

FBS fetal bovine serum

FTIR fourier transform infrared spectroscopy

GFP green fluorescent protein

GM-CSF Granulocyte-Macrophage Colony Stimulating Factor

ID injected dose

ION iron oxide nanoparticles

IV intravenous

MSV multistage vector

NP nanoparticle

PBS phosphate buffer saline

QD quantum dots

RFP red fluorescent protein

RPMI Roswell Park Institute medium

RT room temperature

SEM scanning electron microscope

siRNA silencing RNA

sle^a sialyl lewis a

sle^x sialyl lewis x

TNF- α tumor necrosis factor α

β -gal beta galactosidase

Chapter 1. Introduction

1.1 Bone marrow

1.1.1 Composition, function and structure

The bone marrow (BM) is a loose connective tissue within the central cavities of the bones of the body. BM is a richly cellular and a highly vascular organ and one of the largest organs in the body. BM is the major hematopoietic organ and a primary lymphoid tissue that is responsible for the production of hematopoietic cells. The cellular composition of BM consists of

1. Precursor and mature blood cells

- Hematopoietic stem cells and precursor blood cells
- Blood cells - erythrocytes, leukocytes, granulocytes, lymphocytes and platelets

2. Stromal cells

- Osteoclasts
- Osteoblasts
- Endothelial cells
- Fibroblasts
- Adipocytes
- Macrophages

The cellularity and vascularity of BM can change rapidly in response to various physiological and pathological stimuli. In addition to its prime hematopoietic activity, bone marrow has distinct phagocytic and endocytic function due to the presence of macrophages and endothelial cells delineating its

sinuses, respectively. However, deeper understanding of the anatomical and physiological characteristics of the bone marrow is a prerequisite for achieving efficient delivery of therapeutics to the bone marrow.

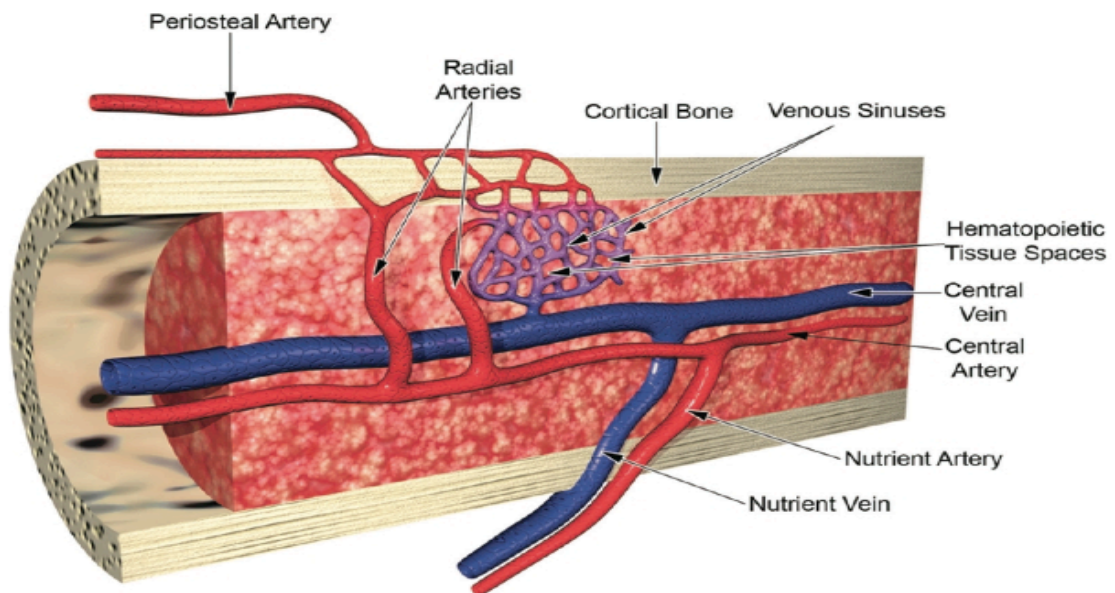
1.1.2 Anatomical properties of the bone marrow

The foremost characteristic of bone marrow organization is its vascular arrangement. The bone marrow is divided into wedge-shaped hematopoietic compartments filled with proliferating and differentiating blood cells in connective tissue matrices bordered by specialized vascular structure known as venous sinuses (1). The vascular system of marrow consists of venous sinuses, veins, and arteries. The major arterial supply of the BM in a long tubular bone is the nutrient artery that runs in the central longitudinal axis. The marrow does not have any lymphatics. The vascular arrangement provides a high number of small vessels and sinuses at the periphery of the bones, and, as a result, hematopoiesis is most active at these peripheries. The sinus wall forms a barrier between the hematopoietic compartment and the circulation and has three distinct components.

1. Endothelial cells that form the inner layer
2. Adventitial cells that form the outer discontinuous layer
3. A discontinuous basal lamina

Figure 1. Vascular architecture of the bone marrow. Presence of extensively distributed microvessels comprising of venous sinuses is characteristic of BM. The major arterial supply is the nutrient artery that runs in the central longitudinal axis.

Reproduced by permission from Toxicologic Pathology, Travlos G. 2006 (1), copyright Society of Toxicologic Pathology (2006).



1.1.3 Physiological properties of the bone marrow

Changes in the blood flow on both a volume and velocity basis have been shown to influence the delivery of drug carriers to any specific site. Due to a variation in the content of the red marrow, there is a considerable variation in the amount of blood flowing through the marrow (2). The blood flow in the marrow can also be altered experimentally by treating animals with phenylhydrazine or acetylcholine (3). However, it has been noted that the average hydrodynamic shear in BM micro vessels is lower than in most other organs (4) to maximize the exchange and transport of cells across the hematopoietic spaces. This property of lower shear rates can be an advantageous in selective delivery of drug carriers to the BM.

1.1.4 Bone marrow associated diseases

Based on the given importance of this organ, damage to the hematopoietic and/or phagocytic components of this multifunctional organ can negatively impact the physiology of the body.

1. For example, a number of pathogenic microorganisms, such as *Mycobacterium bacilli*, *Brucellosis*, etc., can invade bone marrow and can cause undesirable effects such as anemia, leukopenia and chronic infections (5).
2. Bone is one of the most common sites of metastasis originating from primary tumors from the breast or prostate causing severe bone pain, pathological fractures, spinal cord compression and hypercalcemia (6). Bone metastasis frequently occurs in metastatic breast cancer patients

(60 to 80 %) and is associated with poor prognosis (5 year survival rate < 20%) and low quality of life (6).

3. Myeloproliferative disorders for e.g. chronic myelogenous leukemia (CML) characterized by an overproduction of one or more types precursor cells originating in the BM (7).
4. Immune deficiency disorders are associated with a loss of precursor cells in the BM (8).
5. Multiple myeloma characterized as the cancer of the plasma cells originates in the BM (9),
6. Lastly, a large number of anti-neoplastic drugs and therapeutic agents that lack cell specific recognition result in bone marrow toxicity such as myelosuppression (10). This results in maximum tolerated dose (MTD) based therapy, which is less effective against diseases such as cancer.

1.1.5 Treatment of BM associated diseases

Current treatment options for BM diseases associated are limited and consist of either cytotoxic chemotherapy or bone marrow transplantation. Chemotherapy is dose limited due to toxic effects on healthy cells and unfortunately, only about 30 percent of patients are candidates for transplantation because of age limitations or lack of a suitable HLA-matched donor [7]. These facts collectively highlight an urgent need for effective delivery of therapeutic agents for the treatment of diseases of the bone marrow and for the protection and stimulation of the inherent physiological function of this organ.

The ability of the bone marrow to uptake particulates from the bloodstream has opened up an opportunity for delivery of therapeutic agents efficiently by means of drug delivery carriers. In conjunction with the physiological and anatomical characteristics of the bone marrow, two types of BM targeting strategies have been developed. Porter et al., showed a passive targeting approach in which microspheres coated with a copolymer evaded liver and spleen uptake and accumulated in the BM (11). This occurred mainly due to the highly branched and sinusoidal nature of the BM vasculature and the phagocytic uptake. Recently, a targeted therapy using humanized monoclonal antibody against RANK ligand (Denosumab) was approved by the FDA for treatment of osteoporosis and bone metastases (12, 13). Denosumab inhibits the RANK ligand interaction with RANK receptor on precursor osteoclasts, and blocks the osteoclast maturation, and inhibits bone resorption a pathological condition during bone metastases. Targeted therapy comprising of this humanized antibody is extremely expensive (14) and such forms of targeting suffer from limitations in terms of their specificity to the BM organ leading to low overall accumulation in the organ. Therefore, a novel strategy for the delivery of drugs to the BM is needed for further enhancing their therapeutic efficacy.

1.2 Nanotechnology

In 1959, Nobel Laureate Richard Feynman gave his famous lecture titled “There’s plenty of room at the bottom” prompting the research community to visualize things at the sub-atomic scale. The culmination of his vision occurred through the field of nanotechnology, which refers to the design, characterization,

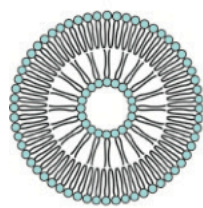
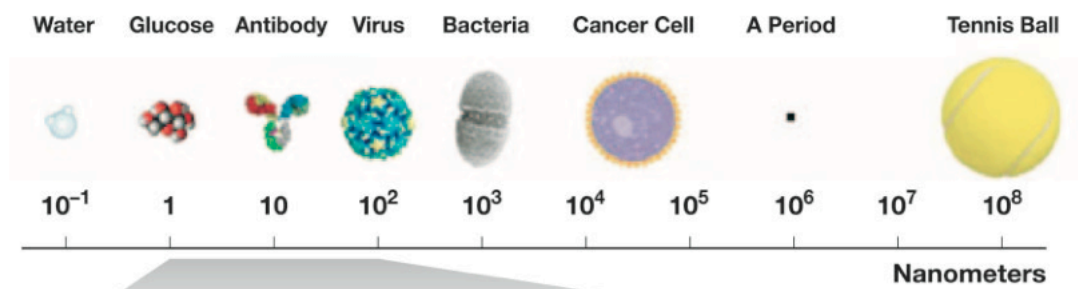
and application of systems in the nanoscale range (1-100 nm). For any device to be considered nanotechnological, it has to be man-made comprising of crucial components in the nanoscale range (15). Additionally, it is equally necessary that the device possess novel properties that emerge due to its nanoscale dimension. These properties could include mechanical, thermal, electrical, magnetic, and optical properties. Nanoparticles, for example, take the advantage of their dramatically increased surface area to volume ratio. For perspective, nanoscale is comparable in dimensions to the interatomic distances in crystalline lattices and is illustrated with respect to other familiar things in figure 2.

Although the full potential of nanotechnology is just beginning to be realized, the following fields have been impacted by nanotechnology

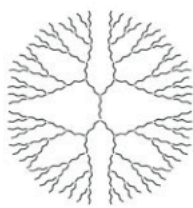
1. Information and communication
2. Medicine
3. Chemistry and environment
4. Energy
5. Consumer goods

Figure 2. Nanoscale size range relative to other familiar objects. The nanoscale ranges between 1-100 nm. Nanoscale devices are smaller than human cells and are similar in size to biological macromolecules such as enzymes, viruses etc. Some commonly used nanotechnology based platforms existing in this range are also presented here.

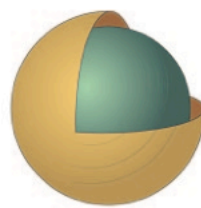
Reproduced with permission from Journal of Leukocyte Biology, McNeil S, 2005. (16), Copyright Society for Leukocyte Biology (2005).



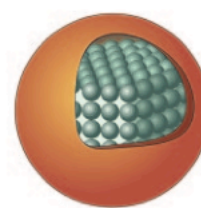
Liposome



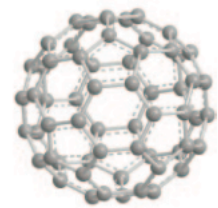
Dendrimer



Gold Nanoshell



Quantum Dot



Fullerene

1.2.1 Nanomedicine

The application of nanotechnology in the field of medicine is termed as nanomedicine. Nanomedicine is an emerging field that offers extraordinary and far-reaching implications for the biomedical applications such as detection, diagnosis and treatment of critical medical conditions including cancer (17), cardiovascular diseases (18), tissue repair (19), and for the improvement of human health (20). The limitless possibilities offered by nanomedicine could possibly open the door for the personalization of medicine for improved patient outcomes (21).

For commonly used medications, multiple different routes are used including topical, local and systemic administration. While systemic delivery such as oral and intravenous routes of administration is the most common, each has serious disadvantages where an effective concentration larger than clinical dose is often required due to rapid clearance of the drug and lack of targeting. For this reason, the maximum effectiveness of the drug is limited. Any injected therapeutic agent encounters multiple obstacles termed as bio-barriers that adversely impact its ability to reach the intended destination at the desired concentration (22). These bio-barriers include physiological barriers such as epithelial/endothelial membranes, reticulo-endothelial system and biophysical barriers such as interstitial pressure gradients, and transport across extracellular matrix. For instance in cancer, one of the major issues surrounding the chemotherapeutic treatment of solid tumors is the bioavailability of the drug at the tumor site. When quantified the drug concentration in a tumor corresponds to only 0.001% of the injected dose, permitting the overwhelming majority of the drug to be systemically dispersed leading to deleterious effects (23).

Nanomedicine holds promise in the development of clinically applicable and biocompatible materials for accurate delivery of therapeutics and imaging tracers by negotiating these biological barriers (24). Nanotechnology based drug delivery systems promise to expand the therapeutic window of drugs by increasing delivery to the target tissue and decreasing drug exposure to normal tissues (17). Some of the established nanoparticle platforms for nanomedicine are represented in figure 2.

1.2.2 Passive vs. Active Targeting

Nanotechnology based therapeutics currently approved by the FDA are either topical, local, or systemic application based on passive targeting mechanism. The progress of clinical translation of novel nano-delivery methods has been rather slow as evidenced by only a few nanoparticles that have obtained FDA approval in the past few decades (Doxil®, Abraxane™). The first generation nanoparticle drug, Doxil is a liposomal formulation of doxorubicin, which leads to improved drug accumulation in the tumors through passive targeting. Similarly, albumin bound paclitaxel formulation also termed as Abraxane has shown drastic improvement in therapeutic efficacy due to improved solubility over Taxol injection. Passive targeting relies on the enhanced permeation and retention (EPR) effect through fenestrations for diffusion into the diseased tissue (25). Due to the changes in the microenvironment in the diseased tissue, the permeability of the vasculature is enhanced due to the presence of sinusoids or fenestrations (Fig. 3). Since nanoparticles such as Doxil are smaller in size than the size of these fenestrations, they can

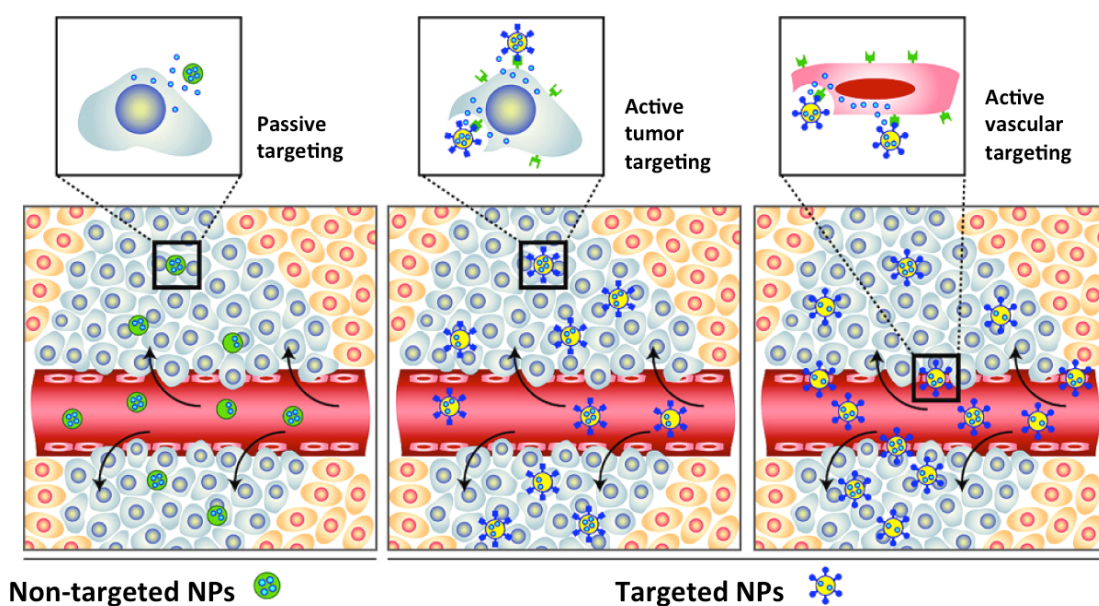
extravasate into the diseased tissue leading to increased accumulation. However, the limitation of passive delivery strategy is that size and location of fenestration and sinusoids are not very specific to the diseased tissue and may result in significant non-specific uptake of circulating nanoparticles in healthy organs. Thus, an active area of research involves functionalization of nanoparticles with targeting moieties that identify and bind to receptors overexpressed on or around the diseased sites, consequently maximizing localization and accumulation in the disease area (Figure 3) (17). This second-generation of nanoparticles based on active targeting through biological recognition of specific antigens on the surface of diseased cells promises to further improve the therapeutic efficacy by enhancing the retention of nanoparticles within the diseased site while minimizing side effects associated with a potential off targeting (Fig. 3). Nevertheless these delivery strategies still primarily rely on extravasation of delivery carriers from discontinuous vessels where the size of openings varies depending on the stage of the disease and location of the tumor (26). Furthermore, high interstitial pressure in the tumor reduces the probability of extravasation of nanoparticles from the vessel into the tumor tissue. Thus, developing novel drug delivery strategies that are independent of vasculature leakiness has been an area of active research.

In this regard, vasculature is attractive target for delivery of therapeutic and imaging contrast agents (27). For example in the case of cancer or inflammation, the vasculature undergoes significant phenotypic changes in response to inflammatory and/or angiogenic stimuli during carcinogenesis. This is evident based on the presence of specific endothelial markers such as cellular adhesion molecules, including E-selectin (28), ICAM (29), integrin $\alpha_v\beta_5$ (30-32),

and VEGFR-2 (33) expression is elevated on the surface of the endothelial cells. This significant difference in expression of surface receptor proteins between normal and tumor endothelium make tumor associated vasculature an attractive target for drug delivery and provide an excellent rationale for therapeutic exploitation (34, 35).

Figure 3. Different targeting strategies employed for drug delivery. Passive (left), active (middle) and active vascular targeting (right). During passive targeting the nanoparticles (NPs) extravasate through the permeable openings in the tumor endothelium. This process can be further improved by active targeting of the NPs to receptors on the tumor cells. In active vascular targeting, nanoparticles favor binding to receptors overexpressed on tumor endothelium, enhancing their accumulation in tumor tissue.

Adapted with permission from ACS Nano, Farokhzad et al, 2009 (25). Copyright American Chemical Society (2009).



Having introduced the first two generations of nanoparticles, it is clear that their ability to negotiate biological barriers and carry drug payload to the desired sites offers multiple therapeutic advantages. However, to add further functionality and another dimension of manipulation to these existing carriers, a third generation of nanocarrier comprising of multiple components is presented here that has the potential to revolutionize the delivery of therapeutics by distributing the tasks of bio-barrier avoidance, targeting, and therapeutic effect among different stages.

1.2.3 Multistage Drug Delivery

Our laboratory has recently developed a novel multistage drug delivery strategy, capable of multiple functions such as navigating biological barriers encountered by nanoparticles and maximizing site-specific localization and release of therapeutics therein. This platform comprises of nanoporous silicon particles that can be loaded with different payload of nanoparticles including therapeutic and imaging agents (36). The rationale for this approach is that MSVs shoulder the burden of efficiently transporting, shielding, and controlling the rate of release of the nanoparticle payload. A schematic describing this concept is presented in Fig.4.

MSVs are fabricated using well-established lithographic techniques for a precise control of shape, size, and porosity (37, 38). The outer dimension of the MSVs can be altered from 500 nm to 20 μ m in size with different shapes and the mean pore size ranges from 5 nm to 80 nm, and the porosity ranges from 40% to 80% (36, 37) (Fig. 5).

Figure 4. Three generation of nanovectors. First generation of nanovectors is based on passive targeting (*top*). Second generation comprises of active targeting through biological recognition of targets (*middle*). Third generation consists of multifunctional delivery systems that comprises of different components such as the MSV (*bottom*). *Reproduced with permission from Pharmacological Research, Sakamoto et al, 2010 [6], copyright Elsevier (2010).*

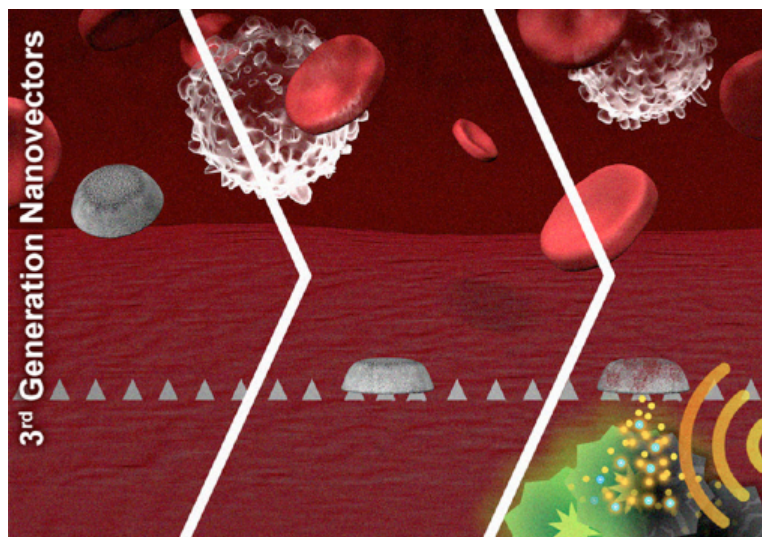
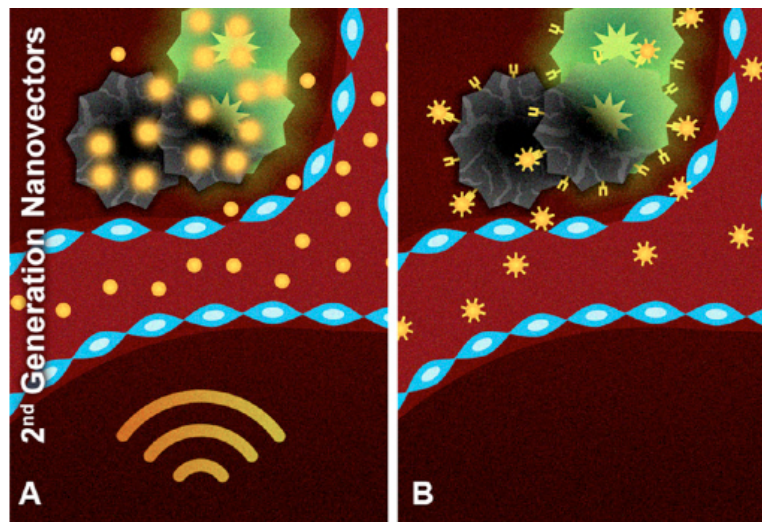
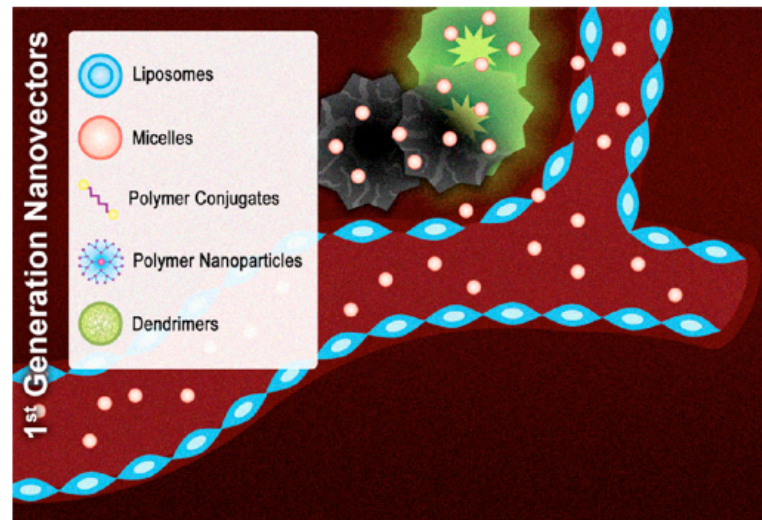
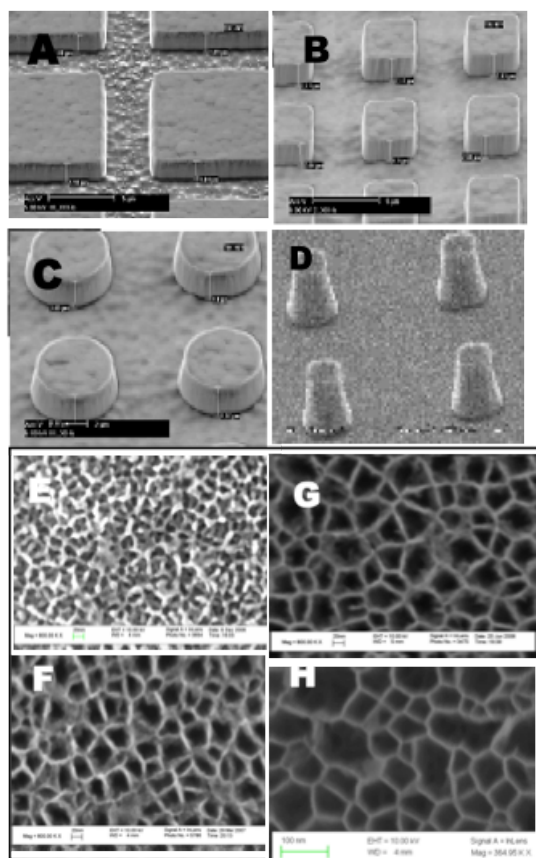


Figure 5. Different types of MSVs. SEM images of different shapes of MSVs (A-D) and different porous characteristics (E-H). List of different geometries possible to microfabricate (table)



Shape	Dimension	Volume μm^3
Hemispherical	Outer Diameter	5.0
	3 μm	1.5
	2.1 μm	0.80
	1.6 μm	0.17
	1.0 μm	
Disk	Diameter x Thickness	5.0
	3 x 0.71 μm	1.5
	2 x 0.36 μm	0.80
	1.5 x 0.45 μm	0.17
	0.7 x 0.44 μm	
Cylindrical	Diameter x Height	5.0
	1.5 x 2.8 μm	1.5
	1 x 1.9 μm	0.79
	1 x 1 μm	0.17
	0.7x 0.44 μm	
Rod	Length x Width x Height	5.0
	=	1.5
	2.2 x 1.5 x 1.5 μm	0.80
	1.5 x 1 x 1 μm	0.17
	1.2 x 1 x 0.67 μm	
	0.7 x 0.7 x 0.35 μm	

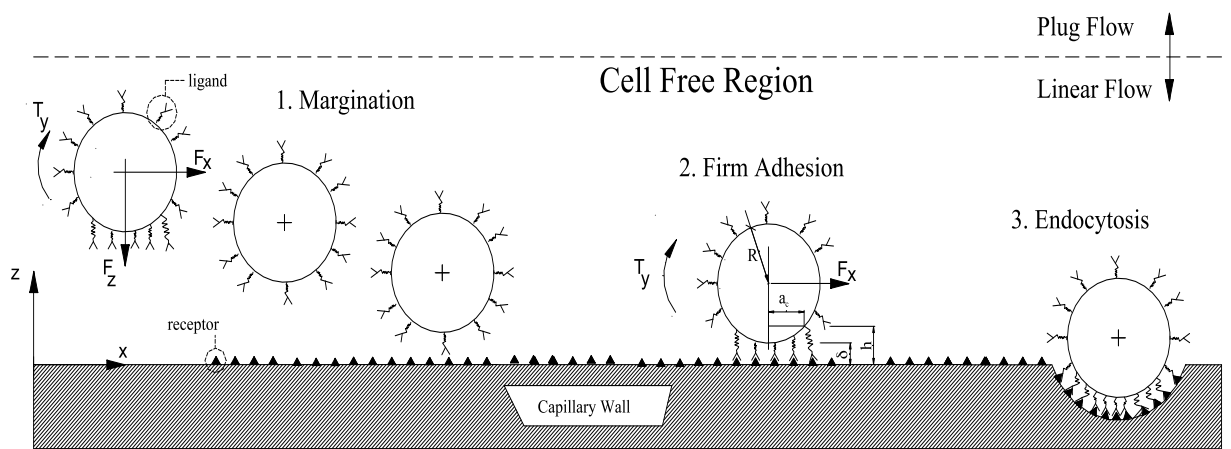
1.2.3.1 Rational Design of MSVs

From a mathematical point of view, the vascular ‘journey’ of any systemically injected particle can be broken down into three events: (i) margination dynamics, (ii) firm adhesion and (iii) control of internalization. *Margination dynamics* is the drifting of nanovectors towards the blood vessel walls. *Firm adhesion* is the ability of a nanovector to recognize a vascular biological target and attach firmly at the blood vessels withstanding the hydrodynamic forces and *endocytosis* is referred to the ability of an adherent nanovector to control cellular uptake (Fig. 6).

Combining together *in silico* mathematical modeling with *in vitro* and *in vivo* experimental validation, the MSVs have been designed to possess the geometry to enhance the probability for margination and adhesion to the vascular endothelium and subsequent cellular uptake. Using a parallel plate flow chamber under controlled hydrodynamic conditions, particles of different shapes were analyzed and the non-spherically shaped particles drifted laterally within the blood flow, thus increasing the probability of interacting with the blood vessel walls, and facilitating the search for specific vascular targets as compared to spherical particles (39, 40). Furthermore, oblate spherical particles that resemble platelets in terms of their geometry showed firm adherence to the vessel wall under flow conditions as compared to spherical particles for the same number of ligand-receptor bonds (41). And lastly, the rate of internalization of particles by cells can be adjusted by controlling the aspect ratio of the particle, as non-spherical particles resist internalization to a greater extent than spherical particles (42). Therefore, depending on the biological properties of the target tissue, a nanoparticle can be selected to have the geometrical and physical

properties to optimize adhesion and cellular uptake or a combination thereof
(43).

Figure 6. Steps in the vascular journey of a circulating particle. *Margination dynamics* is the drifting of nanovectors towards the blood vessel walls. *Firm adhesion* is the ability of a nanovector to recognize a vascular biological target and attach firmly at the blood vessels withstanding the hydrodynamic forces. *Endocytosis* is referred to the ability of an adherent nanovector to control cellular uptake.

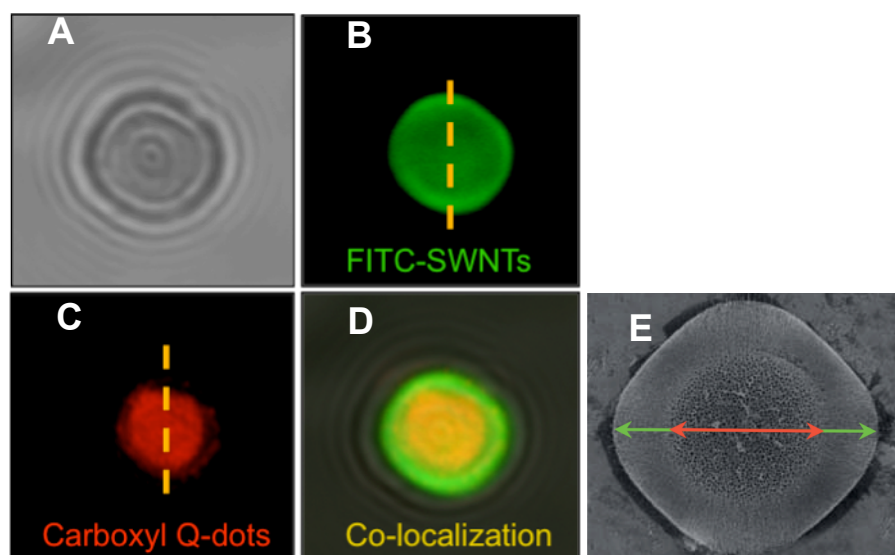


1.2.3.2 Loading of nanoparticles into MSVs

MSVs can be loaded with various types of nanovector construct within the approximate diameter range of 5–100 nm. Depending on the pore size, different types and amount of nanoparticles can be loaded including labeled nanoliposomes, gold nanoparticles, iron oxide nanoparticles, Quantum dots (Q-dot) and carbon nanotubes (SWNTs) (36) (Fig. 7). Once a nanoparticle payload is incorporated into the porous structure of the MSVs, factors governing the release of nanoparticles include MSV degradation rates, polymeric coating, and nanoparticle design strategies (e.g., environmentally sensitive cross-linking techniques with pH, temperature, and/or enzymatic triggers). In addition, the surface of the MSV can be chemically modified with different functional groups, which allows for subsequent bioconjugation of ligand molecules for a site-specific release of the payload for a desirable period.

Figure 7. Loading of nanoparticles into MSV. Bright field confocal microscopy of a single MSV (A). Confocal image showing MSV loaded with single walled nanotubes (green) (B), Quantum-dots (red) (C) and double loading (D). SEM image of MSV, green and red arrows show the spatial distribution of fluorescence (E).

Reproduced with permission from Nature Nanotechnology, Tasciotti et al, 2008 (36). Copyright Nature Publishing Group (2008).

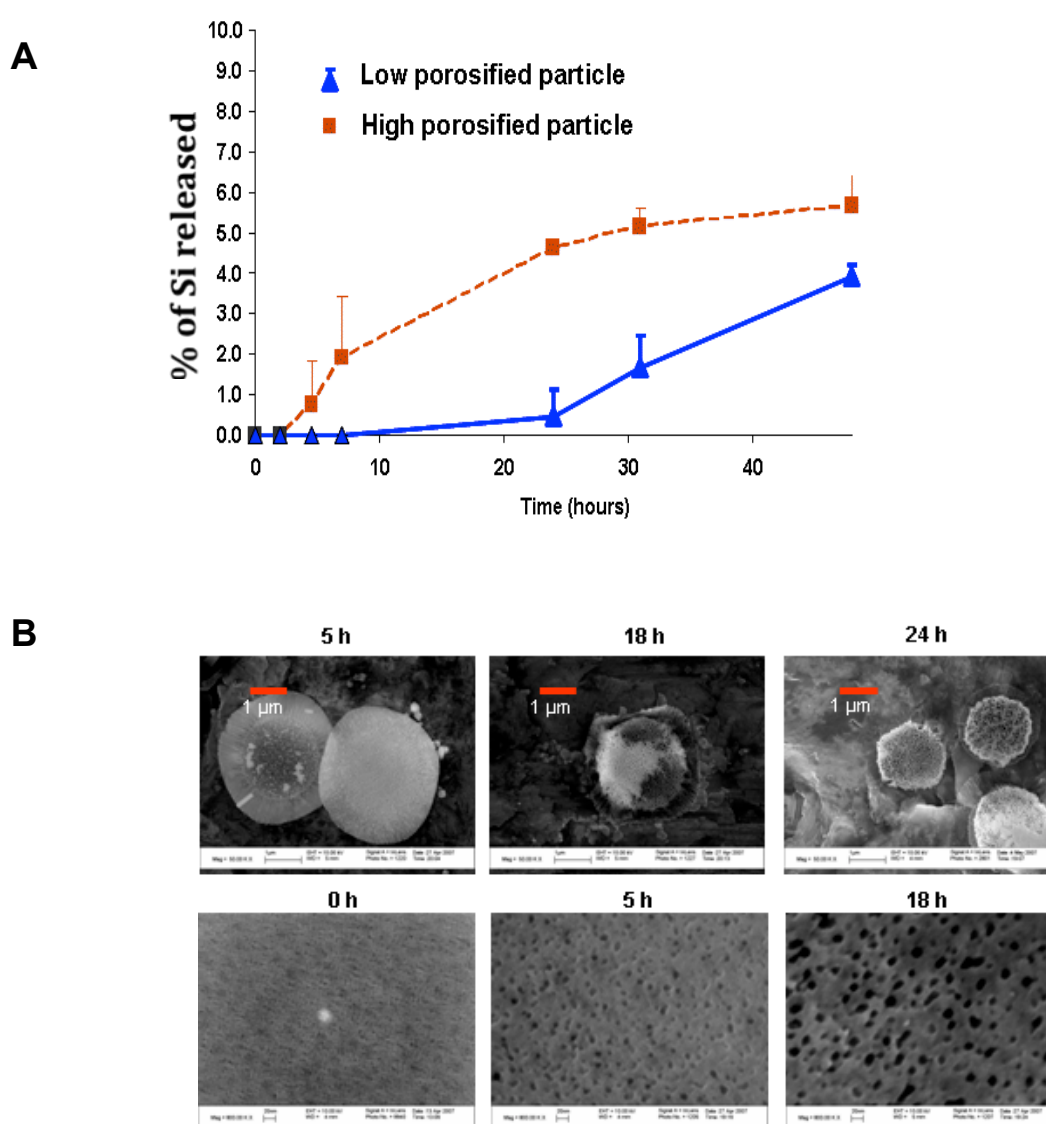


1.2.3.3 Biodegradation of MSVs

Silicon is an attractive material in drug delivery because silicon degrades into harmless silicic acid, which is abundant in nature. The degradation kinetics of MSV is influenced by the porosity of the silicon particles. MSVs of different porosities ranging between 15-70 % undergo degradation at different rates. Based on silicon analysis, MSVs with 60% porosity degraded completely within 30 hours, whereas MSVs with 20% porosity retained their overall structure over 40 hours (Fig. x). Therefore, low porosified particles can serve as an ideal delivery carrier for sustained release applications. SEM images showed that 60% porosified MSVs degraded over time and the outer ring structure was first lost and then the overall MSV size became smaller. Similarly, the pore size of MSVs increased over time, suggesting that enlargement of pore size due to degradation is one of mechanism by which a payload can be released from the porous structure (Fig. 8).

Figure 8. Degradation kinetics of MSVs. (A) Comparison of degradation kinetics of MSVs of different porosities as analyzed by Inductively Coupled Plasma-Atomic Emission Spectroscopy. **(B)** SEM images of MSVs incubated in saline solution (pH-7.2) at 37 °C for different time points.

Reproduced with permission from J Biomed Mater Res A, Godin, B. et. al. 2010, (44), copyright John Wiley and Sons 2010.



1.2.3.4 Biocompatibility of MSV

Porous silicon is an attractive material (45, 46), which has been investigated for possible applications in drug delivery by loading of nanoscale payloads such as protein (47), enzymes (48), drugs (46, 49), and nanocarriers (50). Unlike bulk silicon, porous silicon is highly biodegradable under physiological conditions. The ability of the porous silicon nanostructures to degrade into relatively harmless silicic acid byproducts presents fewer challenges for long-term applications. Similar to other porous silicon particles, MSVs are fully biodegradable under physiological conditions, with biologically benign degradation products (44). In addition, biocompatibility studies of MSVs have provided evidence that the intravenous administration of MSVs as a drug carrier is totally safe (51).

1.3. Adhesion molecules

Cellular adhesion molecules are expressed on the cell surface and helps in cell-cell interaction and adhesion. Some of the most common adhesion molecules include selectins (E-, P-, L- selectins), vascular cell adhesion molecule 1 (VCAM-1), intracellular adhesion molecule 1 (ICAM-1), and integrins ($\alpha\text{v}\beta 5$, $\alpha\text{v}\beta 3$). Selectins were originally named due to their selective expression and the presence of a lectin domain in the molecule. All selectin proteins consist of a lectin domain at the amino-terminus, followed by an EGF-like domain, variable number of consensus repeat (CR) domains, a transmembrane portion and ending with a short cytoplasmic tail (52). There is high homology (65%) between the primary sequences of different selectins throughout the lectin and EGF-like domains but the CR domains are less conserved. Their site of expression best classifies the selectins: for example activated endothelium (E-selectin), lymphocytes (L-selectin) and platelets (P-selectin).

1.3.1 E-selectin (CD62E, ELAM-1)

E-selectin is a member of the selectin family and is specifically synthesized by endothelial cells. In the very first experiments in 1985, treatment of endothelial cells with cytokines as well as bacterial endotoxins resulted in a dramatic increase in adhesion of isolated blood neutrophils and E-selectin was identified as a participant in this process. E-selectin expression is minimal on normal endothelial cells but the expression is induced in activated endothelial cells in response to cytokines such as tumor necrosis factor α (TNF- α), and interleukin (IL)-1 β . E-selectin gene contains binding sites for transcription factors

such as NF- κ B and AP-1. And in the presence of cytokines, E-selectin protein expression is rapidly induced, which peaks at 4 hours followed by a decline within 24 hours of stimulation. This decline in expression is due to the slow internalization and lysosomal degradation of the protein (53).

1.3.1.1 E-selectin – Expression and function

The major function of E-selectin is the recruitment of leukocytes to the site of inflammation. Leukocytes expressing a sialylated carbohydrate ligand (sLe^x, sLe^a) for E-selectin, bind to the inflamed endothelium via E-selectin, and roll along the endothelial surface to subsequently transmigration to the tissue (Fig. 9). Some studies have suggested that E-selectin can also participate in the adhesion of T-lymphocytes and monocytes to activated endothelial cells (54, 55). Abundant infiltration of leukocytes and immune cells to a tissue leads to pathological inflammatory conditions such as diabetes, atherosclerosis, rheumatoid arthritis and cancer. In case of cancer, infiltrated leukocytes secrete cytokines and stimulate the activation of fibroblasts, resulting in a local invasion through degradation of extracellular matrix (56). E-selectin antagonist (Cimetidine), a suppressor of E-selectin expression, has shown improved therapeutic outcome in colorectal cancer patients with metastasis from cancer cells that are sLe^x positive (57). In addition to E-selectin-mediated inflammation, a flurry of recent evidence has suggested the involvement of E-selectin in attachment and transmigration of cancer cells through the endothelium (58-60). Disseminated cancer cells express E-selectin ligands on the surface and exploit the E-selectin dependent recruitment mechanism to extravasate to distant site, a process termed as *vasculogenic mimicry* (61). The interaction of metastatic

cancer cells to endothelial cells *via* E-selectin has been shown to induce a bi-directional signaling that results in the activation of the ERK-Src pathway in the cancer cells and increased endothelial permeability, facilitating the transendothelial migration of cancer cells (62).

Studies have shown that E-selectin is constitutively expressed on postcapillary venules in the bone marrow endothelial cells (63) and mediates tethering and rolling interactions through E-selectin ligands on hematopoietic progenitor cells for their entry into bone marrow (64, 65) (Fig. 10A). This fact was further corroborated by a study that showed that stem cells not expressing E-selectin ligands such as mesenchymal stem cells homed to the bone marrow by engineering of their CD44 surface molecules into an E-selectin ligand (66). Furthermore, using *in vivo* imaging it was recently demonstrated that E-selectin expression in the bone marrow is discrete and discontinuous in specialized microdomains that co-localizes with homing sites of leukemic cells (67) (Fig. 10B). E-selectin also plays a role in homing of leukemic stem cells to bone marrow by binding carbohydrate ligands on their surface (68).

Figure 9. Function of E-selectin in recruitment of circulating cells. Presence of cytokines secreted from the inflammatory tissue leads to overexpression of E-selectin on the endothelial cells. Circulating cells including leukocytes and cancer cells express E-selectin ligands (sLe^x, sLe^a), which aid in the E-selectin mediated rolling followed by tight adhesion with other adhesion molecules such as ICAM. This subsequently leads to arrest and transmigration of these cells into the tissue.

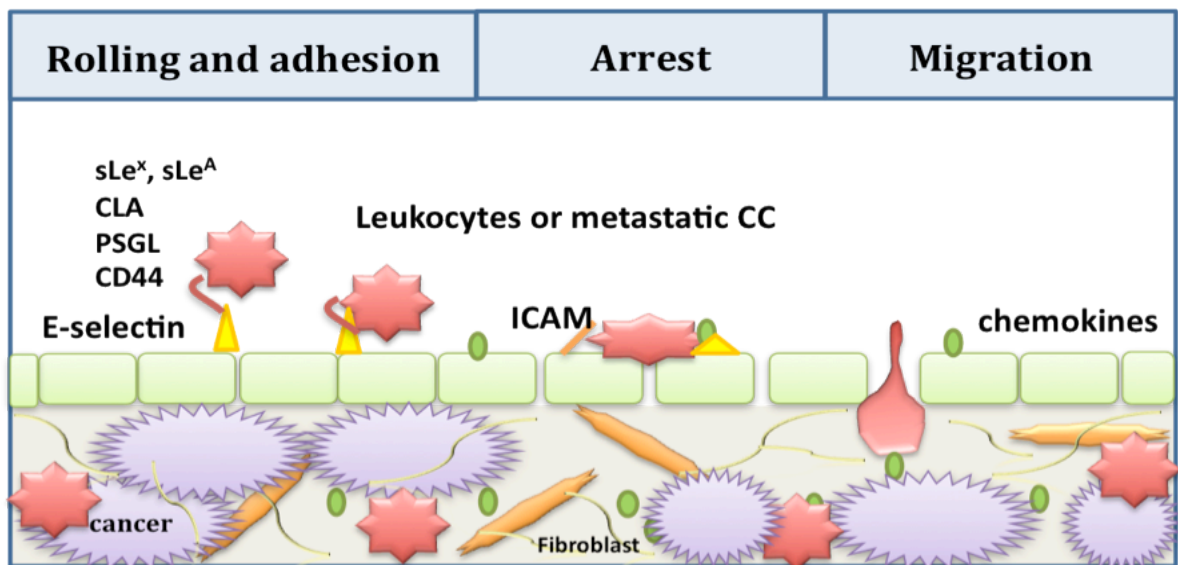


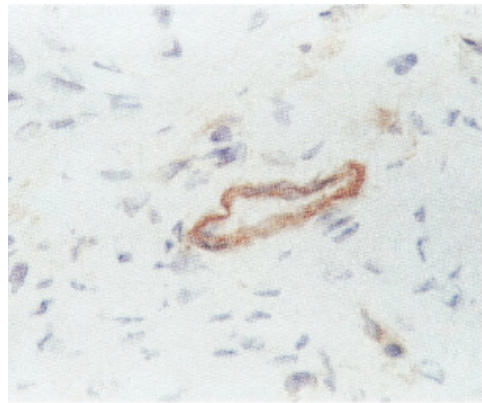
Figure 10. E-selectin expression on bone marrow endothelium. (A)

Constitutive expression of E-selectin on the bone marrow endothelium. (B) *In vivo* confocal imaging shows that E-selectin expression co-localized with homing of leukemic cells in bone marrow. Green - E-selectin, Red – Nalm-6 cells derived from Acute Lymphoblastic Leukemia. Scale bar, 100 μ m.

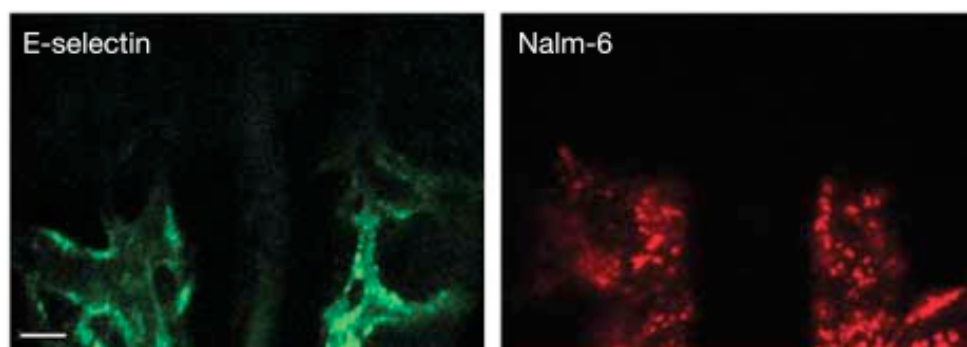
Reproduced with permission from Nature, Sipkins D.A et. al. 2005 (67).

Copyright Nature Publishing Group 2005.

A



B



1.3.1.1 E-selectin ligands for targeting

The two key characteristics of E-selectin expression namely the unique temporal and spatial expression profile and tissue specificity have prompted substantial interest in the potential therapeutic exploitation of this protein. In an attempt to develop tools for targeting E-selectin, numerous efforts have been made to develop a high affinity ligand including, a monoclonal antibody (69), peptide (70), and carbohydrate ligand (71). These ligands have shown binding to the inflamed vasculature in both experimental animal models and clinical trials (72). Some of these ligands have been conjugated to different types of nanoparticles including iron oxide nanoparticles, liposomes, and micelles for improved targeting performance to the inflamed vasculature of different disease models including inflammatory conditions and cancer (73-75). However the use of these ligands for active targeting remains a challenge due to various reasons, such as low affinity and specificity, lack of serum stability, immunogenicity, and high cost (70, 71). Therefore, E-selectin ligands that can overcome these limitations for clinical applications for targeted delivery are highly desirable.

1.3.2 Thioated Aptamer ligands

Aptamers are structurally distinct RNA and DNA oligonucleotides that can mimic protein-binding molecules based on their unique tertiary structures. Aptamers against a target molecule are identified through a selection-based process known as systematic evolution of ligands by exponential enrichment (SELEX) first described by Gold and colleagues in 1990 (76). This process comprises of first a synthesis of a combinatorial nucleic acid library (DNA or

RNA), which is incubated with the desired target molecule under suitable binding conditions. The bound aptamers are partitioned and enriched through PCR amplification for another round of selection. Repeated iterative cycles (normally around 10 cycles) lead to a high affinity aptamer molecule against the target molecule of interest. Based on these characteristics such as high affinity, easy and cost effective synthesis, long shelf-life, and minimal immunogenicity, have made aptamers attractive alternatives to small molecule drugs and antibodies for diagnostic and therapeutic applications (77).

Macugen (Pegaptanib) a RNA-based molecule was the first aptamer approved by FDA to treat age-related macular degeneration (78). However, medical applications of unmodified aptamers are limited to transient treatment (79) or local administration (80), due to lack of *in vivo* stability against nucleases (81, 82). Therefore, for improvement of serum stability of aptamers various chemical modifications incorporated into the sugars or internucleotide phosphodiester linkages have been successfully achieved (83-85). For example, AS1411 a modified aptamer that binds nucleolin has shown increased *in vivo* stability due to the formation of dimers and a quartet structure (86). Phase II clinical trials of AS1411 for the treatment of renal cell carcinoma are currently underway. Similarly, aptamer conjugated nanoparticles have been successfully used for a targeted delivery of chemotherapeutic drugs both *in vitro* (87) and *in vivo* (88).

One of the modifications leading to nuclease-stabilized aptamers is the sulfur substitution of phosphate oxygen on the DNA backbone, which results in thioated aptamers or thioaptamers with higher affinity to target protein (89). This increased affinity can be attributed to sulfur being a softer anion resulting in

decreased interactions with solvated cations (90). Thio-substitution of the nucleotide backbone has also shown to improve the stability of the aptamer with no increase in toxicity (91). Thio-substitution can lead to monothioate or dithioate aptamers (Fig. 11). Recent advances in combinatorial chemistry have enabled the construction and screening of large random thioaptamer libraries for affinity to proteins or other targets such as NF-IL6, HIV RT, Venezuelan Equine Encephalitis nucleocapsid, TGF- β HepC IRES nucleic acid, NF- κ B and CD44 (92-94). Based on these properties thioaptamers are attractive ligands for in vivo targeting. The presence of positively charged amino acids on the E-selectin protein (Fig. 12) presents an opportunity to screen thioaptamer ligands against E-selectin, which would be very advantageous for targeting E-selectin in vivo.

Figure 11. Structure of thioaptamers. The phosphate backbone substitution of one of two non-bridging oxygens result in either the monothioate or dithioate aptamers respectively.

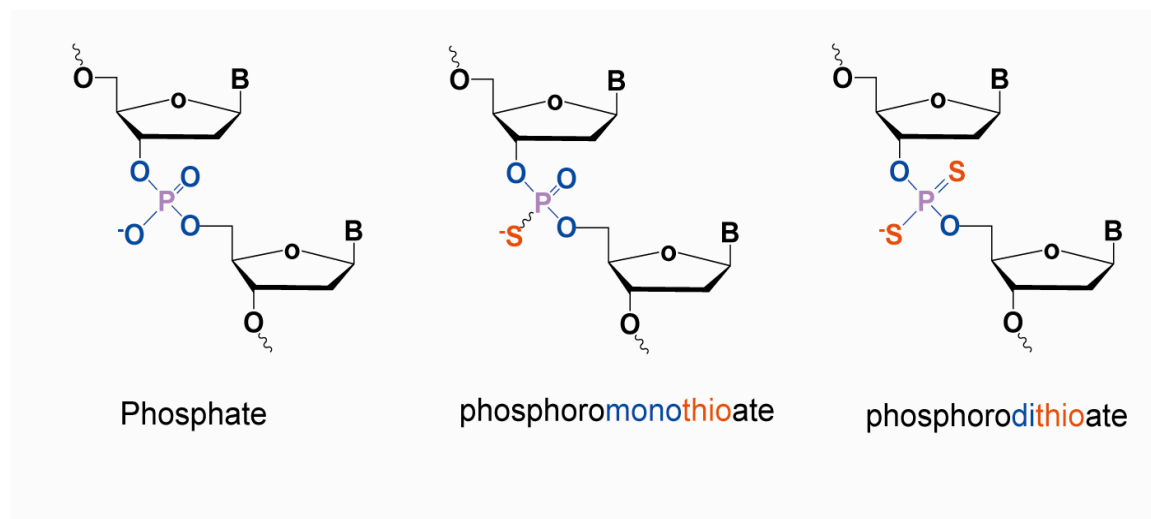
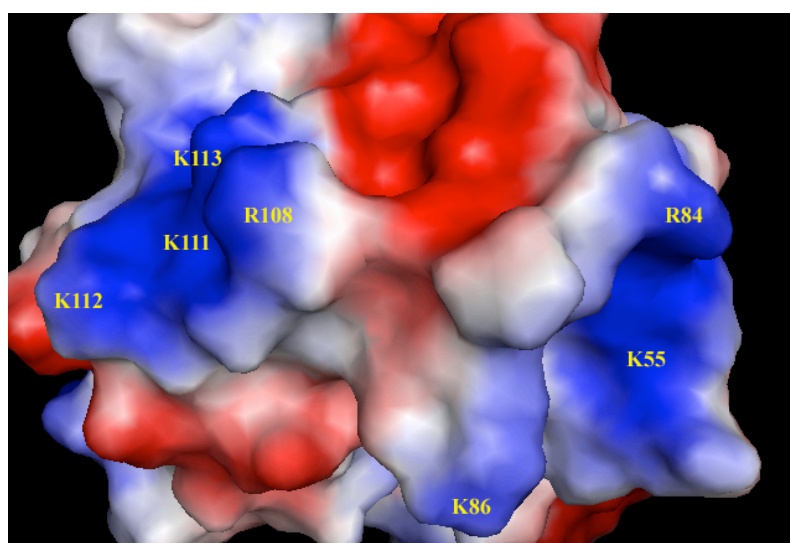


Figure 12. Electrostatic surface of E-selectin protein. Blue area represents positively charged amino acids consisting of hydrophilic-charged amino acids. R-arginine; K-lysine; E-glutamate; D-aspartate; H-histidine.



1.4 Objectives and Hypothesis

Bone marrow is a target organ site involved in multiple diseases including myeloproliferative disorders and malignancies such as myeloma and metastases from primary sites such as breast and prostate. Most of these diseases are associated with poor quality of life and the treatment options are limited, and therefore, there is a critical need to develop effective therapeutic strategies that allows for selective delivery of therapeutic payload to the sites of bone marrow involvement. E-selectin is constitutively overexpressed on the bone marrow vasculature, but almost absent in normal vessels, and therefore, E-selectin targeted drug delivery presents an ideal strategy for the delivery of therapeutic nanoparticles to the bone marrow. Nanotechnology-based drug delivery systems provide the opportunity to deliver drugs to the target tissue while decreasing exposure to normal tissues.

The objective of this study was to develop a drug delivery carrier employing nanotechnology specifically targeted to the bone marrow for the delivery of therapeutic and imaging agents. **We hypothesize that a multistage approach based on first stage biodegradable silicon porous particles conjugated with a high affinity E-selectin thioaptamer ligand will target preferentially to the bone marrow.**

To achieve the aforementioned goals, the following three **Specific Aims** are proposed.

Specific Aim 1: Characterization of the porous silicon multi-stage vector.

The multistage vector (MSV) was characterized in terms of size, surface charge and biocompatibility. The biodistribution and in vivo degradation of the MSV was analyzed. And lastly, sustained gene silencing in tumors by siRNA delivery through MSV was demonstrated.

Specific Aim 2: Identification of high affinity E-selectin thioaptamer ligand.

A high affinity thioaptamer ligand against E-selectin was identified using a two-step screening strategy. ESTA-1 was characterized in terms of E-selectin binding *in vitro* and *in vivo*.

Specific Aim 3: Development of bone marrow targeted multistage vector.

ESTA-1 conjugated MSVs were developed and characterized. ESTA-MSVs showed binding to E-selectin on cells as well as homing to the bone marrow and subsequent delivery of therapeutic nanoparticle payload to the bone marrow tissue.

Chapter 2. Materials and Methods

2.1 Cell culture

The human microvascular endothelial cells (HMVECs) were a kind gift from Dr. Rong Shao (Biomedical Research Institute, Baystate Medical Center/University of Massachusetts at Amherst, Springfield, MA). HMVEC were grown in endothelial basal medium-2 (Lonza, supplemented with 10% (v/v) Tet-approved fetal bovine serum, 100 U/ml penicillin and 10 mg/ml streptomycin, 1 mg/ml epidermal growth factor and 50 mg/ml hydrocortisone. Hybridoma cells were purchased from American Type Culture Collection (Manassas, VA, cat # HB-11684) and grown in complete growth media comprising of RPMI 1640 medium (HyClone, Waltham, MA), 90% and horse serum, 10%. Breast cancer 4T1 cells were purchased from ATCC (cat # CRL-2539) and grown in RPMI-1640; (HyClone, Waltham, MA) supplemented with 10% FBS, penicillin–streptomycin and L- glutamine. HL-60 was purchased from ATCC and grown in Iscove's Modified Dulbecco's Medium supplemented with 20% FBS.

2.2 Development of ES-Endo cells

E-selectin cDNA was obtained (Origene, Rockville, MD) and the ORF was amplified by PCR using the primers listed in Table 1 and ligated into TOPO Blunt (Invitrogen, Carlsbad, CA). E-sel TOPO pBlunt was digested with Mlu I and Sal I to E-selectin gene was inserted into pTRE-Dsred expression vector (Invitrogen, Carlsbad, CA). A clone containing E-selectin-dsred was selected and verified to contain the construct by double digestion with above enzymes. HMVEC were

stably transfected with rtTA plasmid (Clontech, Mountain View, CA) and the clones were screened with 0.5 mg of G418 for two weeks. A positive clone was selected. The selected clone was co-transfected with 15 µg of pTRE-Tight-BI-human E-selectin-RFP and puromycin resistant plasmid using Lipofectamine 2000 (Invitrogen, Carlsbad, CA). The cells were further incubated in the presence of puromycin (300 ng) and the positive clone was selected by single colony isolation and analyzed for E-selectin inducible expression.

Table 1. List of primers used for PCR and sequencing reactions.

PCR Primers	
Sense primer	GGTACCACGCGTACAATGATTGCTTCACAGTTTCTC
Antisense primer	GTCGACATCGATGGCTTAAAGGATGTAAGAAGGCTT
Sequencing primers	
Position 450	CACGGTGAATGTGTAGAG
Position 901	AAAGCTGTGACATGCAGG
Position 1353	ACCTACAAGTCCTCTTGTGCC

2.3 Screening of E-selectin thioaptamer (ESTA-1)

2.3.1 Synthesis of thioaptamer library

ESTA was chemically synthesized as described previously (37, 95). Briefly, phosphoramidite chemistry in 1 μ mol scale was used on a DNA synthesizer (Experdite 8909, Applied Biosystems). The sequence of ESTA was programmed on the synthesizer with a 3' thioate linkage at every adenine residue. At the end of the synthesis, 5' end of the oligo was coupled with Cy3 phosphoramidite (Glen Research, VA) with the MMT protective group remaining. Then the 5'-carboxy modifier-C10 (Glen Research, VA) was coupled to the 5' end of the oligo. The oligo was cleaved from the beads and the protecting groups were removed with 0.4M methanolic NaOH at room temperature for 24-36 hr. The deprotected oligo was diluted with water and desalted in a 10,000 MWCO spin column (Amicon) at 4000 x g and dried on the lyophilizer. The oligo was then purified on FPLC with a monoQ ion exchange column. Biotinylated double stranded PCR products were mixed with Streptavidin coated magnetic particles in binding buffer A (10 mM Tris-HCl, 2 M NaCl, 1 mM EDTA, at pH 7.5) and incubated at room temperature with gentle rotation for 30 minutes according to the manufactures instructions. The beads were washed with the binding buffer A and followed by alkaline melting (0.1M NaOH) to separate the unbiotinylated single stranded DNA (ssDNA) from the bead-bound double stranded DNA (dsDNA). After purifying using spin columns the single stranded TA library was taken in buffer B (Phosphate buffer Saline supplemented with Ca^{2+} and Mg^{2+} , and 5 mM MgCl_2), denatured at 95°C and cooled on ice prior to use to favor the formation of hairpin loop structures.

2.3.2 Combinatorial selection of thioaptamers

The selection of TA against E-selectin was carried out by the solution based nitrocellulose filter method as described previously (ref). Briefly, the recombinant human E-selectin protein (240 pmoles in PBS, was mixed with a previously nitrocellulose filtered (to exclude the sequences that bind to the nitrocellulose) ssDNA TA library (200 pmoles) in binding buffer A and incubated at room temperature for 2 hours. The reaction mixture was filtered through the nitrocellulose filter and washed 3 times with the binding buffer to remove any unbound and weakly bound TAs. The TA-E-selectin complex retained on the filter was eluted with 8 M urea solution. The eluent was PCR amplified by the above-described method and analyzed by nondenaturing 15% polyacrylamide gel electrophoresis (integrity). Stringency of the selection was increased at each iterative cycle by decreasing the amount of E-selectin, gradually lowering the incubation time (120 minutes at cycle 1 and gradually reduced to 40 minutes at cycle 10) and increasing the number washes. The TA libraries obtained from rounds 5 and 10 were PCR amplified and cloned into *E.coli*. Plasmids were purified and DNA sequences were isolated and a subset of sequences was determined. The individual TA sequences were synthesized with cyanine-3 label at the 5' end, from the plasmids, with 5'-biotinylated forward primer and 5'-cyanine-3 labeled reverse primer by PCR amplification and used in the binding experiments.

2.3.3 TA binding to Endothelial cells

All binding experiments with TA were done with ES-Endo cells plated onto plastic plate and cultured overnight to allow them to attach. After E-selectin induction, cells were incubated with thioaptamer at indicated concentrations (10-100 nM) for 15 minutes at 37 °C. The cells were washed with ice cold PBS to remove unbound TA and fixed with 4 % paraformaldehyde for 10 minutes. The cells were stained with 1.0 µg/mL Hoechst for 10 minutes to counterstain the nuclei. TA binding to the cells was assessed by fluorescence microscopic analysis (TE2000-E, Nikon, final magnification 60x). All images were acquired under the same exposure conditions for the comparison of binding.

2.4 Purification of E-selectin antibody

Hybridoma cells were grown in complete growth media containing 10 % FBS. Supernatant (100 ml) was collected after spinning down cells at 1200 rpm and filtered through 0.2 µm filter followed by a centrifugation through a centricon filter (MWCO = 30K) at 4500 rpm for 30 minutes. The fraction in the filter was collected and pooled together. 10X PBS (1/10th volume of the collected solution) was added to have PBS like condition for binding. 80 µl of goat anti-mouse IgG magnetic beads (New England BioLabs, Ipswich, MA) were pre-washed with cold PBS twice using a magnet. The supernatant from the cells was incubated into 4 tubes containing (1/4 beads each) for overnight at 4 °C on a rotating block. Using the magnet excess solution was removed and the beads were washed 4 times with cold PBS (100 µl each). To remove IgG bound to the beads 100 µl of elution buffer was used and immediately after 100 µl per ml of 1M Tris (pH 7.4)

was added to readjust pH. The solution was dialyzed with PBS for 4 hours and collected. Finally, the solution was mixed with 15 % glycerol and aliquoted to be stored at -20 °C.

2.5 Cell viability studies

ES-Endo cells were seeded at 10,000 per well in 96-well tissue culture plate and with TA at indicated concentrations for 48 hours, with pre-induction with doxycycline (1000 µg/ml) for 5 hours. For the measurement of cell viability, 10 µl MTT (5 mg/ml) was added to each well and incubated for 4 hours. The formazan was dissolved in 150 µl of DMSO and measured by absorbance of each well using plate reader at 490 nm.

2.6 Development of Multistage vectors (MSVs)

2.6.1 Fabrication of MSVs

MSV were fabricated by electrochemical etching of silicon wafers in the Microelectronics Research Center at The University of Texas at Austin as previously described (37). The physical dimensions of MSV were verified by high-resolution scanning electron microscope.

2.6.2 Surface modification and characterization of MSVs

The modification of MSV was a three-step reaction as described previously (96). The suspension containing MSVs was transferred to a glass beaker and the isopropanol (IPA) was evaporated overnight using a hotplate set at 110 °C. The dried MSVs were then treated with piranha solution (1 volume

H₂O₂ and 2 volumes H₂SO₄) with heating to 110–120 °C for 2 h with intermittent sonication to disperse the MSVs. Oxidized MSVs were washed in IPA, and then suspended in IPA containing 9 % (v/v) 3'-aminopropyltriethoxysilane (APTES) (Sigma–Aldrich, St. Louis, MO) for 16 h at 35 °C and 1300 rpm. The APTES-modified MSVs were washed in IPA and the surface charge was measured by Zeta Pals (Brookhaven Instruments, Holtsville, NY) as described previously in (96). The size, zeta potential and the number of MSVs was measured using a Multisizer (Beckman) and ZetaPals instrument (Brookhaven Instruments). 2 µl of MSVs were added to 1.4 mL of 10mM phosphate buffer (pH 7.3) and the analysis was conducted at room temperature (23 °C) in triplicates.

2.7 Conjugation of ESTA to MSV

Conjugation of ESTA to MSV was carried out using a PolyLink Protein Coupling Kit as per manufacturers protocol (Bangs Laboratories, Inc., Fishers, IN). Briefly, 0.5 ml of 50 µM Cy3 labeled ESTA was incubated in 150 µL of PolyLink Coupling Buffer. 20 µL of EDAC (200 mg/mL) and 20 µL of sulfo-NHS (200mg/mL Pierce biotechnology) solution were added to the ESTA solution and mixed end-over-end for 30 minutes at room temperature. 4×10^8 NH₂ modified MSV were resuspended in 0.17 mL PolyLink Coupling Buffer and added to the ESTA solution and incubated for 4 hours at room temperature with gentle mixing. The mixture was then centrifuged for 10 minutes at approximately 4000 x G and the pellet was resuspended and stored at 4°C in PolyLink Wash/Storage Buffer.

2.8 Infrared Spectroscopy

Fourier transform infrared spectroscopy (FTIR) was performed on a Nicolet 6700 (Thermo Scientific, Waltham, MA) with a smart diamond crystal attenuated total reflection (ATR) accessory. To confirm the ESTA-1 conjugation to the MSV, the IR spectrum of ESTA-MSV was compared with ESTA and MSV alone. Samples ($10^5/\mu\text{l}$) were diluted in deionized water and a 2 μL drop from each sample was placed on the diamond crystal and subjected to vacuum. Each sample was run for 150 scans at a resolution of 4 wavenumbers.

2.9 Flow cytometry

For analysis of E-selectin expression a 10 cm Petridish space was used for cell culture to yield about 1 million cells. The medium was removed and cells were washed with PBS. 5mM EDTA was added to the cells and incubated in 37 °C for 10 minutes until the cells became rounded. The cells were then scraped using a cell lifter and collected in FACS tube. Cells were then spun down at 1500 rpm for 5 minutes to remove EDTA and re-suspended and washed twice in PBS containing 2 % FBS. 5 μl of PE labeled anti-E-selectin monoclonal antibody (BD # 551145) per 1 million cells was added and incubated on ice in dark for 45 minutes. Cells were then washed with PBS buffer containing FBS twice and analyzed using the PE filter on a flow cytometer (Becton Dickinson, FACScalibur). For fluorescent analysis of particles, 10^5 MSVs were incubated in PBS and washed for two times. The fluorescence was measured on the flow cytometer (BD Biosciences).

2.10 Endothelial cell adhesion studies

E-selectin inducible endothelial cells (ES-Endo) were cultured as described previously (95). For MSV adhesion studies, ES-Endo were plated on 16-well chamber slides and induced with doxycycline (2000 ng/ml) for 5 hours. 10^5 MSV were added to each well in the presence of complete growth media and incubated with cells for 1 hour at 4°C. The media was removed and the cells were washed twice to remove unbound particles by mild shaking. The cells were then fixed with 4 % paraformaldehyde and stained with FITC-phalloidin and DAPI. The slide was mounted and analyzed by microscope. The number of MSV bound per cell was counted at five different fields of view.

2.11 Loading of nanoparticles into ESTA-MSV

Quantum dots (QD 655) were purchased from Invitrogen (Cat #Q21521MP, Carlsbad, CA) and iron oxide nanoparticles (IONs) were purchased from Ocean Nanotech (Cat #SHA-15-05, Springdale, AR). DOPC liposomes were developed and loaded as described previously in (96). ESTA-MSVs ($3\text{--}5 \times 10^6$) were loaded with IONs (25 µg; aminoPEG modified) in borate buffer (25 µL), then centrifuged and washed twice in fresh borate buffer or Millipore water. Iron oxide loading was quantified using a Prussian blue assay. An aliquot from each sample (5 µL) was heated at 50 °C in 6N HCl (120 µL) for 2 hours with agitation to convert IONs into free iron. Iron was oxidized using ammonium persulfate (0.1 mg/mL; BioRad, Richmond, CA) and a color reaction was initiated by adding 5% potassium hexacyanoferrate ($\text{K}_4[\text{Fe}(\text{CN})_6] \cdot 3\text{H}_2\text{O}$) (125 µL; Sigma–Aldrich) and incubating for 10 minutes. A standard curve was

generated using iron (III) hexahydrate (Sigma–Aldrich, St. Louis, MO), and the absorbance was read at 690 nm using a plate reader spectrophotometer.

2.12 Immunofluorescence

Cells were grown in chamber slides and the media was removed. The chamber slide was disassembled and the cells were washed with PBS for 5 minutes twice at room temperature (RT). The cells were fixed with 4 % paraformaldehyde in PBS for 15 minutes at RT. Paraformaldehyde was removed and cells were washed with PBS for 5 minutes each for three times at RT. If required cells were permeabilized with 0.1 % Triton-X 100 in PBS for 10 minutes and washed with PBS for 5 minutes each for three times at RT. For blocking cells were incubated with 10 % goat serum in PBS for 1 hour at RT. Blocking solution was removed and the cells were incubated with primary antibody (anti E-selectin) at dilution 1:100 in 5 % goat serum in PBS for overnight at 4 °C. Cells were washed with PBS for 5 minutes each for three times at RT and incubated with secondary antibody (Anti-mouse 488) at dilution 1:400 in 5 % goat serum in PBS for 30 minutes at RT. Cells were covered with aluminum foil during incubation for all further steps. The cells were washed with PBS for 5 minutes each for three times at RT and the nucleus was stained using Hoechst Stain (1:2000 dilution) (Invitrogen, Carlsbad, CA) in PBS for 10 minutes RT. Cells were washed with PBS for 5 minutes once and rinsed with water and the slide was air dried under the foil. The slide was mounted using mounting media and examined under the fluorescent microscope and stored in the dark at 4 °C.

2.13 Animal studies

All animals were handled in strict accordance with good animal practice as defined by University of Texas Health Science Center Institutional Animal Care and Use Committee (IACUC), and all animal work was approved by the committee.

2.13.1 Animal tumor models

Orthotopic mouse models of ovarian carcinoma were developed by intraperitoneal injection of 10^6 SKOV-3ip into nu/nu animals as previously described (97). Breast tumors were inoculated by injecting 10^5 4T1 cells into the mammary fat pad of nu/nu mice.

2.13.2 Targeting studies

For *in vivo* targeting experiments a total of 5×10^7 MSV were intravenously injected to mouse through the tail vein. Major organs including liver, kidney, spleen, lung, and heart and bone marrow were harvested after 5 hours and processed for silicon contents and histological analysis.

2.14 Silicon content analysis

All the major organs were collected and lysed using RIPA buffer containing DNase. Organs were homogenized using a homogenizer and spun down at 10,000 rpm for 20 minutes and washed the pellet once with water. 3 ml of TMAH (Tetramethyl ammonium hydroxide 25 % in water, Fischer Scientific)

was added and the samples were incubated at 50 °C for 16 hours to dissolve the silicon particles. 500 µl of sample was dissolved in 2.5 ml DI water to measure the silicon content using inductively coupled plasma atomic emission spectroscopy (ICP-AES). To measure amount of silicon in injections, 10 µl of injected particles were dissolved in 90 µl of TMAH at 50 °C for overnight and 100 µl from this solution was analyzed on the ICP. To analyze silicon in the bone marrow, the marrow from the tibia and the femur bone was collected using an insulin syringe with PBS. The marrow was spun down at 8000 rpm for 5 minutes to collect cells and particles. The pellet was dissolved in 100 µl RIPA and incubated at 55 °C for 24-36 hours in a shaker. The entire sample was analyzed on the ICP. Silicon was detected at four different wavelengths of 250.69, 251.43, 251.61, and 288.158 nm and Scandium (1 ppm) was used as an internal control for normalization. All results were expressed as percent of injected dose or percent Si per gram of tissue.

2.15 Statistical analysis

Numerical data were expressed as means \pm standard error. Statistical differences between the means for the different groups were evaluated with Microsoft Office Excel using either the Student's T-test or analysis of variance (ANOVA), with the level of significance at $p < 0.05$.

Chapter 3. Experimental Results

3.1. Properties of MSV

3.1.1 Physico-chemical properties of MSV

Our group has successfully fabricated porous silicon multistage particles (MSV) with different size and shapes using a combination of standard electrochemical etching and photolithographic techniques as summarized in the schematic (Fig. 13). Since the focus of this study is vasculature targeting of MSV, quasi-hemispherical shaped MSVs were fabricated based on the rational design to enhance interaction with the vasculature as described in detail in the introduction.

MSVs used in this study were first characterized by different techniques. Scanning electron micrograph (SEM) images showed that the average diameter of quasi-hemispherical MSV was $1.6 \pm 0.1 \mu\text{m}$ with pore size of 30 nm (Fig. 14A-D). Reproducibility of the geometry of MSV was verified by size distribution analysis using a multisizer (Fig. 15) and all the counting and sizing of MSVs for subsequent experiments was carried out using the multisizer.

Figure 13. Schematic outline of the fabrication protocol for MSV.

Combination of photolithography based microfabrication and electrochemical etching. **(A)** A silicon substrate masked with silicon nitride is patterned through photolithography; **(B)** pattern is transferred and trenches are formed in the silicon by reactive ion etch; **(C)** the electrochemical etching results in selective porosification, and **(D)** the particles are released from the substrate by sonication.

Reproduced by permission from Biochimica et biophysica acta, Serda, et al, 2010 (98). Copyright Elsevier 2010.

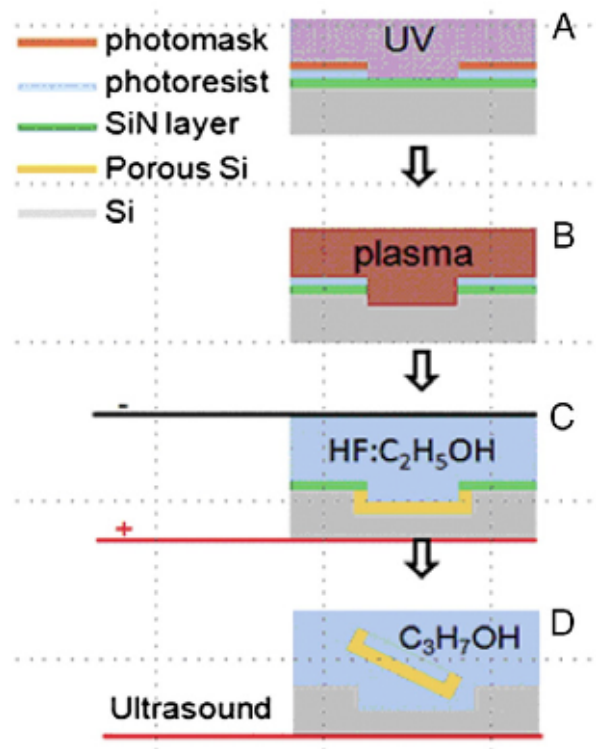


Figure 14. SEM images of porous MSVs with different magnifications. (A) Image of a collection of MSVs; **(B)** Single MSV; **(C)** Cross-section of a MSV; **(D)** Close-up view of the porous structure of a MSV.

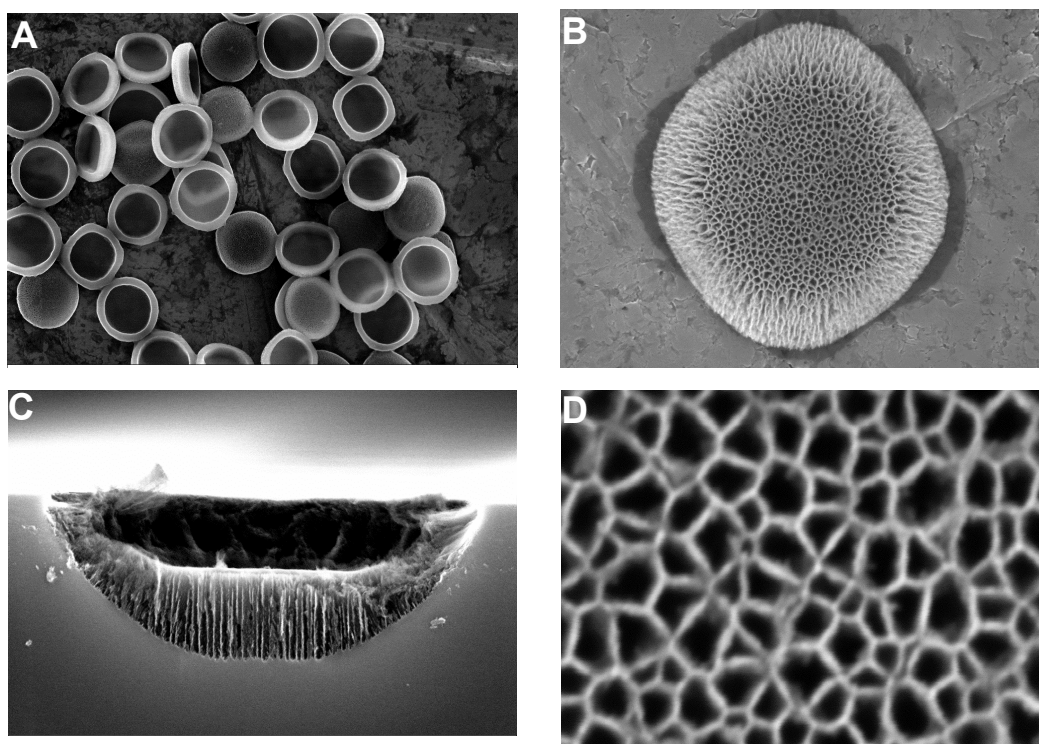
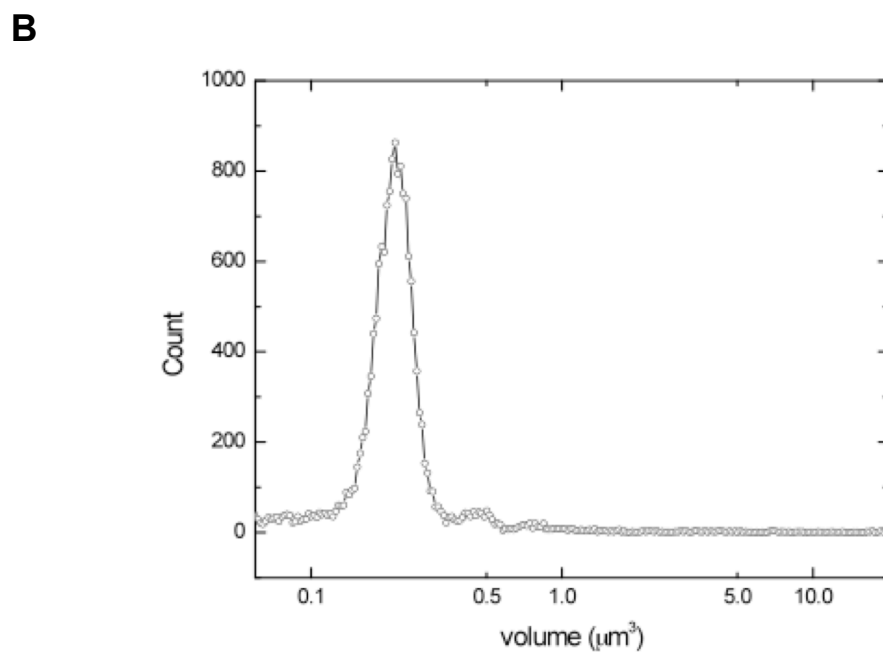
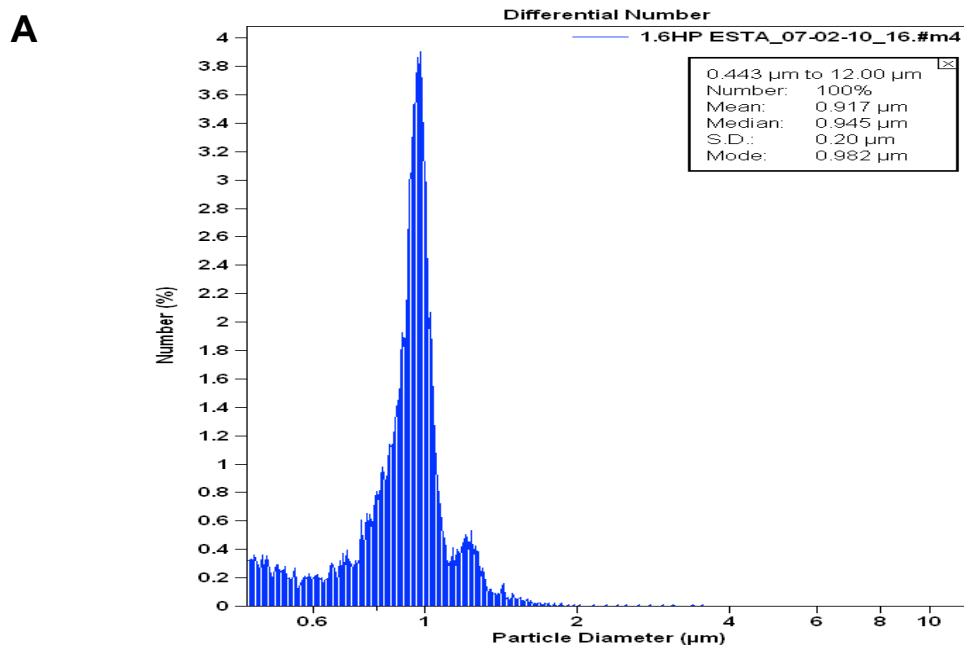


Figure 15. Size distribution of MSVs. MSVs were re-suspended in IPA and the size was measured on a multisizer with three repetitive runs to analyze **(A)** mean diameter; and **(B)** volume equivalent of a spherical particle.



3.1.2 Biodistribution and biodegradation of MSV

To examine the biodistribution of MSV, the mice were injected with MSV intravenously, and the major organs including liver, kidney, spleen, lung, and heart were harvested 5 hours after the injection. Silicon content analysis demonstrated that MSV primarily accumulated in the liver (48 %) and spleen (17 % of total injected dose), and there was minimal MSV accumulation in the kidney, lung, heart and the bone marrow (**Fig. 16**). However, based on our microscopic analysis, there was no evidence of embolization of MSV in the capillaries.

After analyzing the bio-distribution of intravenously injected MSVs, the next step was to examine *in vivo* biodegradation of MSVs in the liver and spleen. For this the silicon content in these organs was measured at different time points. Silicon content in the spleen reduced by 80 % in the first two weeks and cleared by the third week (**Fig. 17**). In contrast, only 55 % of MSV was cleared from the liver in the first two weeks, and approximately 25 % of the injected MSV remained in the liver 3 weeks after injection (**Fig. 18**), suggesting that MSV degradation kinetics are different in each organ. SEM images of the MSV showed enlargement of pore size at day 7 and reduction of overall size by day 14 (**Fig. 18**). Collectively, these data suggest that the MSV can serve as reservoir to protect its payload from degradation, and release them over time by a mechanism that combines degradation of the carrier material, and hindered diffusion through the nanoporous structure.

Figure 16. Biodistribution of MSV. Silicon content analysis of organs isolated from mice (n = 6) following i.v. injection of MSV. The major organs including heart, lung, liver, kidney, and spleen were harvested 4 h after the i.v. injection. Silicon amount was measured by inductively coupled plasma atomic emission spectroscopy and expressed as % of injected dose per organ (% ID). n.d., not detected.

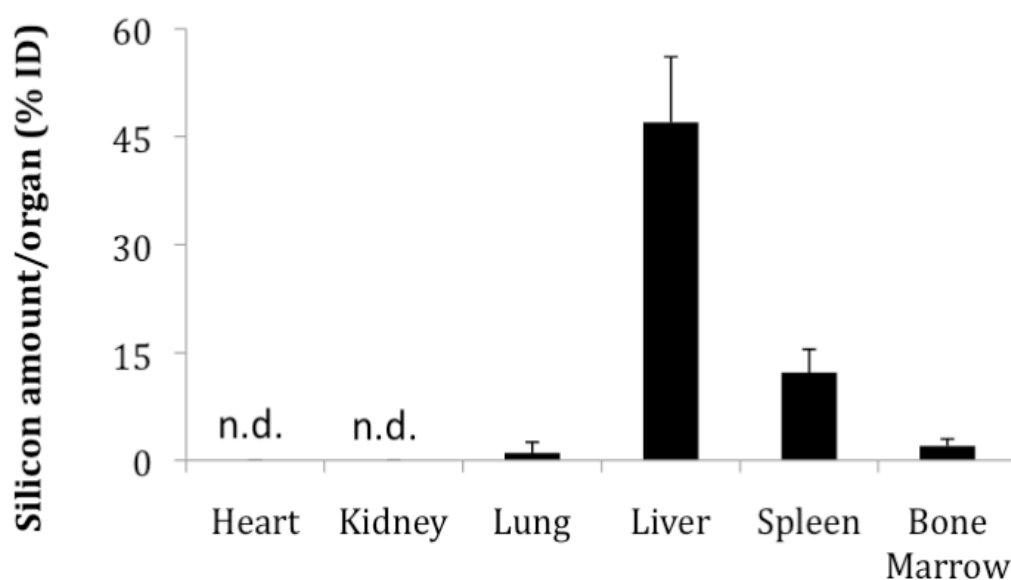
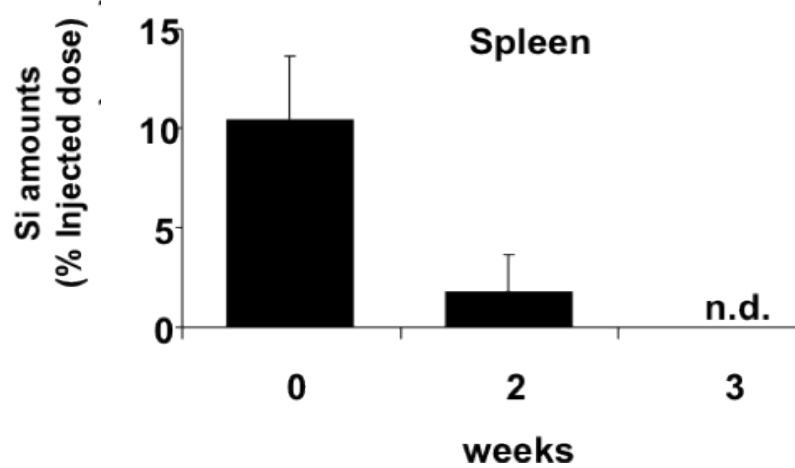


Figure 17. Biodegradation of MSV. (A) Silicon contents in the liver and **(B)** spleen after i.v. injection of MSV at different time points. Silicon amounts were expressed as % of injected dose per organs (% ID).

Reproduced with permission from Cancer Research, Tanaka et al, 2010, (96).

Copyright American Association of Cancer Research 2010.

A



B

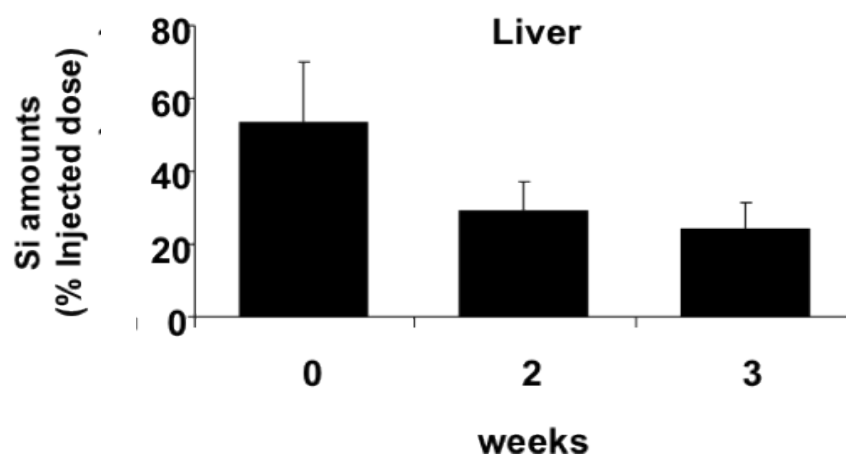
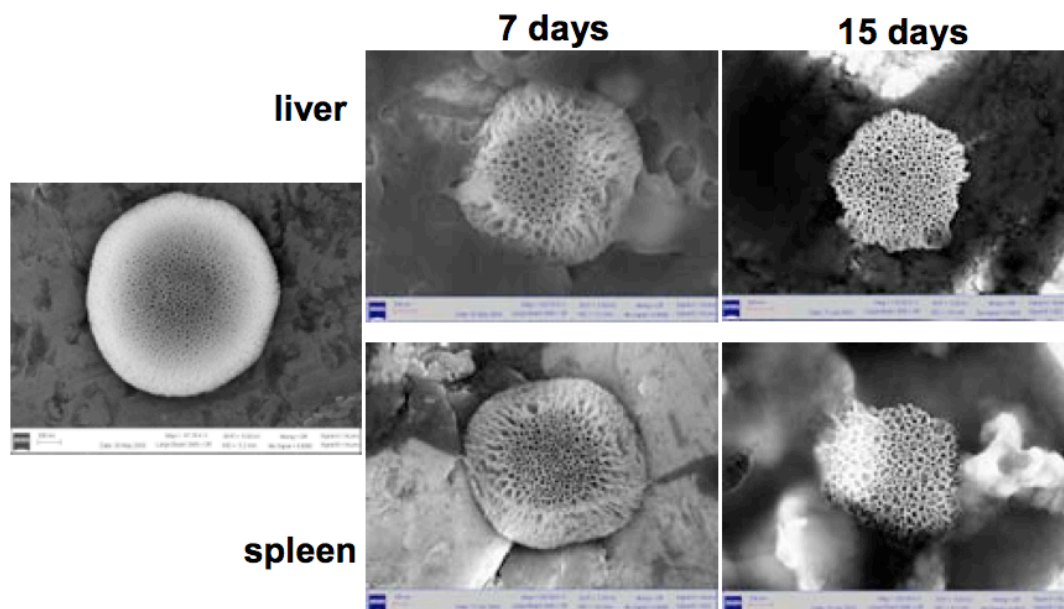


Figure 18. *In vivo* degradation of MSVs. SEM image of MSVs isolated from the liver and spleen after 7 and 15 days of injection. (Original magnification= x 50000).

Reproduced with permission from Cancer Research, Tanaka et al, 2010, (96).

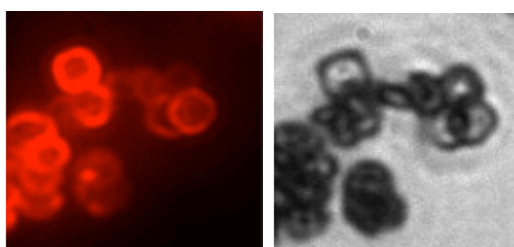
Copyright American Association of Cancer Research 2010.



3.1.3 Sustained delivery of siRNA contained in MSV

Based on the unique biodistribution and sustained biodegradation properties *in vivo*, we next tested if a payload incorporated into the MSV could be released for a sustained period of time. For a proof of principle we tested siRNA delivery to achieve sustained gene silencing. For this we first demonstrated siRNA encapsulated into nanoliposomes could be incorporated into the MSV. Fluorescently labeled siRNA with Alexa 555 were encapsulated into nanoliposomes and loaded into the silicon particles (Fig. 19). The image demonstrated that nanoliposomes containing fluorescently labeled siRNA were effectively incorporated into the porous particles and intensive fluorescence was observed in the majority of the particles as seen in Figure 19.

Figure 19. Liposome loading into MSVs. Fluorescent **(A)** and phase **(B)** view of siRNA encapsulating liposomes incorporated into MSVs



To highlight the feasibility of the multistage delivery system, nanoliposomes were effectively incorporated into the MSVs (with 1.6 μm diameter, 60 % porosity, and 40 nm pore size) and for proof of concept the delivery of a liposome encapsulating siRNA for the sustained silencing of the gene was tested. The gene selected for this study was EphA2 an oncogenic tyrosine kinase receptor overexpressed in ovarian cancer (97).

To test this delivery, mice bearing orthotopic tumors derived from SKOV-3 cells (15 days after intraperitoneal inoculation of tumor cells) were injected with 3×10^7 MSVs loaded with nanoliposome/EphA2-siRNA (15 μg of siRNA: triple dose). As a comparison, EphA2 siRNA encapsulated liposomes (5 μg of siRNA) were injected twice weekly as per a previously published study (97). Tumors were harvested at 3, 7, 14, and 21 days and EphA2 expression was analyzed by immunohistochemistry (Fig. 20). EphA2 expression was downregulated until 21 days (96). Moreover, the biological effect of sustained downregulation of EphA2 was determined by assessing the microvessel density (CD31) and cell proliferation (Ki67) (Fig. 21). Both microvessel density (a and c) and cell proliferation (b and d) were significantly reduced in tumor when treated with a single administration of the MSV-loaded with EphA2 siRNA encapsulated liposomes $**P < 0.001$ (Fig. 21). Similar effect by EphA2 siRNA encapsulated liposomes alone was achieved by three times the siRNA dosage (twice a week injections).

Figure 20. Systemic delivery of EphA2-siRNA using MSV. Mice (n=3 per time point) bearing SKOV3ip1 orthotopic ovarian tumors were injected with MSV-EphA2-siRNA or left nontreated. Immunohistochemical analysis of EphA2 expression in the SKOV-3 tumor. Images were taken at original magnification of $\times 400$.

Reproduced with permission from Cancer Research, Tanaka et al, 2010, (96).

Copyright American Association of Cancer Research 2010.

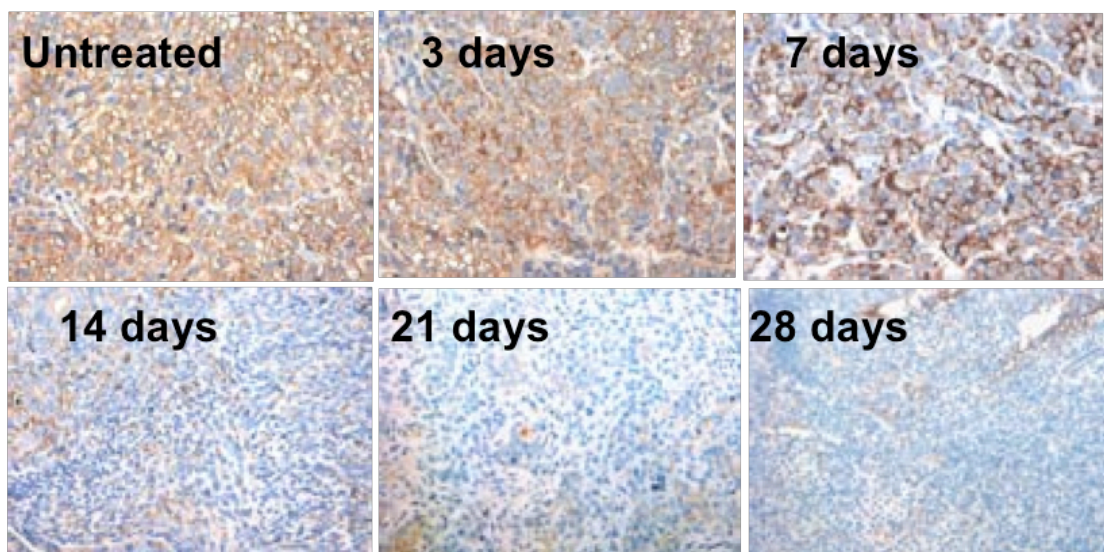
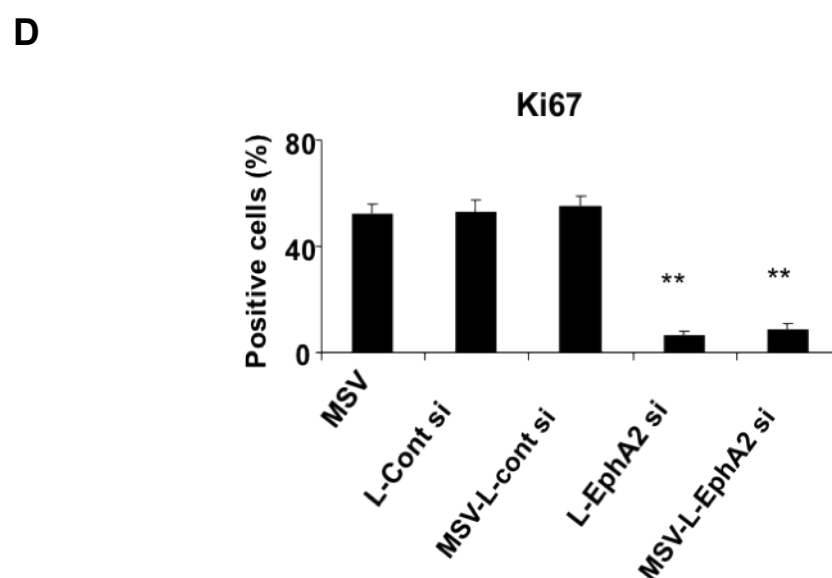
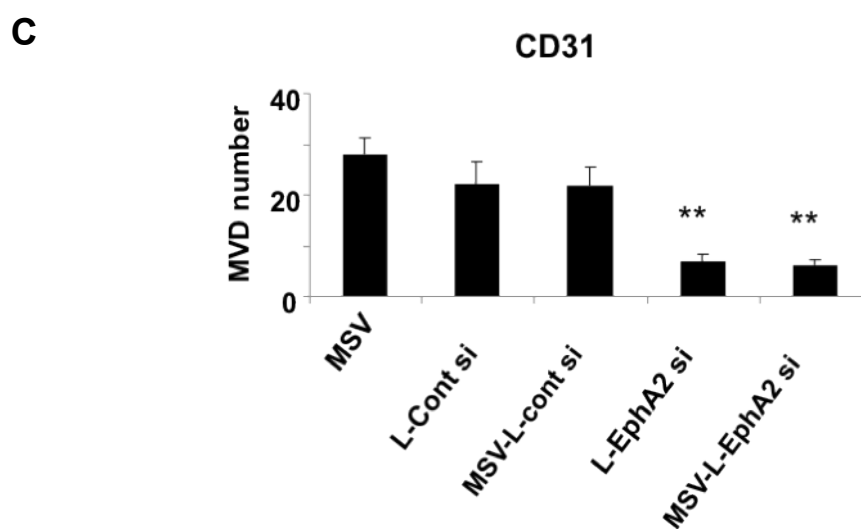
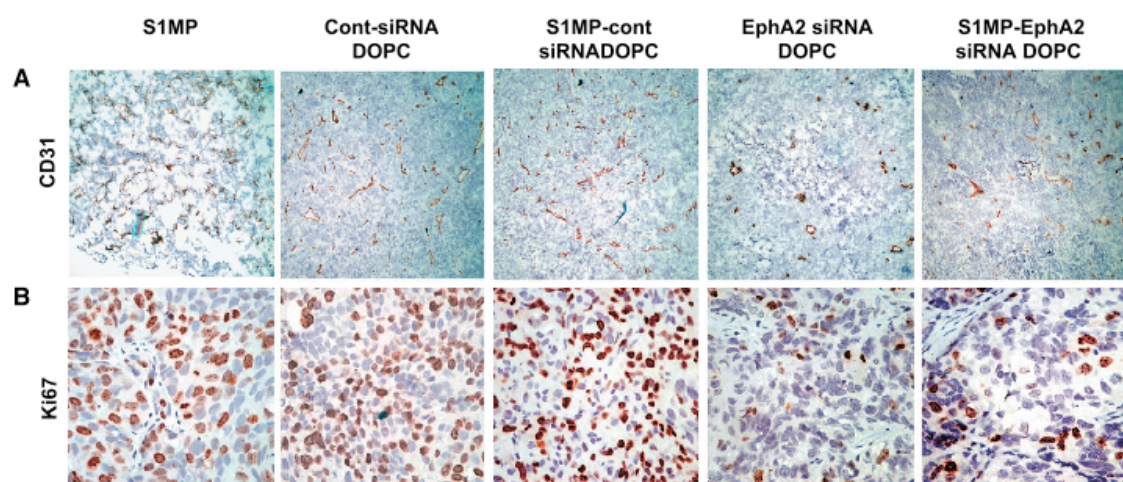


Figure 21. Effect of sustained siRNA delivery on angiogenesis and cell proliferation. Tumors from animals with the SKOV3ip1 ovarian tumor were examined for **(A)** microvessel density (CD31) and **(B)** cell proliferation (Ki67). Representative sections from each treatment group are shown (final magnification= x100 for CD31 and x400 for Ki67), with mean number of vessels per field or mean % of proliferative cells, summarized in the graph at the bottom **(C-D)**. Five different fields per slides at least three individual tumors per treatment group were examined.

Cont si – control siRNA, EphA2 si – siRNA against EphA2, L - liposome.

Reproduced with permission from Cancer Research, Tanaka et al, 2010, (96).

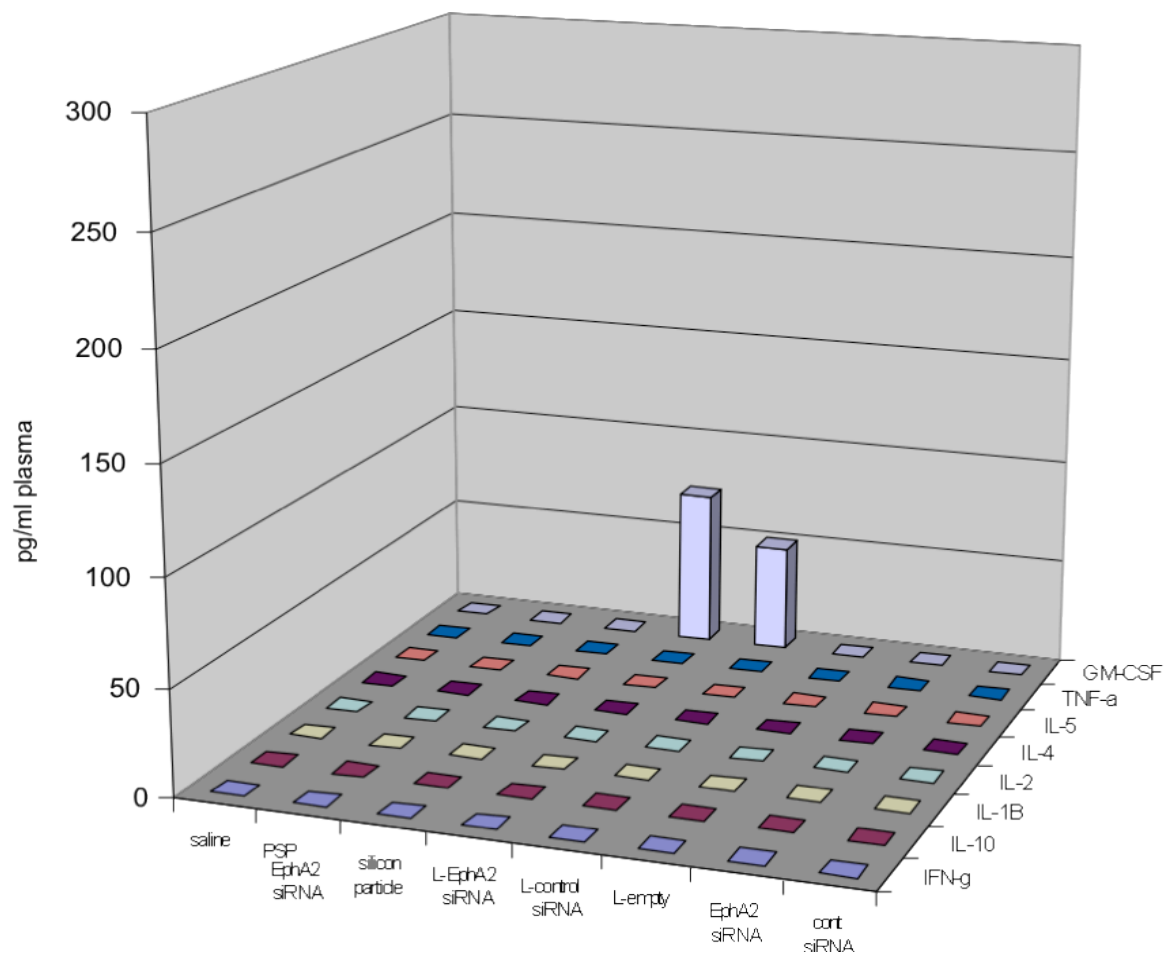
Copyright American Association of Cancer Research 2010.



3.1.4 Biocompatibility of MSV loaded EphA2-siRNA

We next tested the biocompatibility of multistage delivery system following i.v. administration of therapeutic dose of MSV-EphA2-siRNA. The cytokine levels in the plasma were analyzed after 5 hours post injection. Cytokine levels in the mice injected with MSV-EphA2-siRNA were similar to other controls (Fig. 22). Interestingly, liposome injection alone (both L-control siRNA and L-EphA2 siRNA) resulted in elevation in GM-CSF levels, which did not occur for MSV-EphA2-siRNA injection. These data indicate that MSV-loaded liposomal siRNA induced no significant levels of inflammatory cytokines and on the contrary reduced liposome-mediated inflammatory response.

Figure 22. Cytokine analysis of MSV loaded liposome-siRNA. Following i.v. injection of MSV-EphA2-siRNA into FBV/N mice (n=4), the serum was collected 5 hours after injection and the plasma was analyzed for different inflammatory cytokines. Data represented as picograms/ml of plasma.



3.2. Identification of E-selectin thioaptamer

3.2.1 Synthesis of thioaptamer library

A single-stranded library consisting of $\sim 10^{14}$ different sequences was chemically synthesized from a 73-mer DNA template containing a 30-nucleotide random region flanked by 21-mer and 23-mer polymerase chain reaction (PCR) primer regions.

5' Primer – N₃₀ – Primer 3' (10¹⁴ sequences)

The library was PCR amplified using a mixture of dATP, dTTP, dCTP, and dGTP and biotinylated forward primer to obtain a thio-substituted library. The resulting PCR products contained monothio-phosphate substitutions (in the Sp configuration) on the 5' side of every dA residue with the exception of the primer region on the non-template strand. These double stranded PCR products were then incubated with streptavidin-coated beads to separate the unbiotinylated single strand from the double stranded DNA. The combinatorial library was next used to screen for a thioaptamer ligands against E-selectin.

For the identification of E-selectin thioaptamer, a two-step selection strategy comprising of a recombinant protein-based screening followed by a cell-based selection was employed.

3.2.2 Screening with recombinant E-selectin protein

The TA that binds to E-selectin recombinant protein was screened from the TA library using a solution-based filter binding method. The recombinant human E-selectin protein was incubated with TA library and filtered through the nitrocellulose membrane to remove unbound TAs. The TA-E-selectin complex retained on the filter membrane was eluted and used as the template for PCR amplification. This selection cycle was repeated for a total of 10 times and the stringency of the selection was elevated gradually at each iterative cycle by decreasing the amount of E-selectin protein and incubation time (Fig. 24). The TA libraries obtained after round 5 and 10 were PCR amplified and subcloned into plasmid vector for DNA sequences. After 10 iterative cycles a total of 35 TAs were isolated and sequenced. Based on their primary sequences, the TAs were aligned using ClustalW algorithm (Fig. 24) and a cladogram tree was generated in which the 35 sequences were grouped into 14 families (Fig. 25). Based on the lowest predicted free energy of the secondary structures of the TAs, one TA from each family was selected and common sequence motifs were identified (Fig. 26). These 14 TAs were amplified by PCR with Cy-3 labeled reverse primer for the second step of cell-based selection to identify the TA sequences that specifically bind to E-selectin on the surface of endothelial cells.

Figure 23. Schematic representation of the iterative process to screen thioaptamers. The process is based on the SELEX process where the TA library is incubated with the target protein. The bound DNA is enriched after repeated washing steps and amplified by PCR reaction. The cycle is iteratively repeated several times to isolate high binders to target protein.

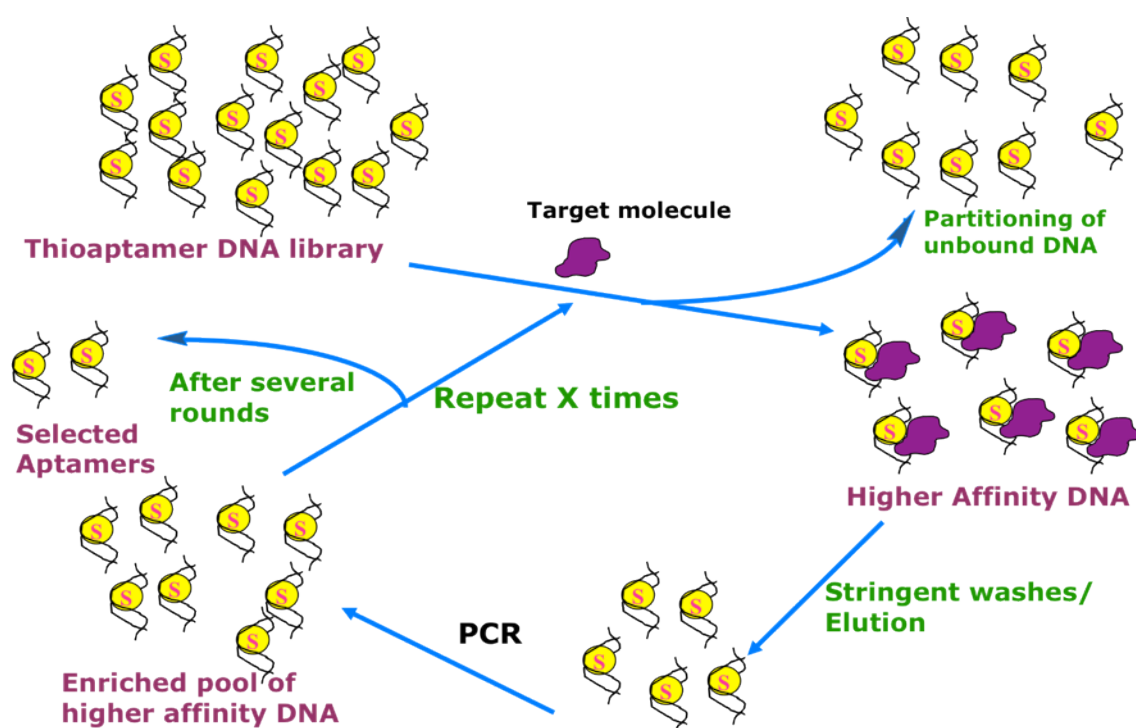


Figure 24. ClustalW alignment of the selected sequences after 10th round.

After the 10th round of selection, 35 clones were selected and their sequences were identified. The PCR primer regions in the sequences are underlined.

Reproduced with permission from PLoS ONE, Mann et al, 2010, (96). Copyright Public Library of Science 2010.

TA-1 CGCTCGGATCGATAAGCTTCGATCCCACTCTCCCGTTCACTTCTCCTCACGTCACGGATCCTCTAGAGCACTG
TA-2 CGCTCGGATCGATAAGCTTCGACCTACTACACCATCTCACCTCAACCCTCGTCACGGATCCTCTAGAGCACTG
TA-3 CGCTCGGATCGATAAGCTTCGTCGCCCTTACACTCCACATCAAGCCGCCGTCACGGATCCTCTAGAGCACTG
TA-4 CGCTCGGATCGATAAGCTTCGTCCCCGTCTTTCTCTCCCTTCCCTCGGGCACGGGTCCTCTAGAGCACTG
TA-5 CGCTCGGATCGATAAGCTTCGTCTCTCCCCCTCTTACCCTCTCCTGTACCGTCACGGATCCTCTAGAGCACTG
TA-6 CGCTCGGATCGATAAGCTTCGCTCCACTCTCCCTTCACTCTACCCACCCGTCACGGATCCTCTAGAGCACTG
TA-7 CGCTCGGATCGATAAGCTTCGGCCCTACACTCACCTCACCCAGACACACCGTCACGGATCCTCTAGAGCACTG
TA-8 CGCTCGGATCGATAAGCTTCGCCCTTCACTCTACCTTCGCCTCTGCACACGTCACGGATCCTCTAGAGCACTG
TA-9 CGCTCGGATCGATAAGCTTCGCCCTCCCTATACCACTGTCAACTTCCACTGTCACGGATCCTCTAGAGCACT
TA-10 CGCTCGGATCGATAAGCTTCGTCTCTCTCTCGTGTATCCACTCCACACAGTCACGGATCCTCTAGAGCACTG
TA-11 CGCTCGGATCGATAAGCTTCGGGGCTCTTCTCTCAATTACCTCACACAGTCACGGATCCTCTAGAGCACT
TA-12 CGCTCGGATCGATAAGCTTCGTCTTTCTTCTCTCTCTTCCATCTAACGTCACGGATCCTCTAGAGCACTG
TA-13 CGCTCGGATCGATAAGCTTCGCCTGCACCTCCACCTACACACTAAACGCGGTACGGATCCTCTAGAGCACTG
TA-14 CGCTCGGATCGATAAGCTTCGTCTCCCTCTTCTCTCTCTCGTTACCGTCACGGATCCTCTAGAGCACTG
TA-15 CGCTCGGATCGATAAGCTTCGTCTCTTCCCTCTCCACGCCACCCGAACGTCACGGATCCTCTAGAGCACTG
TA-16 CGCTCGGATCGATAAGCTTCGTCTCTCCATTTCCCTTCAATTCACCTCGTCACGGATCCTCTAGAGCACTG
TA-17 CGCTCGGATCGATAAGCTTCGCCCTTACCCCATCTCCCTTACCTTACGTCACGGATCCTCTAGAGCACTG
TA-18 CGCTCGGATCGATAAGCTTCGCCCTTCTCCACTTCTACTCTATACCCTCTCGTCACGGATCCTCTAGAGCACTG
TA-19 CGCTCGGATCGATAAGCTTCGCCCTTCTCCACTTCTACTCTATACCCTCTCGTCACGGATCCTCTAGAGCACTG
TA-20 CGCTCGGATCGATAAGCTTCGGCCTTCTCCTGGACTCCACTTCACTCCGTGTCACGGATCCTCTAGAGCACTG
TA-21 CGCTCGGATCGATAAGCTTCGCCTCCCACTTCCACATCCACCACTCGAACGTCACGGATCCTCTAGAGCACTG
TA-22 CGCTCGGATCGATAAGCTTCGACCTCCCCTCTTCACTCCATCTCCACCCGTCACGGATCCTCTAGAGCACTG
TA-23 CGCTCGGATCGATAAGCTTCGTCTCCCCCTTCCATTTCACTTTCCCCCTCGTCACGGATCCTCTAGAGCACTG
TA-24 CGCTCGGATCGATAAGCTTCGTCTCTCTCTCCATCACCTTCCACCTTCCGGTCACGTACGGATCCTCTAGAGCACTG
TA-25 CGCTCGGATCGATAAGCTTCGCCCTCCCTCTCCATCCATTCCCGTCACGTACGGATCCTCTAGAGCACTG
TA-26 CGCTCGGATCGATAAGCTTCGTTCCGCACTCTCCATCCTCCCTTACACGTACGGATCCTCTAGAGCACTG
TA-27 CGCTCGGATCGATAAGCTTCGCCCTTCCCTTCTTCTCTCTACCGCACACGTACGGATCCTCTAGAGCACTG
TA-28 CGCTCGGATCGATAAGCTTCGTCCCTTTACCCGCTCTACATCCCGCTCGTCACGGATCCTCTAGAGCACTG
TA-29 CGCTCGGATCGATAAGCTTCGTCCGTCTATACCCACACTCGCCGTCACGGATCCTCTAGAGCACTG
TA-30 CGCTCGGATCGATAAGCTTCGTCTTCCCAGTTCCATCTTATCTCTCTCGGGTCACGGATCCTCTAGAGCACTG
TA-31 CGCTCGGATCGATAAGCTTCGGCCCCACACTCAACACACGCGCTCCGCGTCACGGATCCTCTAGAGCACTG
TA-32 CGTTGGGATGGATAAGTTTGACCTCTCTCGTTCCCTTTCTCTTTACGTCACGGATCCTCTAGAGCACTG
TA-33 CGCTCGGATCGATAAGCTTCGACCTCTACCCATCAATCTCCACACCTAGGTCACGGATCCTCTAGAGCACTG
TA-34 CGCTCGGATCGATAAGCTTCGTCCCTTCCACATCCACAACCTTACCCAACGTCACGGATCCTCTAGAGCACTG
TA-35 CGCTCGGATCGATAAGCTTCGTCTTTTATTCCCTTACCTGCTAGACTCCACGTCACGGATCCTCTAGAGCACTG
TA-36 CGCTCGGATCGATAAGCTTCGCCCCCGACCACTCATGCCGTCTACCCGTCACGGATCCTCTAGAGCACTG

Figure 25. Cladogram of the selected sequences after round 10. The sequences from 10th round of selection was aligned by ClustalW. Based on the Phylogeny of the sequences they were grouped into 14 different families.

Reproduced with permission from PLoS ONE, Mann et al, 2010, (96). Copyright Public Library of Science 2010.

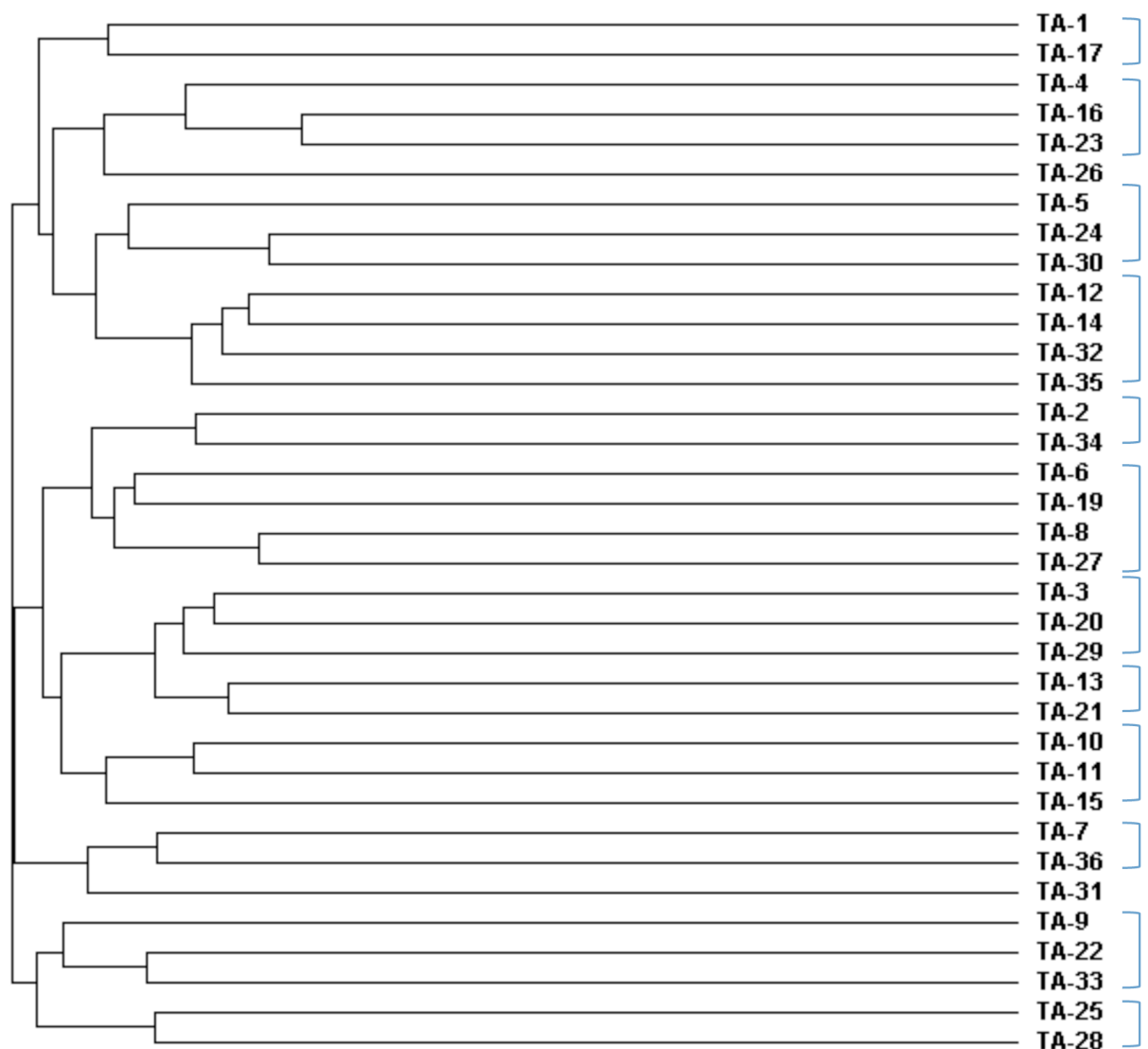


Figure 26. Common sequence motifs among 14 TA candidates. (A) The 14 sequences belonging to each family from the cladogram are aligned by ClustalW program. **(B)** Common sequence motifs identified among the 14 sequences.

Reproduced with permission from PLoS ONE, Mann et al, 2010, (96). Copyright Public Library of Science 2010.

A

```

TA-31  -GCCCCACACCTCCAACACACGCGCCTCCGC----
TA-30   TCCTTCCCAGTTCCATCTTATCCTCCTCGG----
TA-2    -ACCCTACTACACCATCTCACCTCAACCCTC----
TA-7    -GCCCTAG-ACTCACCCTCACCCAGACACACC---
TA-9    ---CCCTCCCCTATACCACTGTCAACTTCCACT--
TA-13   ---CCTGCACCTCCACCCTACACACTAAACGCG--
TA-1    ----ATCCCACTCTCCCGTTCACTTCTCCTCAC--
TA-6    ----CTCCACTCCTCCCTTCACT-CTACCCACCC
TA-14   --TCTCCCTCCTT-CTCCTCTCTGCT-TCACC-
TA-4    --TCCCCGTCCTTTCTCTTCCCTTCCCC-TCGG--
TA-26   --TTCCCGCACTCCTCCATCCTTCCTTC-ACAC-
TA-25   ---CCCTCCCCTCCTCCATCCATTCCCCGTCAC--
TA-20   --GCCTTCTCCTGGACTCCACTTCACTCCGTG---
TA-10   ---TCCTCTCTCTCGTGTA-TCCACTCCACACA-

```

B

Sequence Motif	TA Sequence identifier
ACT(T/C)C(T/A)C(T/C)TCAC	(1,20)
TCCTC	(1,14,6,25,26,10,30)
TCCC(G/T)T	(1,4,6,26)
TCCCC(T/G)	(4,9,25)
ACCC (T/A)(A/C)	(2,6,13,7)
ACT(A/T/C) C	(1,26,6,20,20,13,10)
TCCC(G/T)	(1,14,4,26,6,30)
ATCC	(1,26,25,10)
CCCGT(T/C)	(1,4,25)
CTTC(T/A)	(1,14,26,6,20,30)
GCCC(T/C)ACAC	(31,7)
ACACC	(31,7,2)
CTCCA	(31.13.6.26.25.20.10)

3.2.3. Cell-based TA screening

The second step in the screening was a cell-based selection of the 14 TAs identified in the first step (81). To identify the TA sequences that bind to E-selectin on the surface of endothelial cells, there were two strategies that were considered for achieving over expression of E-selectin on the surface of endothelial cells

1. Induction of cells with cytokines like TNF- α , IL-1 β (69, 99)
2. Development of an inducible system of cells to precisely control expression of E-selectin

The limitation of induction of E-selectin by cytokines is that firstly, it results in non-uniform stimulation of E-selectin in cells and secondly, it also causes upregulation of multiple surface molecules which can interfere in the screening of E-selectin specific thioaptamer ligands. For these reasons, a Tet-on inducible E-selectin endothelial cell line (ES-Endo) was developed (Fig. 27).

3.2.3.1 Development of E-selectin inducible endothelial system

A) Construction of E-selectin expression vector

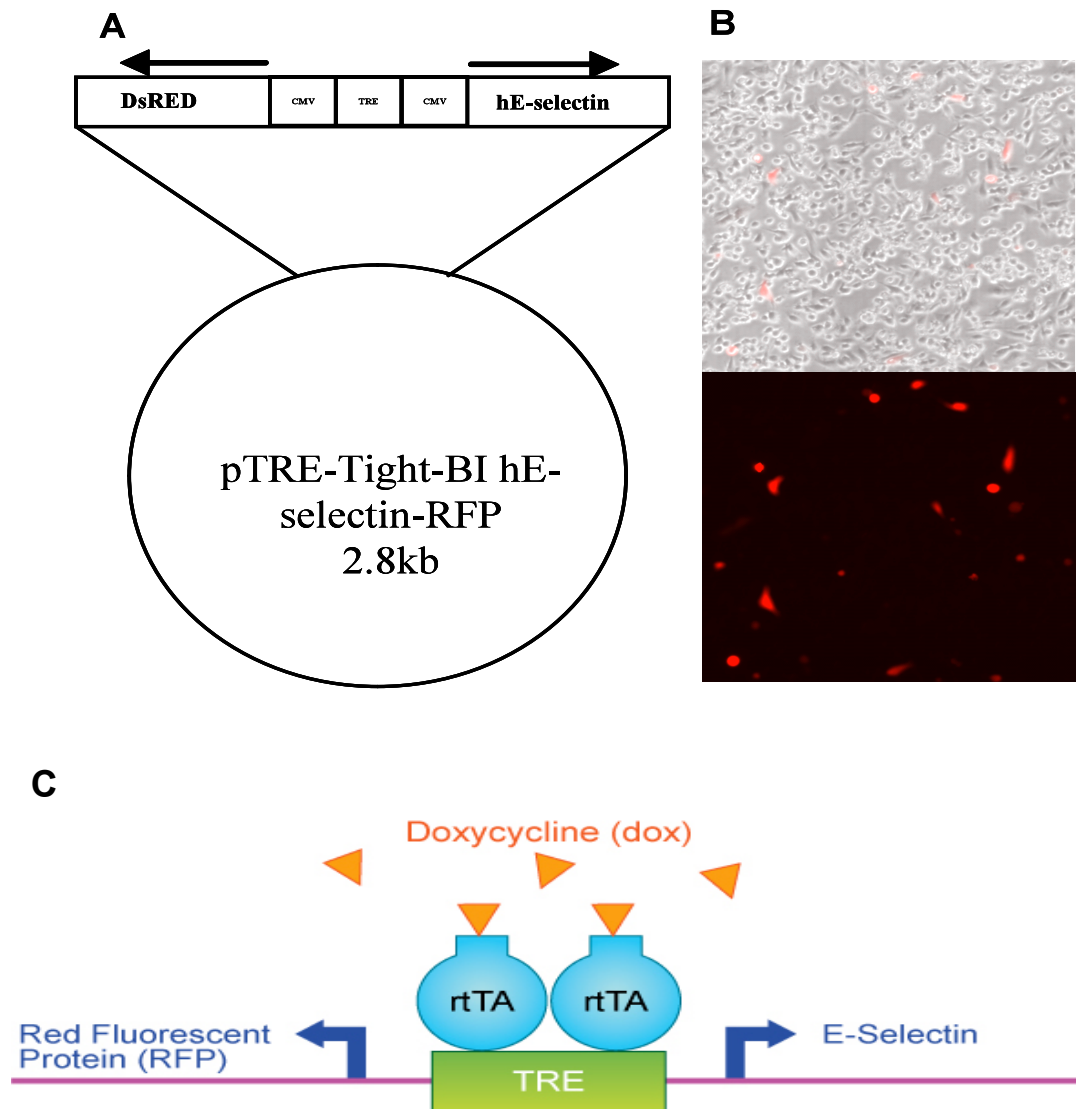
The following steps were carried out for the construction of E-selectin expression vector:

- The cDNA of E-selectin was obtained and the E-selectin ORF was amplified by PCR and cloned into TOPO blunt vector.
- Positive clones containing the gene were selected and sequenced and verified with Pubmed database (Accession NM_000450). The gene

sequence of E-selectin positive clone was 100% intact and no mutation was observed.

- E-sel TOPO pBlunt was digested with *Mlu* I and *Sal* I to obtain the E-selectin gene for subsequent insertion into pTRE-Dsred expression vector (Fig. 27A)
- A clone containing E-selectin-dsred was selected and verified to contain the construct by double digestion with above enzymes
- The function of the pTRE-Tight-BI hE-selectin-RFP positive clone was confirmed by transient transfection of the plasmid into tet-on MDA-MB-231 breast cancer cell line established previously (100), and the cells were treated with 1000ng of doxycycline overnight.
- MDA-MB-231 cells expressed red fluorescence protein in response to 1000ng doxycycline (Fig. 27B). This data supports that the isolated pTRE-Tight-BI hE-selectin-RFP positive clone was functional.

Figure 27. Construction of E-selectin expression vector. (A) Plasmid map of pTRE-Tight-BI human E-selectin-RFP. **(B)** transient transfection of pTRE-Tight-BI human E-selectin-RFP plasmid in Tet-on MDA-MB-231 cells. **(C)** Mechanism of Tet-on inducible system.

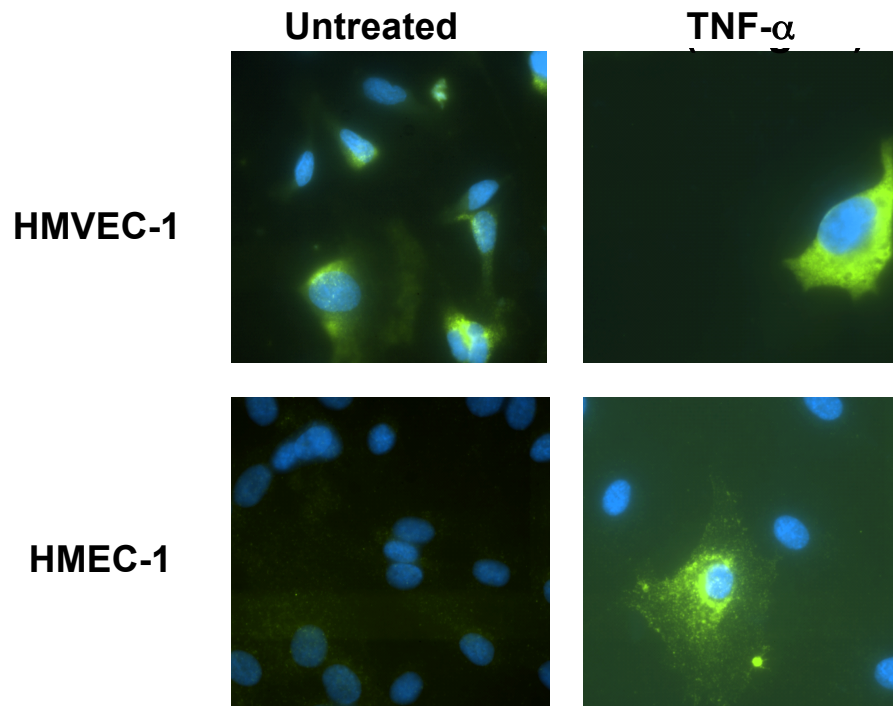


B) Development of Tet-on endothelial cells

Two immortalized human endothelial cell lines were tested (HMVEC and HMEC) for developing an E-selectin inducible cell line. Human microvasculature endothelial cell line (HMVEC) was previously immortalized by stable transfection of telomerase reverse transcriptase (TERT) gene (101) and the human dermal microvasculature endothelial cell line (HMEC) was immortalized by SV-40 (102).

First, immunofluorescence was performed to test the basal expression level of E-selectin in these human endothelial cell lines. Both HMVEC and HMEC were incubated in the presence of 10 μg of $\text{TNF-}\alpha$ for 5 hours to induce E-selectin expression. After brief fixation, the cells were stained with antibody against E-selectin. E-selectin expression was rapidly induced by pro-inflammatory cytokine ($\text{TNF-}\alpha$) in both HMVEC and HMEC cells (Fig. 28). However, the baseline E-selectin expression level for HMVEC cells was minimal, and the induction of E-selectin expression was very scattered and was only seen in a total of 20-30 % of the cells (Fig. 28). This data suggests that E-selectin induction by cytokine through $\text{NF-}\kappa\text{B}$ may require additional cellular mechanisms. In contrast, HMEC cells responded to $\text{TNF-}\alpha$ induction more sensitively and evenly, however, the basal E-selectin expression level was higher than HMVEC. HMVEC cells with much lower baseline expression of E-selectin than HMEC were selected for development of E-selectin inducible system.

Figure 28. Immunofluorescence of E-selectin in two endothelial cell lines (HMEC and HMVEC). Cells were induced with TNF (10 ng/ml) for 5 hours and fixed and stained for E-selectin expression. Green - E-selectin and Blue - Hoechst 33342.



Next, HMVEC were stably transfected with an rtTA plasmid and the positive clones were screened. To confirm the expression and function of the rtTA protein, the clones were infected with 50 MOI of adenoviral TRE- β -galactosidase with 1000 ng of doxycycline treatment. The β -galactosidase activity in the clones was measured using ONPG as the substrate. Clone 32 showed the highest activity (Fig. 29A). To further confirm the expression of rtTA, western blotting was performed using antibody against rtTA and clone 32 showed the highest rtTA expression level (Fig. 29B). As a second step of the cloning, the clone 32 was co-transfected with pTRE-Tight-BI-human E-selectin-RFP and the stable clone was isolated after two weeks. The stable clone expressed the RFP after treatment with doxycycline as visualized by fluorescent microscopy (Fig. 29C).

To examine the ability to induce E-selectin overexpression in the stable HMVEC clone of Tet-on inducible bi-directional RFP/E-selectin, the cells were incubated with 1000 ng of doxycycline for 5 hours and E-selectin expression was determined by immunofluorescence and western blotting (Fig. 30). E-selectin was expressed on the surface of the cells in response to doxycycline, whereas no E-selectin expression was seen without treatment with doxycycline.

Figure 29. Development of tet-on E-selectin inducible endothelial cells. (A) Screening of tet-on positive cells. **(B)** Tet-on protein expression in HMVEC clone 32. **(C)** RFP expression in HMVEC clone 32 in response to doxycycline.

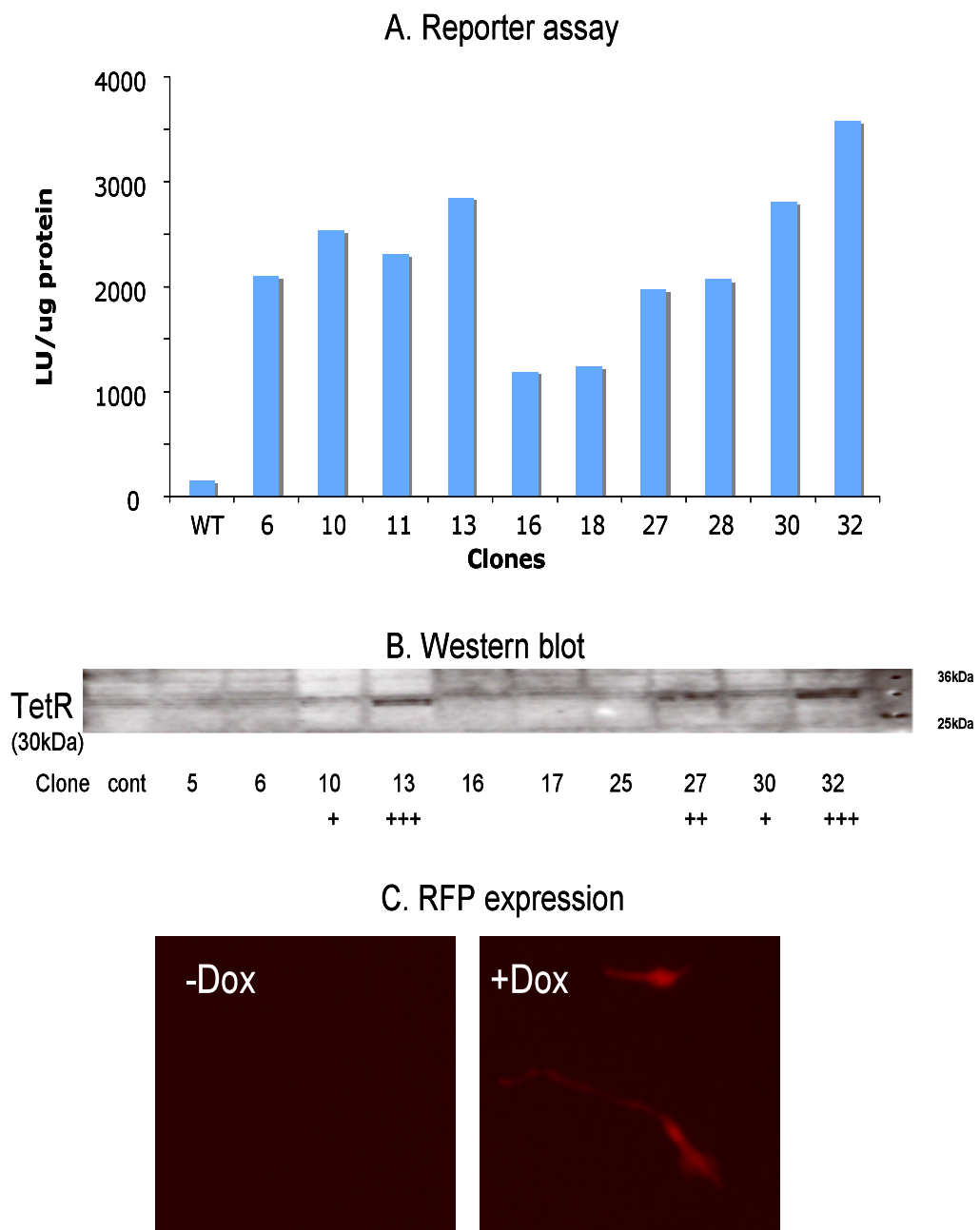
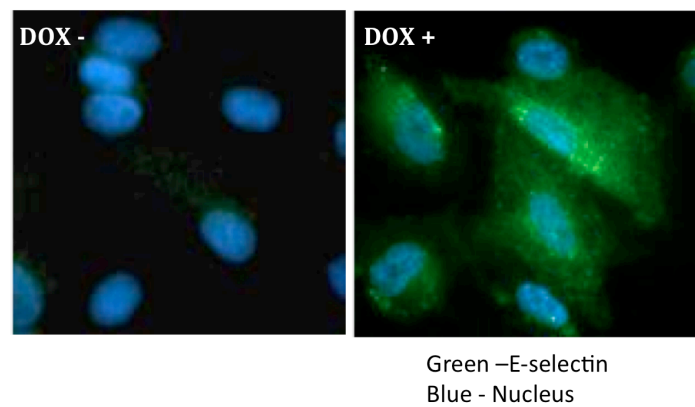


Figure 30. Doxycycline inducible E-selectin expression in ES-Endo. (A)

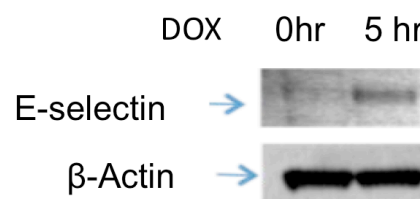
Immunofluorescence to analyze E-selectin expression in ES-Endo after induction with doxycycline 1000 ng/ml Green – E-selectin; Blue - Hoechst 33342.

(B) Western blotting of E-selectin protein expression in the ES-Endo cells after 5 hour induction with doxycycline.

A



B



3.2.3.2 TA selection using E-selectin inducible endothelial cells

To utilize the E-selectin inducible endothelial cells (ES-Endo) for the second step of TA selection, first the doxycycline dose dependent induction of E-selectin expression was analyzed. For this induction in E-selectin expression on the plasma membrane was analyzed on ES-Endo incubated with increasing concentrations of doxycycline (0–2000 ng/ml) for 5 hours. As a reference for the physiological level of E-selectin expression, the cells were also treated with TNF- α (10 ng/ml) for 5 hours. E-selectin expression was analyzed using immunofluorescent staining with anti-E-selectin antibody. When treated with 500 ng/ml of doxycycline, upregulation of E-selectin expression was observed predominantly on the cell membrane, and the expression level increased in a doxycycline concentration dependent manner (Fig. 31). At doxycycline concentration of 2000 ng/ml, the level of E-selectin expression was the highest and equivalent to TNF- α treated cells therefore this concentration of doxycycline was used for all the subsequent experiments. Due to the leakiness of the inducible system, the baseline level of E-selectin expression was slightly higher than wild type cells in the absence of doxycycline.

Next step was to select out of the 14 TAs isolated in the first step, the TA that binds to E-selectin specifically. For this ES-Endo were pre-incubated with doxycycline and then with each of the 14 TAs (100 nM) were added for 20 minutes at 37 °C. To analyze the binding and specificity of each TA, the fluorescent intensity associated with the cells was compared using fluorescent microscopy (Table 2).

Between the 14 TAs tested, TA-1 exhibited the highest binding, and this binding was doxycycline dose-dependent. The number and brightness of the

speckles increased proportionally to the doxycycline concentration up to 2000 ng/ml (Fig. 31), suggesting E-selectin specific binding. Similar binding pattern of TA-1 was also observed with TNF- α induction of ES-Endo. Although all the TAs were isolated based on their ability to bind human recombinant E-selectin protein, the rest of the TAs showed weak doxycycline dependent with high background binding (TA 20, 31) (Table 2). Based on these results, TA-1 was selected as the top candidate for E-selectin thioaptamer 1 (ESTA-1) and further characterization studies of ESTA-1 were conducted.

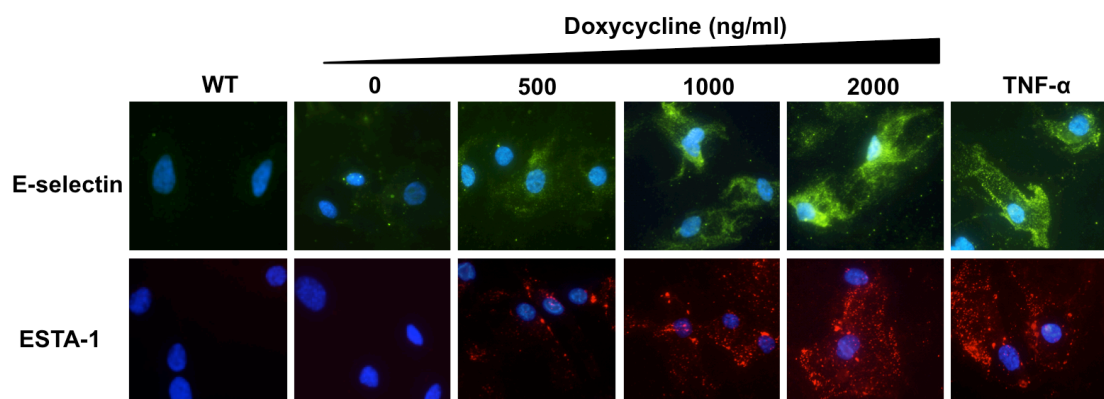
Table 2. Comparison of TA binding to E-selectin expressing ES-Endo. The table shows the calculated lowest free energy using MFold algorithm for each 14 TA sequences, their relative binding, and relative specificities to E-selectin expressing cells. The relative binding affinity was determined by the amount of fluorescence detected per field of view (final magnification 60x) in the cell based binding assay and the relative specificity was defined by the degree of doxycycline dose dependent effect on TA binding. + indicates the binding strength or specificity.

Reproduced with permission from PLoS ONE, Mann et al, 2010, (96). Copyright Public Library of Science 2010.

Sequence Identifier	ΔG (Kcal/mol)	Relative Binding	Relative Specificity
TA- 1	-10.72	+++	+++
TA-20	-7.98	+++	++
TA-31	-8.64	++	+
TA- 4	-7.25	+	-
TA-14	-6.31	+	-
TA-25	-6.25	+	-
TA- 6	-6.24	+	-
TA-10	-6.09	+	-
TA-30	-6.07	+	-
TA-26	-5.86	+	-
TA- 7	-5.49	+	-
TA-13	-4.68	+	-
TA- 2	-3.78	+	-
TA- 9	-3.62	+	-

Figure 31. E-selectin dependent binding of ESTA-1. ES-Endo cells were induced with different concentrations of doxycycline (0-2000 ng/ml) and analyzed for E-selectin expression and ESTA-1 binding. E-selectin overexpressing ES-Endo cells were incubated with Cy3-labeled ESTA-1 (100 nM) for 20 minutes at 37 °C. TNF- α (10 ng/ml) induced ES-Endo was used as a positive control. Blue, Hoechst 33342; Red, Cy3-labeled ESTA-1; Green, E-selectin.

Reproduced with permission from PLoS ONE, Mann et al, 2010, (96). Copyright Public Library of Science 2010.



We did two experiments to confirm that ESTA-1 binding on the ES-Endo cells was E-selectin specific. Firstly, we treated ES-Endo with different concentrations of E-selectin monoclonal antibody followed by incubation with 100 nM of ESTA-1. Pre-treatment and co-incubation with E-selectin antibody caused a significant reduction of ESTA-1 binding to ES-Endo as confirmed by the disappearance of the speckle pattern (Fig. 32). In contrast, there was no affect of normal IgG pre- treatment on ESTA-1 binding to the cells (Fig. 32). This data confirms that E-selectin antibody shares the binding site with ESTA-1 on the E-selectin protein.

Secondly, immunofluorescence of E-selectin was performed on induced ES-Endo that were incubated with ESTA-1. For this a different monoclonal antibody against E-selectin was used that does not compete with ESTA-1 binding. Partial colocalization of ESTA-1 (red fluorescence) with E-selectin (green fluorescence) was observed on the edge of the cells as seen in yellow merge, supporting ESTA-1 binding to E- selectin on the cell surface (Fig. 33). One of the possible reasons for only a partial colocalization of ESTA-1 and E-selectin can be the intracellular uptake of ESTA-1 following the initial cell surface binding. In fact, it is well documented that E-selectin undergoes recycle phase and is internalized to the intracellular organelles (endosomes and lysosomes) [34]. Confocal microscopy suggested that ESTA-1 maybe internalized as evidenced by appearance of speckles at different heights (Fig. 33B). These data confirmed that ESTA-1 binds to E-selectin protein.

Figure 32. Competitive E-selectin binding of ESTA-1 and E-selectin antibody. Blocking of ESTA-1 binding by E-selectin antibody. ES-Endo were pre-incubated (top panel) or co-incubated (bottom panel) with 25 mg of E-selectin antibody for 2 hours and incubated with 100 nM of ESTA-1 for 20 minutes. Unbound ESTAs were washed away and slides were prepared for fluorescent imaging to visualize the binding to ES-Endo cells. Blue, Hoechst 33342; Red, Cy3-labeled ESTA-1; Green, E-selectin.

Reproduced with permission from PLoS ONE, Mann et al, 2010, (96). Copyright Public Library of Science 2010.

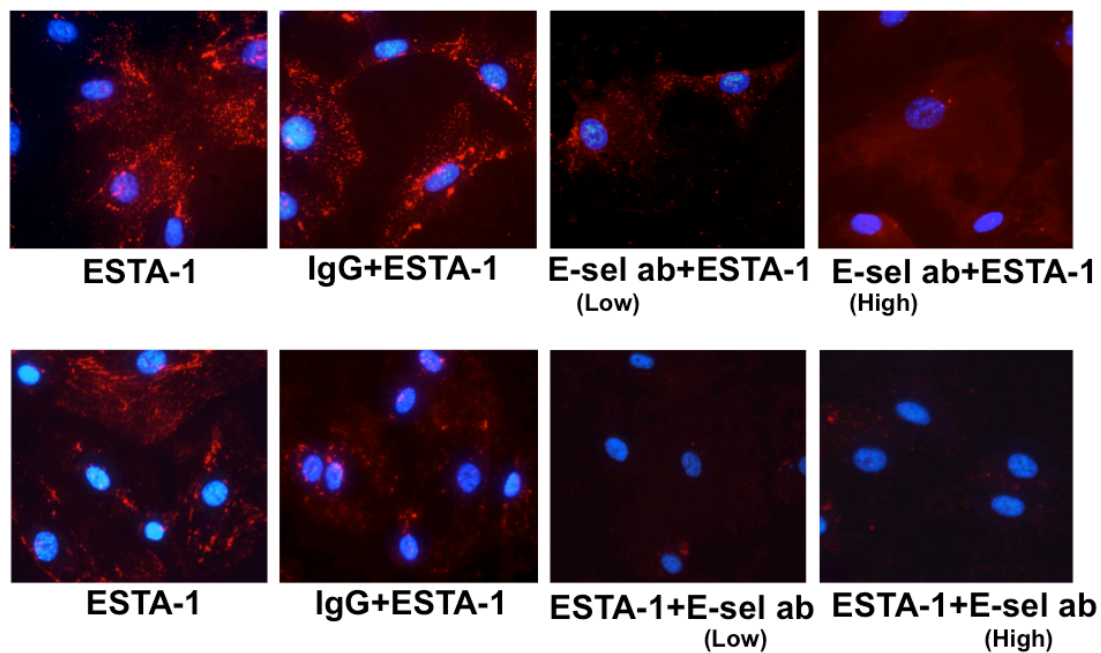
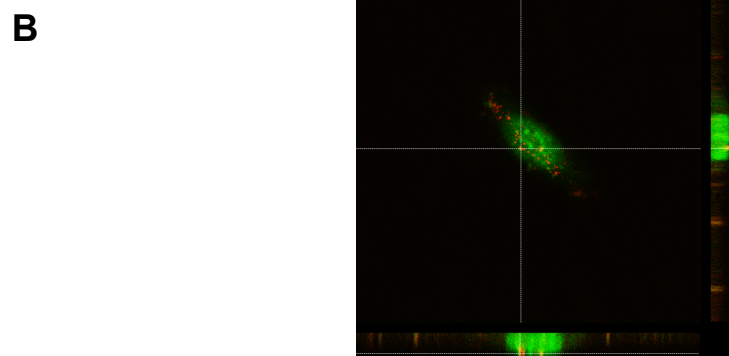
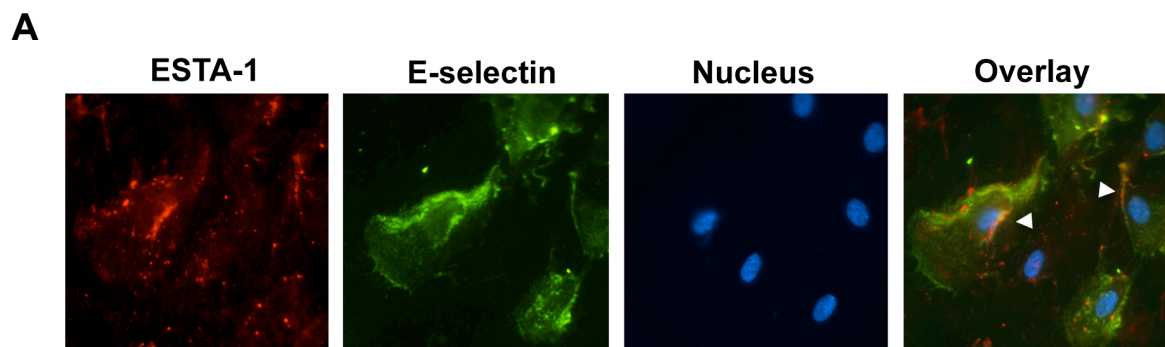


Figure 33. Colocalization of E-selectin expression and ESTA-1 binding. (A)

ES-Endo cells were treated with doxycycline (2000 ng/ml) and analyzed for ESTA-1 binding and E-selectin expression using immunofluorescence. Blue, Hoechst 33342; Red, Cy3-labeled ESTA-1; Green, E-selectin. **(B)** Confocal image of ESTA-1 binding to doxycycline induced ES-Endo cells. Red, Cy3-labeled ESTA-1; Green, Cytox nuclear staining.

Reproduced with permission from PLoS ONE, Mann et al, 2010, (96). Copyright Public Library of Science 2010.



3.2.4 Characterization of ESTA-1

Next, ESTA-1 primary sequence was analyzed (Figure 34A). Based on our analysis this sequence did not show any homology to the existing genes in the NCBI database. The predicted secondary structure of ESTA-1 was determined using the MFOLD computer simulation program (103). Based on MFOLD prediction, the structure of the ESTA-1 comprised of two stable hairpin loops with an estimated free-energy change of folding of -10.72 kcal/mol (Fig. 34B). Preliminary deletion studies of the stem loops suggest that these loops played an important role in binding to the E-selectin protein.

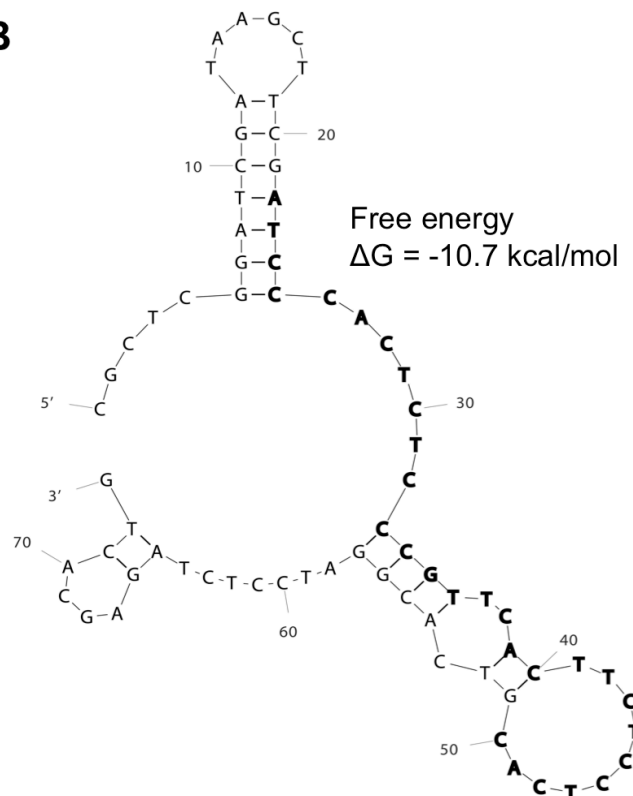
Figure 34. ESTA-1 sequence and the MFOLD predicted secondary structure. (A) ESTA-1 DNA sequence. All of the deoxy adenosine (dA) residues are modified monothio substituted with Rp configuration, with the exception of 5'-primer binding region in the sequence. (B) MFOLD predicted secondary structure of ESTA-1.

Reproduced with permission from PLoS ONE, Mann et al, 2010, (96). Copyright Public Library of Science 2010.

A

5'- CGCTCGGATCGATAAGCTTCG
 ATCCCACTCTCCCGTTCACTTCTCCTCAC
 GTCACGGATCCTCTAGAGCACTG -3'

B



3.2.5 Evaluation of binding affinity of ESTA-1 to E-selectin

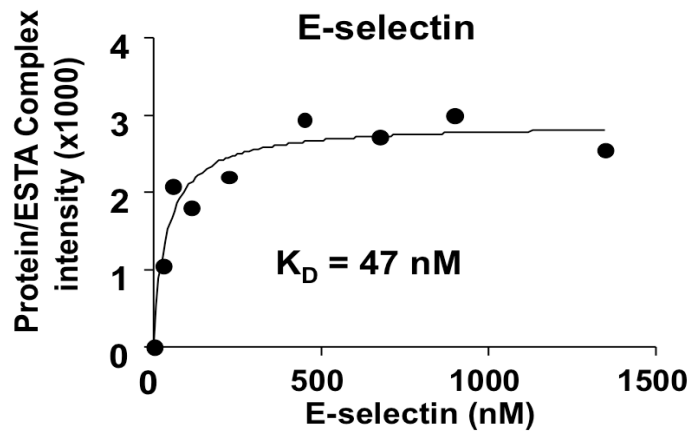
The binding affinity of ESTA-1 with all selectins was determined using electrophoretic mobility shift assay (EMSA). In this experiment, fixed amounts of ESTA-1 (4.6 pmoles) was mixed with increasing amounts (up to 22 pmoles) of recombinant proteins (E-, P-, L-selectin) to form a DNA/protein complex. The amount of ESTA-1/E-selectin protein complex formation was analyzed using EMSA. This complex increased when higher amount of recombinant E-selectin was added to the reaction with a corresponding decrease in the free (unbound) ESTA-1. Notably the amount of this complex reached saturation when the molar ratio of ESTA-1/E-selectin was 1:1. Based on the densitometric analysis of the unbound ESTA-1, the K_D for ESTA-1 binding to E-selectin was estimated to be 47 nM (Fig. 35A). Contrary to this, the binding of ESTA-1 to P-selectin showed very low affinity (estimated K_D = 13 μ M) under the same conditions and there was no detectable binding to L-selectin (Fig. 35B).

The nanomolar range of binding affinity of ESTA-1 for E-selectin on the endothelial cells was further confirmed under biological conditions, by incubating different concentrations of ESTA-1 (50 nM - 200 nM) with ES-Endo cells induced with doxycycline. A doxycycline dose dependent increase of ESTA-1 binding to the cells was observed that reached a maximum at 200 nM (Fig. 35C).

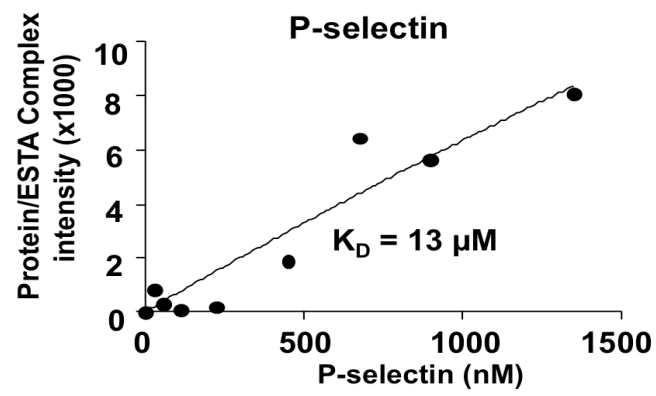
Figure 35. Evaluation of binding affinity of ESTA-1 to E-selectin. ESTA-1 (4.6 pmoles) and recombinant human E-selectin protein (up to 19 pmoles) were incubated and subjected to electrophoresis at 4 °C. The gels were stained with SYBR Gold nucleic acid stain and densitometric analysis of the unbound ESTA-1 was plotted. **(A)** E-selectin recombinant protein. **(B)** P-selectin recombinant protein. **(C)** ESTA-1 concentration dependent binding to ES-Endo. ES-Endo were incubated with doxycycline (1000 ng/ml) for 5 hours and then with indicated concentrations of Cy3-labeled ESTA-1 for 20 minutes. ESTA-1 binding was analyzed by fluorescent imaging. Red, Cy3-labeled ESTA-1; blue, Hoechst 33342.

Reproduced with permission from PLoS ONE, Mann et al, 2010, (96). Copyright Public Library of Science 2010.

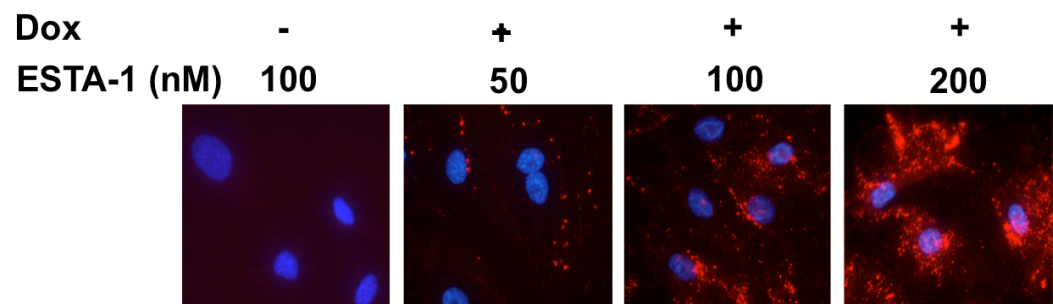
A



B



C



3.2.6 ESTA-1 binding to vascular E-selectin *in vivo*

Next step was to determine if ESTA-1 binds E-selectin *in vivo*. As mentioned earlier, E-selectin is constitutively expressed on bone marrow endothelium and in the normal organs; E-selectin is upregulated in the presence of inflammatory stimuli such as in the case of cancer. So prior to examining the ESTA-1 binding to these sites we first examined the E-selectin expression at these sites.

Firstly, bone marrow was isolated and immunohistochemical analysis was performed on paraffin-embedded sections that confirmed high constitutive E-selectin expression (Fig. 36A). These results are consistent with earlier published studies. Next, ESTA binding to E-selectin on the bone marrow endothelium was examined. ESTA-1 labeled with Cy-3 dye was intravenously injected into mice and the bone marrow was isolated and analyzed by a fluorescent microscope. A significantly high accumulation of ESTA-1 was observed in the bone marrow tissue (Fig. 36B). ESTA-1 accumulation in other organs was minimal.

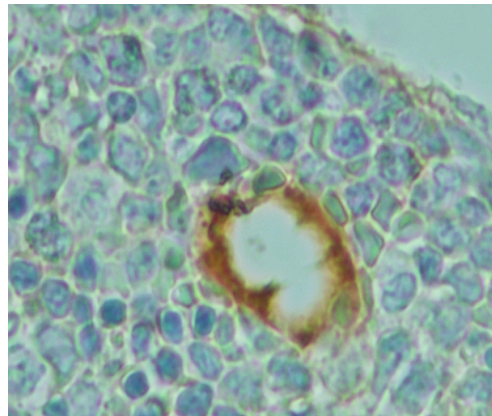
Similarly, a 4T1 breast tumor mouse model immunohistochemistry was performed to determine E-selectin expression. 4T1 tumor is characteristic for the presence of infiltrating leukocytes and macrophages. A high E-selectin expression was observed on the endothelial cells of the tumor-associated vasculature (Fig. 37A). Next, Cy-3 labeled ESTA-1 was intravenously injected into 4T1 mouse model, and the tumor was analyzed for ESTA-1 binding. ESTA-1 binding to the tumor vasculature was observed as evidenced by the speckled and punctate red pattern (Fig. 37B). No significant binding of ESTA-1 was observed in other organs including liver, spleen, kidney, lung, and heart. To

confirm that this was E-selectin specific binding, a pre-injection of E-selectin monoclonal antibody significantly reduced the ESTA-1 binding. Pre-injection of control IgG did not cause any inhibition in ESTA-1 binding.

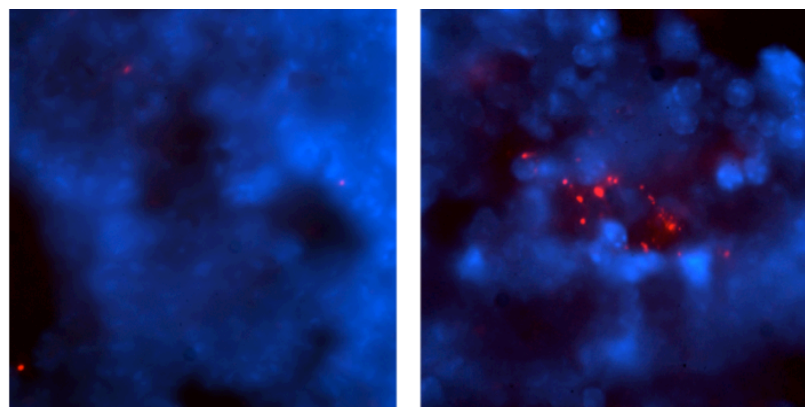
Figure 36. *In vivo* binding of ESTA-1 to bone marrow vasculature. (A)

Immunohistochemical analysis of paraffin embedded sections to analyze E-selectin expression on the vasculature of bone marrow. **(B)** *In vivo* binding of ESTA-1 to bone marrow vasculature. Bone marrow was isolated from the animals (n=3) and analyzed under a fluorescent microscope. Red, Cy3-labeled ESTA-1; blue, Hoechst 33342.

A



B

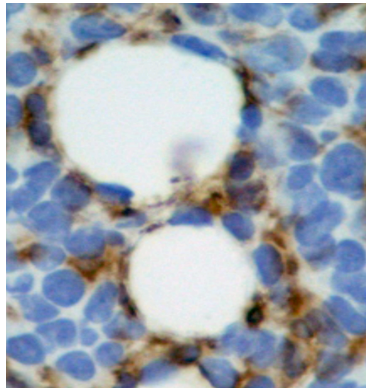


Saline

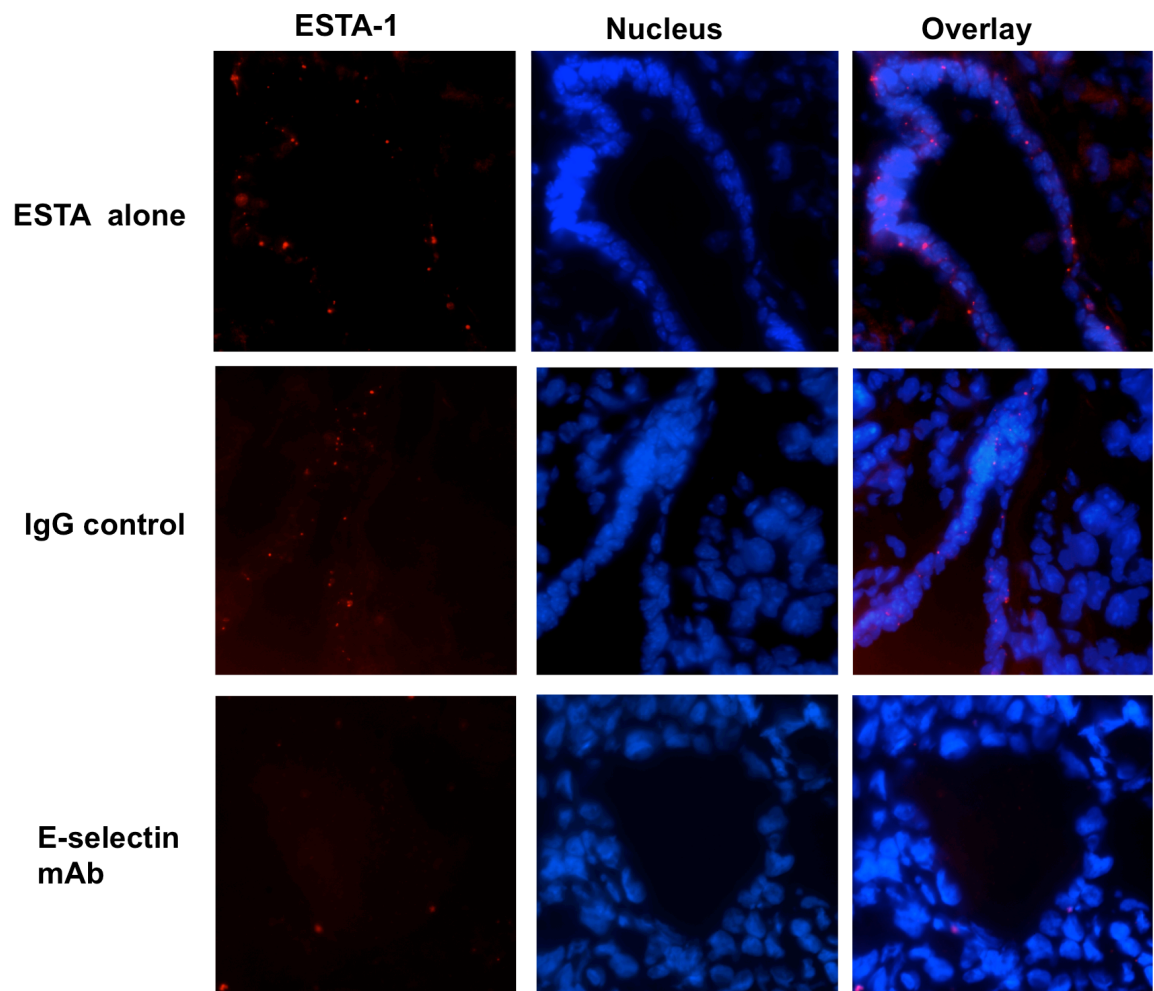
ESTA-1

Figure 37. *In vivo* binding of ESTA-1 to tumor vasculature. Sections derived from 4T1 xenograft model were examined for E-selectin expression and ESTA-1 binding. **(A)** Immunohistochemical analysis of paraffin embedded sections to analyze E-selectin expression on the vasculature of 4T1 xenograft. **(B)** ESTA-1 binding to 4T1 tumor vasculature. ESTA-1 was injected to mice (n = 3) via tail vein and tumor was isolated and the frozen sections (5 mm) were prepared to assess distribution of ESTA-1. Red, Cy3-labeled ESTA-1; blue, Hoechst 33342. *Reproduced with permission from PLoS ONE, Mann et al, 2010, (96). Copyright Public Library of Science 2010.*

A



B

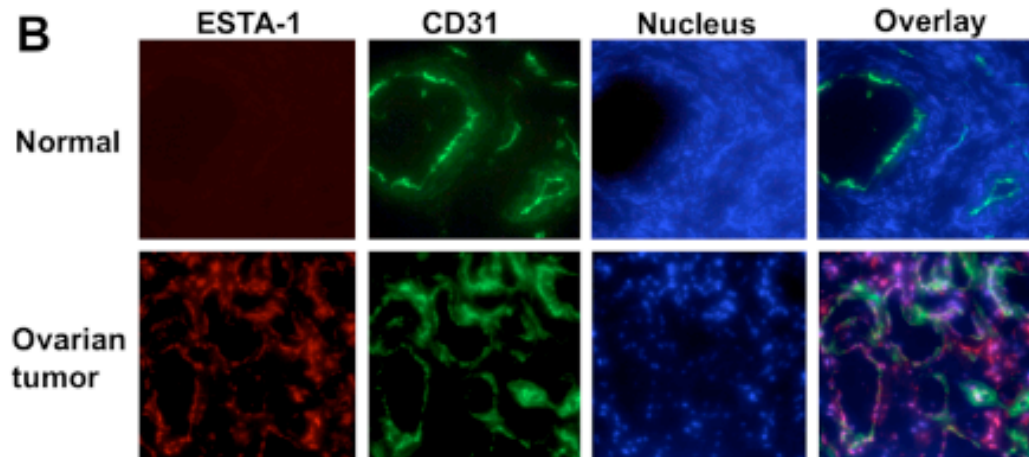
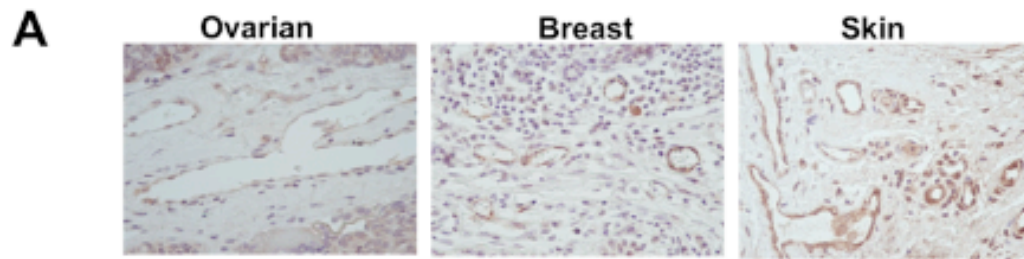


3.2.7 ESTA-1 binding to human tumor vasculature

Due to species differences in human and mouse selectin, ESTA-1 binding to the tumor vasculature using histological sections derived from human carcinomas was tested. Immunohistochemical analysis confirmed that approximately 70-80% of skin, ovarian and breast tumors showed positive E-selectin expression on the vasculature (Fig. 38 A and C). The incubation of the frozen sections with ESTA-1 showed intense binding on the vessels in ovarian carcinomas as evidenced by the co-localization with CD31 (Fig. 38B). In contrast, ESTA-1 binding was not observed in normal vessels. Similarly, high ESTA-1 binding was also observed to the tumor-associated vasculature in skin and breast carcinomas (Fig. 38C). ESTA-1 binding was almost absent in the normal human tissues, including the adrenal, pancreas, brain, lung, temporal lobe, breast, cervix, heart, kidney, stomach, thyroid, liver, placenta, salivary gland, skeletal muscle, small intestine, spleen, and uterus.

Figure 38. ESTA-1 binding to the human tumor vasculature. Frozen sections derived from human ovarian carcinomas and normal ovaries were examined for E-selectin expression and ESTA-1 binding. **(A)** Immunohistochemical analysis for E-selectin expression on the vasculature of ovarian carcinoma. **(B)** ESTA-1 binding to tumor vasculature of ovarian carcinoma. Green, CD31; Red, Cy3-labeled ESTA-1; Blue, Hoechst 33342. **(C)** Correlation of ESTA-1 binding to the tumor vasculature and E-selectin expression in human carcinomas derived from breast, ovary, and skin.

Reproduced with permission from PLoS ONE, Mann et al, 2010, (96). Copyright Public Library of Science 2010.



C

tumor	sample N.	E-selectin (%)	ESTA-1 (%)	ESTA/E-sel ratio
breast	10	90	80	0.89
ovarian	19	71	71	1
skin	4	100	100	1

3.2.8 Effect of ESTA-1 binding on cell adhesion

Since E-selectin plays a critical role in cell adhesion, we next tested if ESTA-1-binding to E-selectin mediated inhibition of cell adhesion to endothelial cells. For this study, adhesion of a sLe^x positive human promyelocytic cell line (HL-60) on ES-Endo was analyzed. On induction of ES-Endo with doxycycline the HL-60 cell adhesion to cells increased by 5-fold (Fig. 39A). HL-60 adhesion to ES-Endo pre-incubated with indicated concentration of ESTA-1 for 20 minutes was compared with untreated cells. Preincubation of ES-Endo with ESTA-1 (100 nM) resulted in inhibition of HL-60 adhesion to induced ES-Endo by 80 % (Fig. 39A) ($p < 0.01$). The IC₅₀ for the inhibition of this interaction was approximately 63 nM. This data indicates that ESTA-1 interaction to E-selectin competes with binding of natural ligands such as sLe^x and therefore ESTA-1 can have a potential application as an antagonist of E-selectin mediated adhesion during inflammation.

3.2.9 Effect of ESTA-1 on cell viability

Lastly, for *in vivo* applications of ESTA-1, the effect of ESTA-1 treatment on the cell viability of ES-Endo cells was tested. Cells were first stimulated with doxycycline and then incubated with increasing concentration of ESTA-1 (up to 200 nM) for up to 48 hours. To test cell viability during this treatment, a MTT assay was performed. There was no reduction in cell viability at least up to 200 nM of ESTA-1 for 48 hours incubation with ESTA-1 (Fig. 39B). Also this treatment did not cause any visible morphological changes associated with cytotoxicity in the cells. Therefore, ESTA is a biocompatible material and can be

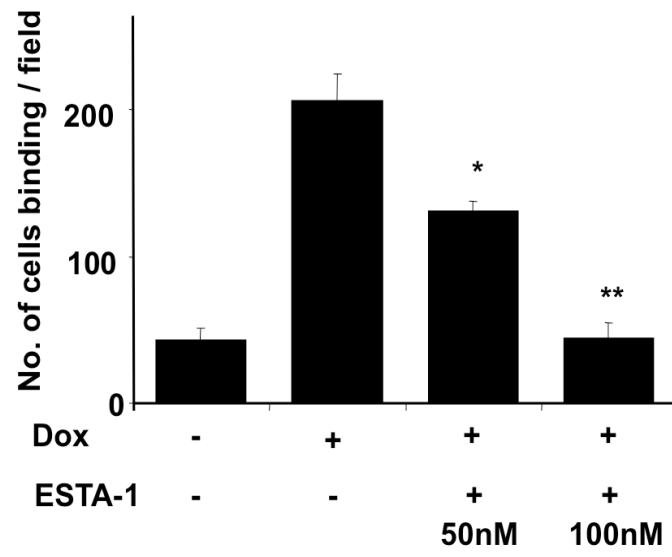
tested for its *in vivo* applications. With this data, we next developed ESTA-1 conjugated MSV to attempt targeted delivery to the bone marrow.

Figure 39. Effect of ESTA-1 binding on cell adhesion and cell viability. (A)

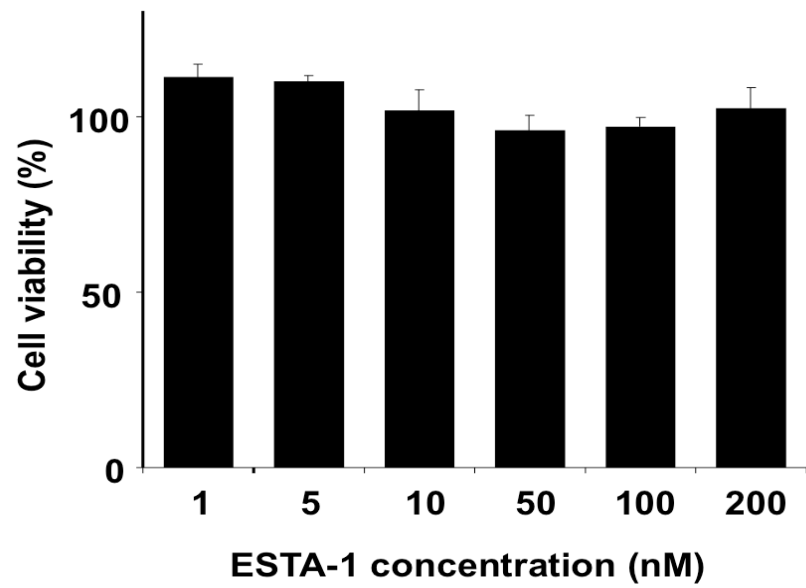
ES-Endo were incubated with doxycycline (1000 ng/ml) for 5 hours followed by different concentrations of ESTA-1 (1 - 200 nM) for 30 minutes. HL-60 cells were incubated with ES-Endo and the adhesion of HL-60 cells was quantified. Error bars, mean \pm SEM; *, $P < 0.05$, **, $P < 0.01$ vs. Dox+/ESTA-, Student's t test. **(B)** ES-Endo were incubated with doxycycline (1000 ng/ml) for 5 hours followed by different concentrations of ESTA-1 (1 - 200 nM) for 30 minutes. The cells were washed and incubated with MTT for 4 hours, and the absorbance at 570 nm was measured. The data was normalized by untreated cells (without ESTA-1) as 100%. . Error bars, mean \pm SEM.

Reproduced with permission from PLoS ONE, Mann et al, 2010, (96). Copyright Public Library of Science 2010.

A



B



3.3 Development of bone marrow targeted MSV

3.3.1 Conjugation and characterization of ESTA-MSV

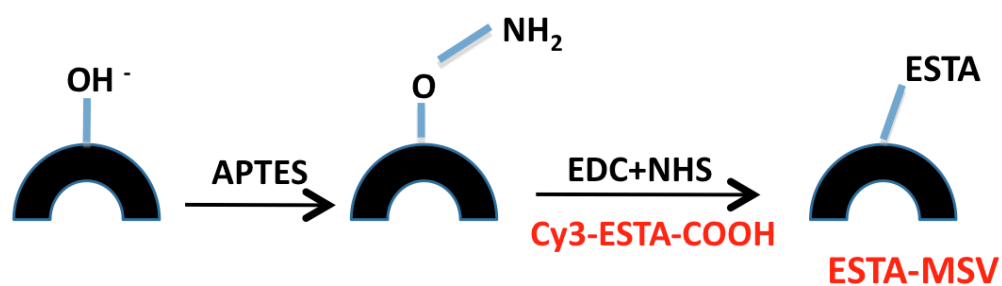
The MSVs fabricated as part of Aim 1 were functionalized by 3'-aminopropyltriethoxysilane (APTES) to introduce amine groups on the surface to serve as a linker for conjugation with E-selectin thioaptamer molecule (ESTA). ESTA containing a 5' carboxyl group was conjugated to the amino functionalized MSV as schematically represented in Fig. 40A. Initial confirmation of conjugation was done by visualizing the fluorescent ESTA-MSVs under a fluorescent microscope (Fig. 40B).

To validate the conjugation of ESTA to MSV, physico-chemical properties of ESTA-MSV were measured using three independent methods. Analysis of zeta potential showed that the surface charge of MSV changed from +6mV of amine modified MSV to -35 mV of ESTA-MSV. This change in the surface charge was attributed from the presence of DNA on the surface of MSV. To confirm the conjugation of ESTA to the MSV, the fluorescence of the Cy3-labeled ESTA conjugated MSV was examined using flow cytometry. Following the conjugation of Cy3-ESTA, the mean fluorescent intensity of MSV increased approximately 100 times (from 101 to 10561 AU) (Fig. 41A). To determine the average amount of ESTA on the MSV, Cy-3 fluorescence was measured using a fluorimeter. A linear standard curve was generated from Cy-3 ESTA fluorescence and based on Cy-3 fluorescence from ESTA-MSV, it was calculated that approximately 10^6 ESTA molecules were conjugated to each MSV (Fig. 41B). Together, these data support ESTA conjugation to MSV.

To further validate the conjugation, the infrared spectrum of ESTA-MSV was analyzed by Fourier transform infrared spectroscopy (FTIR). FTIR spectra of ESTA-MSV exhibited an appearance of two distinct peaks (1060 cm^{-1} and 1651 cm^{-1}) that corresponds to the phospho-linkage (P=O) in DNA and carboxyl (C=O) chains in the ESTA, respectively (Fig. 41C).

Figure 40. Conjugation of ESTA-1 to MSV. (A) Schematic of conjugation chemistry adopted for the conjugation of Cy3-COOH-ESTA to amine modified MSVs; **(B)** Fluorescent images of ESTA-MSV. Red – Cy-3 label on ESTA.

A



B

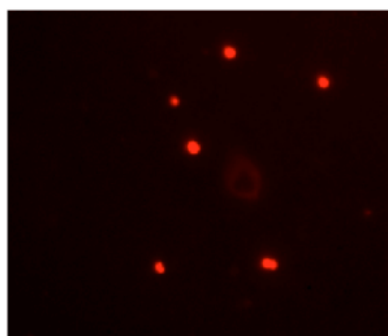
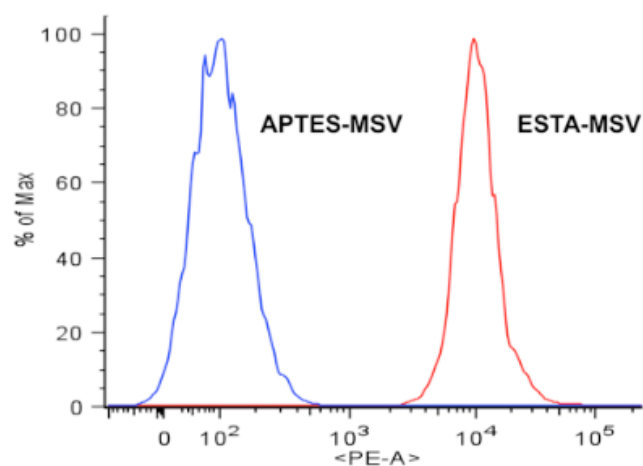
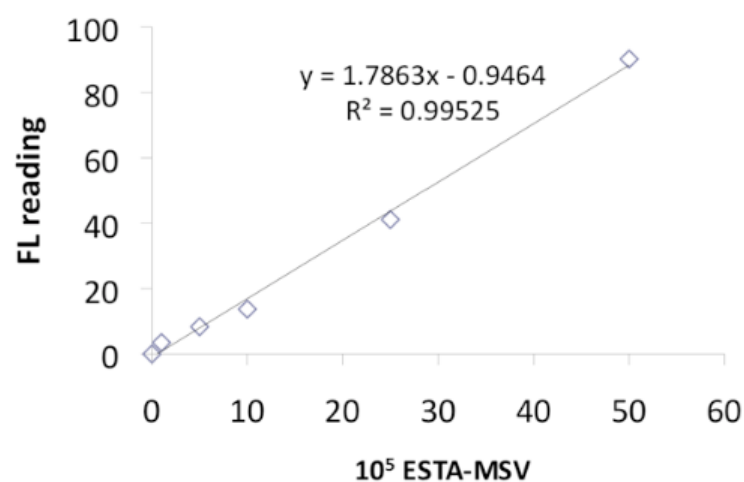


Figure 41. Physico-chemical characteristics of ESTA-MSV (A) Flow cytometry data of amine modified MSV (*blue*) and ESTA-MSV (*red*). (B) Linear standard curve of the change in fluorescence intensity corresponding to the number of ESTA-MSV. (C) FTIR spectra of MSV (*red*), ESTA (*blue*), ESTA-MSV (*green*). Arrows point to the stretching due to P=O and C=O linkages.

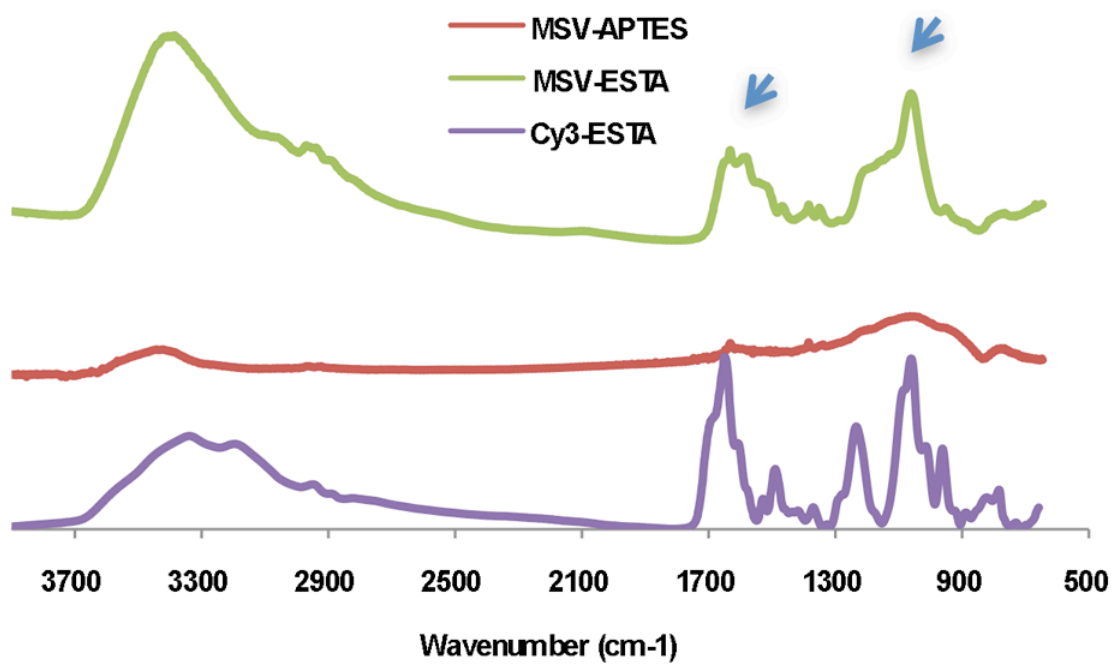
A



B



C



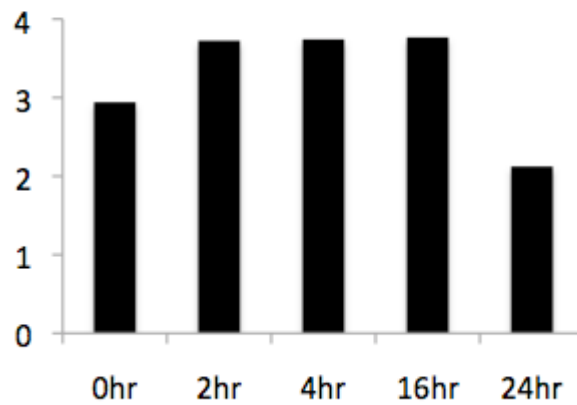
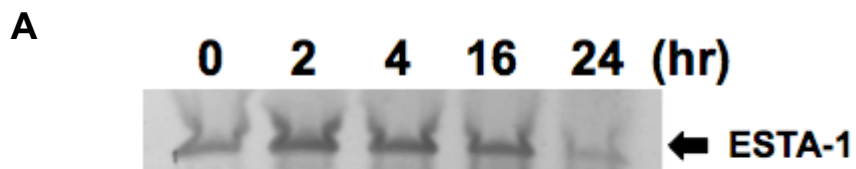
3.3.2 Serum stability of ESTA-MSV

For potential *in vivo* applications, the serum stability of ESTA-MSV was evaluated under physiological conditions. ESTA-MSV (10^6) was incubated in freshly isolated mouse serum at 37 °C up to 5 hours and three different parameters including MSV stability, ESTA-stability, and stability of ESTA conjugation on the MSV were analyzed.

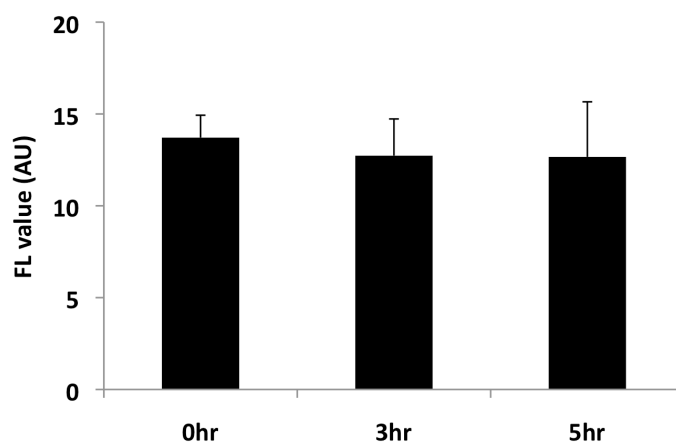
- The size distribution of ESTA-MSV remained unchanged after serum incubation as measured by dynamic light scattering, which indicated MSV stability in the serum.
- Next, stability of ESTA was assessed by serum incubation up to 24 hours at 37 °C followed by gel electrophoresis of the DNA. ESTA-1 was stable upto 16 hours in the serum, which is consistent with earlier reports that the thio-substitution enhances serum stability (Fig. 42A).
- Lastly, to confirm the serum stability of ESTA conjugation to MSV, intensity of Cy-3 fluorescence from ESTA-MSV was measured at different time points. There were no changes in the fluorescence intensity after the 5-hour incubation of MSV in the serum (Fig. 42B). The 5 hour time point was chosen based on the fact that 5 hour is the optimum time required to achieve *in vivo* targeting of the MSVs.

We also observed that serum incubation of the negatively charged ESTA-MSV caused a neutralization of the surface charge of the particles from -35mV to -15mV due to opsonization. These findings suggest that ESTA-MSV is stable for up to 5 hours under physiological conditions.

Figure 42: Stability of ESTA-MSV under physiological conditions. (A) Gel electrophoresis and densitometric analysis of ESTA-1 after serum incubation for indicated time points. **(B)** Quantification of Cy3 fluorescence from ESTA-MSV after incubation in fetal bovine serum at 37 °C for indicated time points.



B

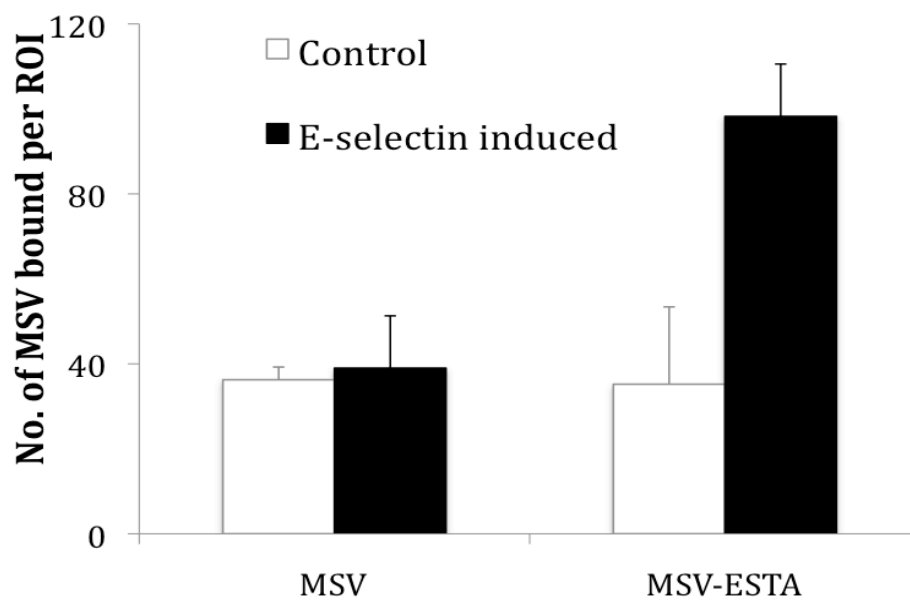


3.3.3 Adhesion of ESTA-MSV to E-selectin expressing endothelial cells

Using E-selectin inducible human microvascular endothelial cell line (ES-Endo) (95), we next examined the specific interaction of ESTA-MSV to endothelial cells expressing E-selectin on the membrane. ES-Endo showed minimal basal expression of E-selectin and the expression was induced on treatment with doxycycline (Fig. 43). To test the E-selectin specific binding of ESTA-MSV, 10^4 ESTA-MSV was incubated with ES-Endo in the presence of doxycycline at 4 °C. The number of MSV adhesion to the endothelial cell surface was three-fold more than MSV alone or to untreated cells (Fig. 43). There was no significant difference in the number of MSV and ESTA-MSV that are attached on the endothelial cell surface when E-selectin expression was not induced.

Figure 43. E-selectin dependent ESTA-MSV adhesion to endothelial cells.

ES-Endo cells were induced with doxycycline for 5 hours to induce E-selectin expression. The cells were then incubated with ESTA-MSV for 1 hour at 4° C and then washed and fixed in paraformaldehyde. The number of MSV was counted in five different fields of view using a microscope and plotted per region of interest (ROI). Error bars mean \pm SEM.

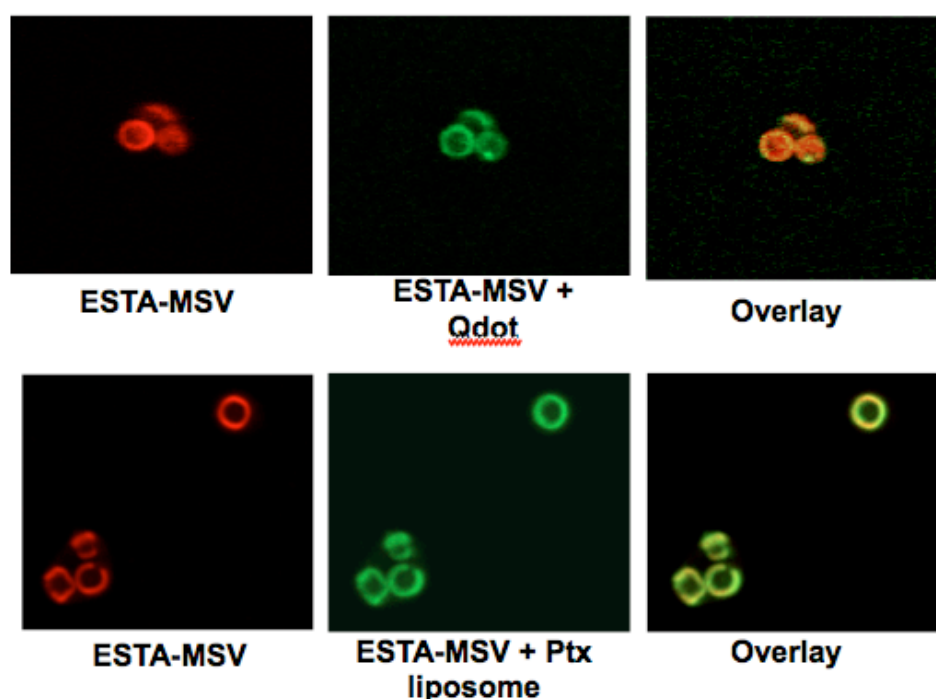


3.3.4 Development of ESTA-MSV loaded with nanoparticles

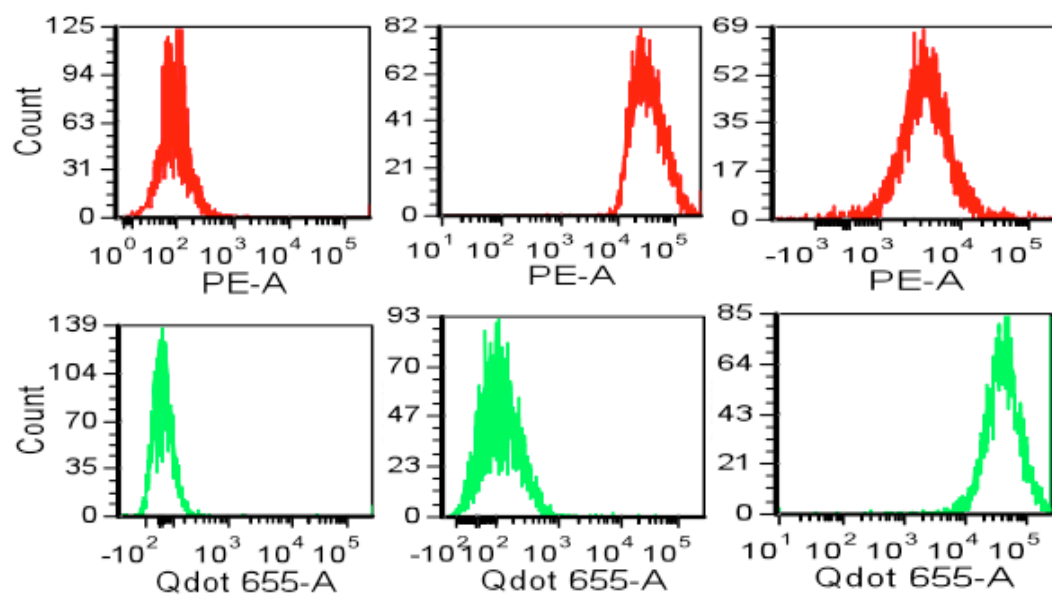
Next, the ability of nanoparticle loading to the ESTA-MSV was tested using three different types of nanoparticles. First, loading of amino (PEG) quantum dots-655 of (mean diameter = 20 nm) showed a similar overlay pattern of green (Qdot) and red fluorescence (Cy-3 ESTA) (Fig. 44A top panel). Similarly, cationic DOPC liposomes containing Oregon green paclitaxel (size ranging from 25-35 nm) were loaded into the ESTA-MSV (96). The loading of liposomes was visualized by confocal microscopy by analyzing the overlay of green (liposomes) and red fluorescence (Cy-3 ESTA)(Fig. 44A bottom panel). The fluorescence measurements by flow cytometer verified a significant increase (approximately 100 fold) in red fluorescence after ESTA conjugation to MSV (ESTA-MSV) and green fluorescence after loading of with Q-dot 655 into ESTA-MSV (Fig. 44B). Lastly, the loading of amine functionalized iron oxide nanoparticles (diameter =15 nm) was also confirmed by Prussian blue staining (Fig. 44C), and the iron content was quantified to 5 μg of Fe in 10^7 ESTA-MSV. These experiments demonstrated the ability of loading nanoparticles, which could either be a drug carrier (such as liposomes) or an imaging agent (Q-dot or FeO NPs), into the mesoporous structure of ESTA-MSV.

Figure 44. Nanoparticle loading into ESTA-MSV. (A) Qdot 655 were loaded into ESTA-MSV (top panel) *Red*, Cy-3 ESTA-MSV; *Green*, Qdot. Ptx encapsulating DOPC liposomes were loaded into ESTA-MSV (bottom panel) *Red*, Cy-3 ESTA-MSV; *Green*, Oregon green Ptx encapsulated liposomes. **(B)** Flow cytometry was carried out to analyze the fluorescence from the surface of MSV. Red fluorescence measured for ESTA-MSV after conjugation (top panel); green fluorescence measured for ESTA-MSV before and after loading with Qdot (bottom panel). **(C)** Iron oxide nanoparticles were loaded into ESTA-MSV and amount of iron loaded was measured using Prussian blue analysis. Error bars mean \pm SEM.

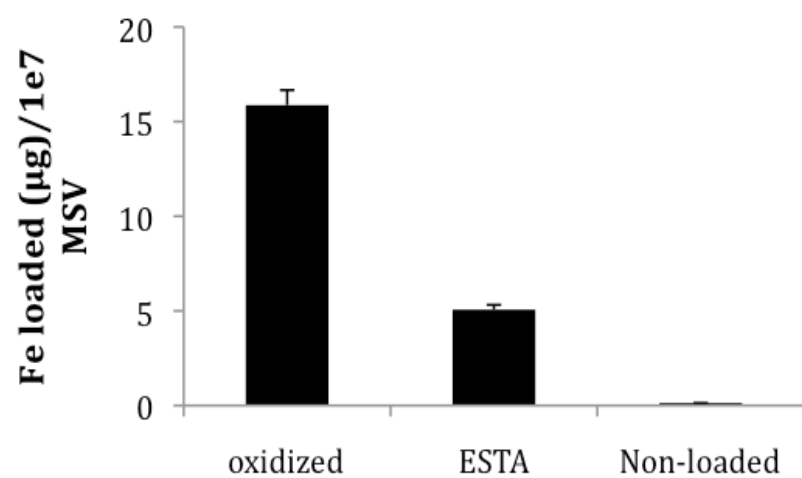
A



B



C



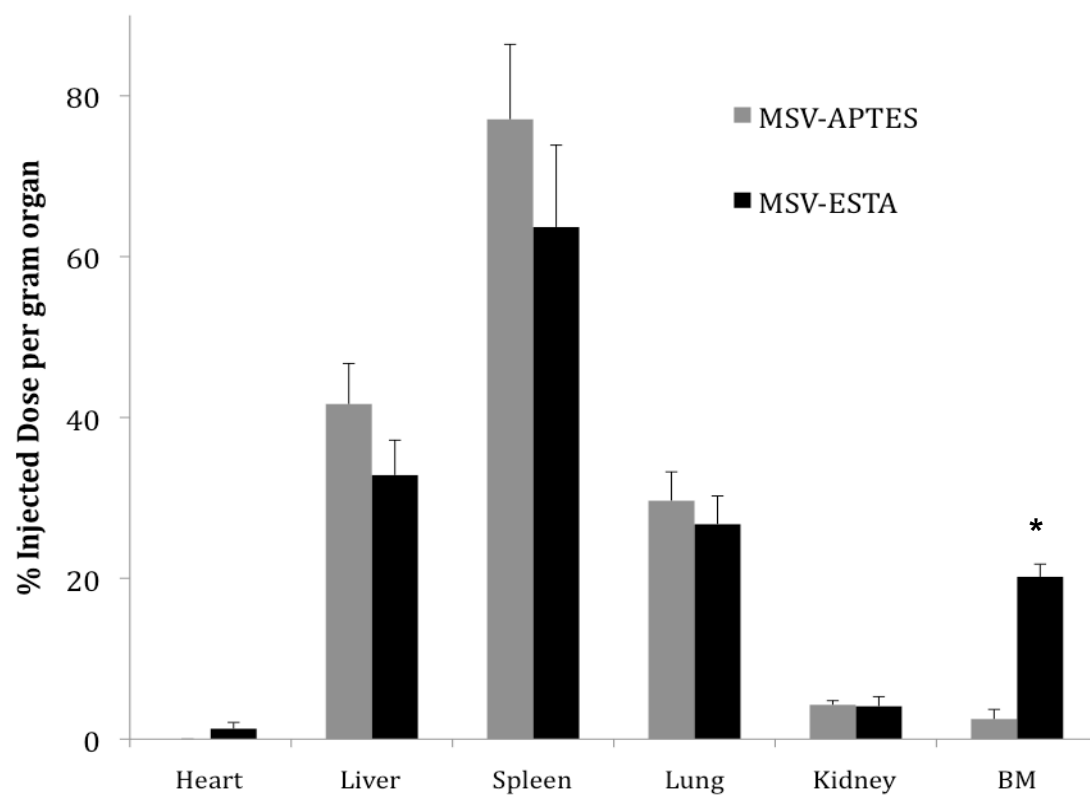
3.3.5 BM targeting of ESTA-MSV

For bio-distribution studies of ESTA-MSV, the mice were intravenously injected with 5×10^7 ESTA-MSV and all major organs including liver, spleen, heart, lung, bone marrow were harvested after 5 hours and the silicon content was analyzed using ICP-OES. The accumulation of ESTA-MSV in the bone marrow was 8 times higher as compared to un-conjugated MSV. The accumulation of ESTA-MSV in the bone corresponded to over 20 % of injected dose/g organ weight ($P < 0.04$) (Fig. 45A). The non-targeted MSV exhibited minimum accumulation in the BM and primarily accumulated in the liver and spleen. Histological analysis also supported the presence of ESTA-MSV in the endothelial wall of the BM tissue (Fig. 45B).

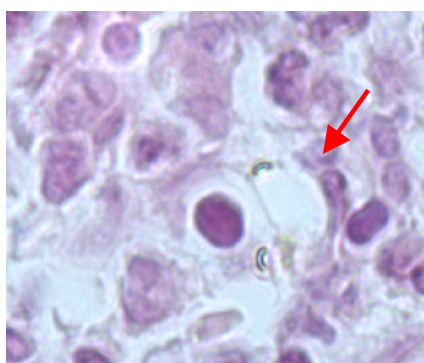
Lastly, the delivery of MSV loaded with nanoliposomes containing Oregon green paclitaxel to the bone marrow was analyzed. Following intravenously injection, the fresh bone marrow was isolated and analyzed by fluorescent microscope. A significant accumulation of green fluorescence was observed in the BM when the liposome loaded ESTA-MSV was injected intravenously. In contrast, injection of non-targeted MSV loaded with equivalent amount of liposomes or with naked liposomal only showed minimal accumulation of green fluorescence in the BM (Fig. 45C).

Figure 45. *In vivo* distribution of ESTA-MSV in mice. ESTA-MSV was injected to mice via tail vein and were harvested 5 hours after the injection and analyzed for silicon content. **(A)** Biodistribution of ESTA-MSV represented as percentage of injected silicon per gram weight of organ. Error bars mean \pm SEM. *P<0.04. **(B)** Paraffin sections of bone were prepared to visualize the localization of ESTA-MSV in the bone marrow. **(C)** ESTA- MSV containing paclitaxel liposomes were injected in mice and bone marrow tissue was isolated and stained with DAPI to assess distribution of liposomes. *Green*, Oregon green encapsulated liposome; *blue*, Hoechst 33342.

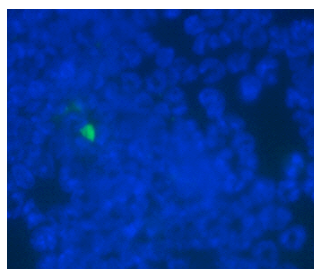
A



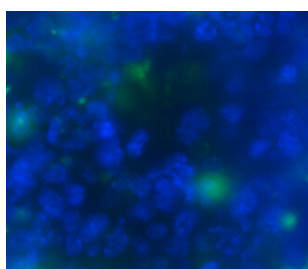
B



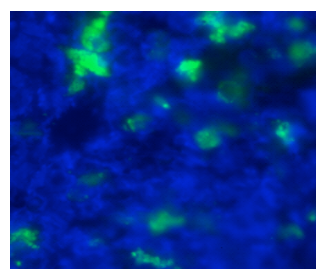
C



MSV-Liposome



Liposome alone



ESTA-MSV-Liposome

Chapter 4. Discussion

Bone marrow is a highly heterogeneous organ performing a critical function of hematopoiesis and comprising of a wide variety of cell types. Multiple diseases that originate or involve this organ are associated with a specific cell type in the BM. Due to this complexity of BM composition and the presence of healthy hematopoietic progenitor cells, conventional forms of treatment options are not efficient. Therefore, non-conventional forms of drug delivery are urgently needed to efficiently deliver therapeutics to the diseased cell type in the bone marrow

To achieve this goal we proposed a strategy to actively target therapeutics through targeting of a drug carrier to the bone marrow. For successfully targeting a drug carrier to a specific site in the body we first identified three prerequisites.

1. A unique biological target specific to site of delivery
2. A high-affinity ligand against the target molecule
3. An optimally designed drug delivery carrier

In our study we focused on active vascular targeting to achieve an efficient method of drug delivery. E-selectin a cell adhesion molecule on endothelial cells was selected as the biological target for active targeting due to its constitutive expression on BM endothelium and that E-selectin expressed on the luminal surface of vascular endothelium is readily accessible to systemically injected drug carriers.

For targeting E-selectin, although various ligands have been developed and used for active targeting of nanoparticles to E-selectin expressing cells [4,5], the usage of these ligands remains a challenge due to low affinity and lack of serum stability. For example, E-selectin peptide is an L-amino acid peptide that suffers from bioavailability and stability issues for clinical applications [6]. In fact, we conducted targeting experiments with MSVs conjugated with high affinity E-selectin peptide and observed that the serum stability of the peptide compromised the in vivo targeting efficacy. For other ligands such as antibodies, difficulty in controlling the orientation during chemical conjugation posed a limitation for targeted delivery. Lastly, due to the structural homology between different members of the selectin cell adhesion family, isolation of E-selectin specific selectin ligands has remained elusive. In fact, most of the carbohydrate mimetic ligands identified for E-selectin exhibit considerable cross reactivity against other selectins (L- and P- selectin) [7], limiting their use of such for targeted delivery due to possible off targeting effects. These limitations prompted me to identify a novel thioaptamer ligand against E-selectin.

Aptamer screening typically consists of binding reactions of combinatorial libraries with recombinant protein (25-28). However, mammalian proteins undergo structural differences associated with post-translational modifications, which cannot be completely mimicked by recombinant proteins. Therefore, screening with protein alone can lead to identification of aptamers that would not maintain their binding capabilities to the target protein in a physiological environment such as in the cells. Hence, the integration of biologically relevant conditions during the aptamer screening process is crucial for identifying aptamers that maintain binding under physiologically conditions. Therefore, for

the identification of E-selectin specific thioaptamer, we utilized a two-step selection strategy. The first screening step involved screening the combinatorial library using human E-selectin recombinant protein. Ten iterative cycles of binding and enrichment of thioaptamers bound to E-selectin protein led to the identification of 14 TA sequences (Fig. 24). The second step was the cell-based selection of these 14 candidates using an E-selectin inducible endothelial cells. Commonly used approaches including induction by cytokines such as TNF- α , IL-1 β were not employed in this step as they result in induction of a wide variety of surface molecules and it would be difficult to rule out the involvement of these other cell surface molecules during the E-selectin specific screening of thioaptamers. Therefore, we developed a doxycycline inducible E-selectin expression endothelial cell line for a controllable and highly selective induction of E-selectin expression. In the cell-based selection, only one of the 14 selected TA's exhibited highly doxycycline-dependent binding to endothelial cell expressing E-selectin (Table 2). This was surprising because the initial TA screening was conducted using human recombinant E-selectin protein isolated from the mammalian system. This points out the fact that the first step of screening of TA's from the combinatorial library yielded ligands of relatively high affinity, but low specificity (less doxycycline-dependent binding) to the E-selectin expressing cells.

Most mammalian proteins undergo structural changes associated with post-translational modifications, which cannot be completely mimicked by recombinant proteins. Therefore, *in vitro* ligand selection with pure biochemical entities (e.g., recombinant protein) may not mimic effective ligand binding in a

complex biological environment, particularly if the target protein is significantly post-translationally modified such as in the case of E-selectin. E-selectin protein undergoes sequential post-translational modification and is matured from 51 kDa to 115 kDa. Thus, the integration of 2nd step of biological selection in the screening process is essential for the identification of highly specific and high affinity ligands. Overall, the two-step screening strategy allowed us to identify a novel E-selectin thioaptamer (ESTA-1) that specifically binds to E-selectin expressing on the endothelial cell surface (Fig. 31). Our data demonstrated that mono-thiophosphate substitution in ESTA-1 resulted in high affinity binding to E-selectin (47 nM) (Fig. 35). This is a significant improvement of 2,000-40,000 times higher affinity as compared to the natural ligand sLe^x (K_D = 100–2000 mM) (13). Also the sulfur substitution of the phosphate oxygens on the DNA backbone in ESTA offers enhanced serum stability. Moreover, dithio-substituted DNA has been shown to increase the binding affinity of non-thioated or monothio analogue by 100–600 times [30]. This suggests that dithio-substitution of ESTA-1 can lead to further development of higher affinity of ligands against E-selectin. Additionally, we demonstrated that the ESTA-1 binds E-selectin with negligible cross reactivity to L- and P-selectin (μ M). Minimal cross reactivity of ESTA-1 further highlights the potential utility of ESTA-1 for highly selective E-selectin targeted therapeutic and imaging applications. Lastly, we tested ESTA-1 binding to E-selectin expressing vessels in both human carcinoma pathology samples and animal models to ensure that ESTA-1 bound E-selectin independent of species differences. We believe that sequence and structural homology between human and mouse E-selectin [8] resulted in species independent binding of ESTA-1 to E-selectin. In addition, ESTA-1 is stable under physiological

conditions for up to 16 hours (Fig. 42). This fact makes ESTA-1 extremely useful for pre-clinical validation and for possible clinical applications. Furthermore, ESTA-1 effectively inhibited the E-selectin dependent adhesion of leukocytes on endothelial cells (Fig. 39). Therefore, ESTA-1 can also be utilized as an antagonist to block the E-selectin dependent leukocyte recruitment cascade during chronic inflammation.

One of the foremost applications of ESTA-1 is for targeted delivery of drug carriers to E-selectin as described in this study. We utilized the multistage drug delivery strategy, which has been developed by our group. This strategy is based on circumnavigating biological barriers present in the body by incorporating multiple stages thereby maximizing site-specific localization and release of therapeutics therein. The first stage comprises of porous silicon microparticles as drug carriers and involves encapsulating drug-containing nanoparticles within MSVs that protect and ferry these nanoparticles until they recognize and dock at their target site on the vasculature. Using an integrated approach combining *in silico* mathematical modeling with *in vitro* and *in vivo* experiments, MSVs were rationally designed with a hemispherical geometry to maximize localization and adhesion to vasculature, whilst minimizing RES uptake [9]. Porous silicon was chosen because it is highly biodegradable into harmless silicic acid byproducts under physiological conditions, presenting fewer challenges for long-term use and has received FDA approval. The degradation kinetics of MSVs is dependent on the pore characteristics, which can be tailored during their fabrication. Since the release of nanoparticle payload is dependent on the degradation of MSV, the release can be tightly regulated. One of the applications of MSV can be to function as intravascular depots, whereby MSVs

are fabricated to undergo slow degradation leading to a sustained release of therapeutic payload. This property was successfully demonstrated for the sustained delivery of siRNA-encapsulated liposomes incorporated into the MSV to achieve sustained gene silencing in ovarian tumors. The silencing of EphA2 gene in ovarian tumor by a single intravenous injection of MSV loaded with EphA2 siRNA liposomes lasted three weeks, which was comparable to six repeated injections of siRNA liposomes alone (Fig. 20). In addition, our data indicated that MSV-loaded liposomal siRNA reduced the induction of inflammatory cytokines as associated with liposomes alone (Fig. 22). This silencing led to significant tumor shrinkage and therapeutic efficacy in animals bearing ovarian xenografts (96).

The fact that BM exhibits unique vascular characteristics, for instance the average hydrodynamic shear rate in the BM microvessels being lower than in other organs [10], higher margination and subsequent adhesion to the vessel wall is expected. This vessel binding can be further enhanced by the presence of high affinity targeting ligands [11]. Porous silicon offers ease of surface modifications for chemical conjugation of targeting ligands. ESTA-1 was conjugated to MSV and confirmed by multiple techniques. ESTA-MSV showed higher adhesion to E-selectin positive endothelial cells *in vitro* and *in vivo*. ESTA-MSV showed enhanced localization in the BM tissue (20 % injected dose/g organ) and significantly enhanced delivery of therapeutic liposomes incorporate in the porous structure of MSVs (Fig. 45). Comparing these results with an earlier study by Tari et al, we estimated that 200 times more liposomes could be delivered to the BM tissue carried by the ESTA-MSV as compared to an injection of equivalent amount of liposome alone [12]. The targeting experiments in this

study have been conducted in disease free animals, and as mentioned earlier certain pathological and physiological stimuli can cause changes in the vascular characteristics of BM. Therefore it still remains to be evaluated how such changes would affect the MSV targeting to the BM vasculature.

One of the unique advantages of MSV is the flexible choice of payload such as lipid-based carriers, metal nanoparticles or drug alone that can be loaded into the porous MSVs. As a proof of concept, we demonstrated three types of nanoparticles loaded into the porous structure of ESTA-MSV (Fig. 44). Based on our calculations, 7×10^4 iron oxide nanoparticles (with a 15 nm diameter) were incorporated into the pores of a single ESTA-MSV (1.6 μm diameter, 60 % porosity). As described by a recent study from our group, the geometrical confinement of iron oxide nanoparticles in the MSV can lead to enhancement of contrast for imaging applications (104). Therefore, delivery of MSV loaded with such iron oxide nanoparticles can have imaging applications.

The advantage afforded by this multistage approach for drug delivery are easily appreciable, and lie in its multi-functionality and its ability to favorably alter the pharmacokinetics of drugs. A combination of two biocompatible materials (MSV and ESTA), may allow for wide ranging applications such as described below:

1. Treatment of pathological conditions associated with bone marrow [11].
2. For non-invasive methods of diagnostic imaging for the evaluation of multiple clinical problems for

- determining the amount of active marrow after X-irradiation and chemotherapy

- diagnosis and detection of metastases

- location of the sites for marrow biopsy

3. Delivery of agents for the suppression of the inherent function of the bone marrow. This can be particularly effective in preventing rejection following organ transplantation. Currently used immunosuppressant such as Cyclosporin A is associated with significant side effects, particularly nephrotoxicity, when used for prolonged periods [12].

4. Majority of conventional chemotherapeutic drugs have limitations to the dose administered due to their toxicity to the bone marrow. Several hematopoietic growth factors such as CSF-1 and GM-CSF, can mediate self-renewal, proliferation, maturation and activation of marrow cells [13]. This class of agents can be delivered to the bone marrow for protection of bone marrow and stimulation of its hematopoietic function in conjunction with the chemotherapy.

4.1 Future work and directions

In this study, we provide first evidence of organ specific active targeting for delivery of nanoparticles to the BM tissue via E-selectin. This multistage system can further be improved by loading nanoparticles that can target specific cell type in the bone marrow space. This can be achieved by conjugating the nanoparticle with ligands specific to a cell type of interest. Such a two-step active targeting concept comprising of organ targeting followed by cell targeting can further improve the efficacy and potentially minimize the effect of drugs on healthy hematopoietic cells. One example can be the case of breast cancer bone metastases where cancer cells metastasizing to the bone marrow cause hypercalcemia and their self-stimulation via a “vicious cycle” through maturation of osteoclast via activation of cell membrane-associated proteins termed receptor activator of NF- κ B ligand (RANK/RANKL axis). The mature osteoclasts mediate osteolysis (bone resorption) and also secrete growth factors such as TGF- β that stimulate tumor growth, leading to pathological hypercalcemia. This study can be applied to achieve inhibition of this osteoclastogenic vicious cycle by the delivery of therapeutic agents specifically at the metastatic sites in the bone marrow without affecting the normal hematopoietic precursor cells. Utilizing the two-step sequential targeting; first the MSV targets to the bone marrow metastatic niche via E-selectin, then RANK peptide conjugated nanoparticles released from MSV in the bone marrow will target osteoclasts. This can potentially lead to enhanced local delivery of therapeutics to the osteoclast in the bone marrow metastatic niche and reduce bone resorption without affecting healthy hematopoietic precursor cells.

References

1. Travlos, G. S. 2006. Normal structure, function, and histology of the bone marrow. *Toxicol Pathol* 34:548-565.
2. Cumming, J. D. 1962. A study of blood flow through bone marrow by a method of venous effluent collection. *J Physiol* 162:13-20.
3. Michelsen, K. 1969. Hemodynamics in the bone marrow of anemic rabbits with increased hematopoiesis. *Acta Physiol Scand* 77:52-57.
4. Mazo, I. B., and U. H. von Andrian. 1999. Adhesion and homing of blood-borne cells in bone marrow microvessels. *J Leukoc Biol* 66:25-32.
5. Farhi, D. C., U. G. Mason, 3rd, and C. R. Horsburgh, Jr. 1985. The bone marrow in disseminated *Mycobacterium avium*-intracellulare infection. *Am J Clin Pathol* 83:463-468.
6. Mundy, G. R. 2002. Metastasis to bone: causes, consequences and therapeutic opportunities. *Nat Rev Cancer* 2:584-593.
7. Savona, M., and M. Talpaz. 2008. Getting to the stem of chronic myeloid leukaemia. *Nat Rev Cancer* 8:341-350.
8. Barrett, O. N. 1986. Bone Marrow Disorders: The Biological Basis of Clinical Problems. *JAMA: The Journal of the American Medical Association* 256:533.
9. Palumbo, A., and K. Anderson. 2011. Multiple myeloma. *N Engl J Med* 364:1046-1060.

10. Maxwell, M. B., and K. E. Maher. 1992. Chemotherapy-induced myelosuppression. *Semin Oncol Nurs* 8:113-123.
11. Porter, C. J., S. M. Moghimi, L. Illum, and S. S. Davis. 1992. The polyoxyethylene/polyoxypropylene block co-polymer poloxamer-407 selectively redirects intravenously injected microspheres to sinusoidal endothelial cells of rabbit bone marrow. *FEBS Lett* 305:62-66.
12. Stopeck, A. T., A. Lipton, J. J. Body, G. G. Steger, K. Tonkin, R. H. de Boer, M. Lichinitser, Y. Fujiwara, D. A. Yardley, M. Viniegra, M. Fan, Q. Jiang, R. Dansey, S. Jun, and A. Braun. 2010. Denosumab compared with zoledronic acid for the treatment of bone metastases in patients with advanced breast cancer: a randomized, double-blind study. *J Clin Oncol* 28:5132-5139.
13. Rachner, T. D., S. Khosla, and L. C. Hofbauer. 2011. Osteoporosis: now and the future. *Lancet* 377:1276-1287.
14. Rizzoli, R., U. Yasothan, and P. Kirkpatrick. 2010. Denosumab. *Nat Rev Drug Discov* 9:591-592.
15. Theis, T., D. Parr, P. Binks, J. Ying, K. E. Drexler, E. Schepers, K. Mullis, C. Bai, J. J. Boland, R. Langer, P. Dobson, C. N. Rao, and M. Ferrari. 2006. nanotechnology. *Nat Nanotechnol* 1:8-10.
16. McNeil, S. E. 2005. Nanotechnology for the biologist. *J Leukoc Biol* 78:585-594.

17. Ferrari, M. 2005. Cancer nanotechnology: opportunities and challenges. *Nat Rev Cancer* 5:161-171.
18. Godin, B., J. H. Sakamoto, R. E. Serda, A. Grattoni, A. Bouamrani, and M. Ferrari. 2010. Emerging applications of nanomedicine for the diagnosis and treatment of cardiovascular diseases. *Trends Pharmacol Sci* 31:199-205.
19. Wan, A. C., and J. Y. Ying. 2010. Nanomaterials for in situ cell delivery and tissue regeneration. *Adv Drug Deliv Rev* 62:731-740.
20. Kim, B. Y., J. T. Rutka, and W. C. Chan. 2010. Nanomedicine. *N Engl J Med* 363:2434-2443.
21. Sakamoto, J. H., A. L. van de Ven, B. Godin, E. Blanco, R. E. Serda, A. Grattoni, A. Ziemys, A. Bouamrani, T. Hu, S. I. Ranganathan, E. De Rosa, J. O. Martinez, C. A. Smid, R. M. Buchanan, S. Y. Lee, S. Srinivasan, M. Landry, A. Meyn, E. Tasciotti, X. Liu, P. Decuzzi, and M. Ferrari. 2010. Enabling individualized therapy through nanotechnology. *Pharmacol Res* 62:57-89.
22. Sakamoto, J., A. Annapragada, P. Decuzzi, and M. Ferrari. 2007. Antibiological barrier nanovector technology for cancer applications. *Expert Opin Drug Deliv* 4:359-369.
23. Northfelt, D. W., F. J. Martin, P. Working, P. A. Volberding, J. Russell, M. Newman, M. A. Amantea, and L. D. Kaplan. 1996. Doxorubicin encapsulated in liposomes containing surface-bound polyethylene glycol:

- pharmacokinetics, tumor localization, and safety in patients with AIDS-related Kaposi's sarcoma. *J Clin Pharmacol* 36:55-63.
24. Blanco, E., A. Hsiao, A. P. Mann, M. G. Landry, F. Meric-Bernstam, and M. Ferrari. 2011. Nanomedicine in Cancer Therapy: Innovative Trends and Prospects. *Cancer Sci*.
 25. Farokhzad, O. C., and R. Langer. 2009. Impact of nanotechnology on drug delivery. *ACS Nano* 3:16-20.
 26. Hobbs, S. K., W. L. Monsky, F. Yuan, W. G. Roberts, L. Griffith, V. P. Torchilin, and R. K. Jain. 1998. Regulation of transport pathways in tumor vessels: role of tumor type and microenvironment. *Proceedings of the National Academy of Sciences of the United States of America* 95:4607-4612.
 27. Neri, D., and R. Bicknell. 2005. Tumour vascular targeting. *Nat Rev Cancer* 5:436-446.
 28. Welply, J. K., J. L. Keene, J. J. Schmuke, and S. C. Howard. 1994. Selectins as potential targets of therapeutic intervention in inflammatory diseases. *Biochim Biophys Acta* 1197:215-226.
 29. Kobayashi, H., K. C. Boelte, and P. C. Lin. 2007. Endothelial cell adhesion molecules and cancer progression. *Curr Med Chem* 14:377-386.
 30. Kumar, C. C., L. Armstrong, Z. Yin, M. Malkowski, E. Maxwell, H. Ling, B. Yaremko, M. Liu, J. Varner, E. M. Smith, B. Neustadt, and T. Nechuta.

2000. Targeting integrins alpha v beta 3 and alpha v beta 5 for blocking tumor-induced angiogenesis. *Advances in experimental medicine and biology* 476:169-180.
31. Kumar, C. C. 2003. Integrin alpha v beta 3 as a therapeutic target for blocking tumor-induced angiogenesis. *Current drug targets* 4:123-131.
 32. Pfaff, M., K. Tangemann, B. Muller, M. Gurrath, G. Muller, H. Kessler, R. Timpl, and J. Engel. 1994. Selective recognition of cyclic RGD peptides of NMR defined conformation by alpha IIb beta 3, alpha V beta 3, and alpha 5 beta 1 integrins. *The Journal of biological chemistry* 269:20233-20238.
 33. Witte, L., D. J. Hicklin, Z. Zhu, B. Pytowski, H. Kotanides, P. Rockwell, and P. Bohlen. 1998. Monoclonal antibodies targeting the VEGF receptor-2 (Flk1/KDR) as an anti-angiogenic therapeutic strategy. *Cancer metastasis reviews* 17:155-161.
 34. Siegel, G., and M. Malmsten. 1997. The role of the endothelium in inflammation and tumor metastasis. *Int J Microcirc Clin Exp* 17:257-272.
 35. Burdick, M. M., O. J. McCarty, S. Jadhav, and K. Konstantopoulos. 2001. Cell-cell interactions in inflammation and cancer metastasis. *IEEE Eng Med Biol Mag* 20:86-91.
 36. Tasciotti, E., X. Liu, R. Bhavane, K. Plant, A. D. Leonard, B. K. Price, M. M. Cheng, P. Decuzzi, J. M. Tour, F. Robertson, and M. Ferrari. 2008. Mesoporous silicon particles as a multistage delivery system for imaging and therapeutic applications. *Nat Nanotechnol* 3:151-157.

37. Chiappini, C., E. Tasciotti, J. R. Fakhoury, D. Fine, L. Pullan, Y. C. Wang, L. Fu, X. Liu, and M. Ferrari. 2010. Tailored porous silicon microparticles: fabrication and properties. *Chemphyschem* 11:1029-1035.
38. Martin, F. J., K. Melnik, T. West, J. Shapiro, M. Cohen, A. A. Boiarski, and M. Ferrari. 2005. Acute toxicity of intravenously administered microfabricated silicon dioxide drug delivery particles in mice: preliminary findings. *Drugs R D* 6:71-81.
39. Decuzzi, P., R. Pasqualini, W. Arap, and M. Ferrari. 2009. Intravascular delivery of particulate systems: does geometry really matter? *Pharm Res* 26:235-243.
40. Decuzzi, P., and M. Ferrari. 2007. The role of specific and non-specific interactions in receptor-mediated endocytosis of nanoparticles. *Biomaterials* 28:2915-2922.
41. Decuzzi, P., and M. Ferrari. 2006. The adhesive strength of non-spherical particles mediated by specific interactions. *Biomaterials* 27:5307-5314.
42. Decuzzi, P., and M. Ferrari. 2008. The receptor-mediated endocytosis of nonspherical particles. *Biophysical journal* 94:3790-3797.
43. Ferrari, M. 2008. The mathematical engines of nanomedicine. *Small* 4:20-25.
44. Godin, B., J. Gu, R. E. Serda, R. Bhavane, E. Tasciotti, C. Chiappini, X. Liu, T. Tanaka, P. Decuzzi, and M. Ferrari. 2010. Tailoring the

- degradation kinetics of mesoporous silicon structures through PEGylation. *J Biomed Mater Res A* 94:1236-1243.
45. Park, J. H., L. Gu, G. von Maltzahn, E. Ruoslahti, S. N. Bhatia, and M. J. Sailor. 2009. Biodegradable luminescent porous silicon nanoparticles for in vivo applications. *Nature materials* 8:331-336.
 46. Anglin, E. J., L. Cheng, W. R. Freeman, and M. J. Sailor. 2008. Porous silicon in drug delivery devices and materials. *Advanced drug delivery reviews* 60:1266-1277.
 47. Foraker, A. B., R. J. Walczak, M. H. Cohen, T. A. Boiarski, C. F. Grove, and P. W. Swaan. 2003. Microfabricated porous silicon particles enhance paracellular delivery of insulin across intestinal Caco-2 cell monolayers. *Pharmaceutical research* 20:110-116.
 48. Delouise, L. A., and B. L. Miller. 2005. Enzyme immobilization in porous silicon: quantitative analysis of the kinetic parameters for glutathione-S-transferases. *Analytical chemistry* 77:1950-1956.
 49. Salonen, J., A. M. Kaukonen, J. Hirvonen, and V. P. Lehto. 2008. Mesoporous silicon in drug delivery applications. *Journal of pharmaceutical sciences* 97:632-653.
 50. Tasciotti, E., X. W. Liu, R. Bhavane, K. Plant, A. D. Leonard, B. K. Price, M. M. C. Cheng, P. Decuzzi, J. M. Tour, F. Robertson, and M. Ferrari. 2008. Mesoporous silicon particles as a multistage delivery system for imaging and therapeutic applications. *Nature Nanotechnology* 3:151-157.

51. Tanaka, T., B. Godin, R. Bhavane, R. Nieves-Alicea, J. Gu, X. Liu, C. Chiappini, J. R. Fakhoury, S. Amra, A. Ewing, Q. Li, I. J. Fidler, and M. Ferrari. 2010. In vivo evaluation of safety of nanoporous silicon carriers following single and multiple dose intravenous administrations in mice. *Int J Pharm* 402:190-197.
52. Springer, T. A. 1994. Traffic signals for lymphocyte recirculation and leukocyte emigration: the multistep paradigm. *Cell* 76:301-314.
53. Subramaniam, M., J. A. Koedam, and D. D. Wagner. 1993. Divergent fates of P- and E-selectins after their expression on the plasma membrane. *Mol Biol Cell* 4:791-801.
54. Shimizu, Y., S. Shaw, N. Graber, T. V. Gopal, K. J. Horgan, G. A. Van Seventer, and W. Newman. 1991. Activation-independent binding of human memory T cells to adhesion molecule ELAM-1. *Nature* 349:799-802.
55. Picker, L. J., T. K. Kishimoto, C. W. Smith, R. A. Warnock, and E. C. Butcher. 1991. ELAM-1 is an adhesion molecule for skin-homing T cells. *Nature* 349:796-799.
56. Kalluri, R., and M. Zeisberg. 2006. Fibroblasts in cancer. *Nat Rev Cancer* 6:392-401.
57. Matsumoto, S., Y. Imaeda, S. Umemoto, K. Kobayashi, H. Suzuki, and T. Okamoto. 2002. Cimetidine increases survival of colorectal cancer

patients with high levels of sialyl Lewis-X and sialyl Lewis-A epitope expression on tumour cells. *Br J Cancer* 86:161-167.

58. Gout, S., P. L. Tremblay, and J. Huot. 2008. Selectins and selectin ligands in extravasation of cancer cells and organ selectivity of metastasis. *Clin Exp Metastasis* 25:335-344.
59. Tremblay, P. L., J. Huot, and F. A. Auger. 2008. Mechanisms by which E-selectin regulates diapedesis of colon cancer cells under flow conditions. *Cancer Res* 68:5167-5176.
60. Zen, K., D. Q. Liu, Y. L. Guo, C. Wang, J. Shan, M. Fang, C. Y. Zhang, and Y. Liu. 2008. CD44v4 is a major E-selectin ligand that mediates breast cancer cell transendothelial migration. *PLoS One* 3:e1826.
61. Hendrix, M. J., E. A. Seftor, A. R. Hess, and R. E. Seftor. 2003. Vasculogenic mimicry and tumour-cell plasticity: lessons from melanoma. *Nat Rev Cancer* 3:411-421.
62. Tremblay, P. L., F. A. Auger, and J. Huot. 2006. Regulation of transendothelial migration of colon cancer cells by E-selectin-mediated activation of p38 and ERK MAP kinases. *Oncogene* 25:6563-6573.
63. Schweitzer, K. M., A. M. Drager, P. van der Valk, S. F. Thijsen, A. Zevenbergen, A. P. Theijssmeijer, C. E. van der Schoot, and M. M. Langenhuijsen. 1996. Constitutive expression of E-selectin and vascular cell adhesion molecule-1 on endothelial cells of hematopoietic tissues. *Am J Pathol* 148:165-175.

64. Frenette, P. S., S. Subbarao, I. B. Mazo, U. H. von Andrian, and D. D. Wagner. 1998. Endothelial selectins and vascular cell adhesion molecule-1 promote hematopoietic progenitor homing to bone marrow. *Proc Natl Acad Sci U S A* 95:14423-14428.
65. Dimitroff, C. J., J. Y. Lee, S. Rafii, R. C. Fuhlbrigge, and R. Sackstein. 2001. CD44 is a major E-selectin ligand on human hematopoietic progenitor cells. *J Cell Biol* 153:1277-1286.
66. Sackstein, R., J. S. Merzaban, D. W. Cain, N. M. Dagia, J. A. Spencer, C. P. Lin, and R. Wohlgemuth. 2008. Ex vivo glycan engineering of CD44 programs human multipotent mesenchymal stromal cell trafficking to bone. *Nat Med* 14:181-187.
67. Sipkins, D. A., X. Wei, J. W. Wu, J. M. Runnels, D. Cote, T. K. Means, A. D. Luster, D. T. Scadden, and C. P. Lin. 2005. In vivo imaging of specialized bone marrow endothelial microdomains for tumour engraftment. *Nature* 435:969-973.
68. Krause, D. S., K. Lazarides, U. H. von Andrian, and R. A. Van Etten. 2006. Requirement for CD44 in homing and engraftment of BCR-ABL-expressing leukemic stem cells. *Nat Med* 12:1175-1180.
69. Bevilacqua, M. P., J. S. Pober, D. L. Mendrick, R. S. Cotran, and M. A. Gimbrone, Jr. 1987. Identification of an inducible endothelial-leukocyte adhesion molecule. *Proc Natl Acad Sci U S A* 84:9238-9242.

70. Martens, C. L., S. E. Cwirla, R. Y. Lee, E. Whitehorn, E. Y. Chen, A. Bakker, E. L. Martin, C. Wagstrom, P. Gopalan, C. W. Smith, and et al. 1995. Peptides which bind to E-selectin and block neutrophil adhesion. *J Biol Chem* 270:21129-21136.
71. Ernst, B., and J. L. Magnani. 2009. From carbohydrate leads to glycomimetic drugs. *Nat Rev Drug Discov* 8:661-677.
72. Chapman, P. T., F. Jamar, A. A. Harrison, J. B. Schofield, A. M. Peters, R. M. Binns, and D. O. Haskard. 1996. Characterization of E-selectin expression, leucocyte traffic and clinical sequelae in urate crystal-induced inflammation: an insight into gout. *Br J Rheumatol* 35:323-334.
73. Bendas, G., A. Krause, U. Bakowsky, J. Vogel, and U. Rothe. 1999. Targetability of novel immunoliposomes prepared by a new antibody conjugation technique. *Int J Pharm* 181:79-93.
74. Funovics, M., X. Montet, F. Reynolds, R. Weissleder, and L. Josephson. 2005. Nanoparticles for the optical imaging of tumor E-selectin. *Neoplasia* (New York, N.Y 7:904-911.
75. Asgeirsdottir, S. A., R. J. Kok, M. Everts, D. K. Meijer, and G. Molema. 2003. Delivery of pharmacologically active dexamethasone into activated endothelial cells by dexamethasone-anti-E-selectin immunoconjugate. *Biochem Pharmacol* 65:1729-1739.

76. Tuerk, C., and L. Gold. 1990. Systematic evolution of ligands by exponential enrichment: RNA ligands to bacteriophage T4 DNA polymerase. *Science* 249:505-510.
77. Bunka, D. H., and P. G. Stockley. 2006. Aptamers come of age - at last. *Nat Rev Microbiol* 4:588-596.
78. Gragoudas, E. S., A. P. Adamis, E. T. Cunningham, Jr., M. Feinsod, and D. R. Guyer. 2004. Pegaptanib for neovascular age-related macular degeneration. *N Engl J Med* 351:2805-2816.
79. Rusconi, C. P., J. D. Roberts, G. A. Pitoc, S. M. Nimjee, R. R. White, G. Quick, Jr., E. Scardino, W. P. Fay, and B. A. Sullenger. 2004. Antidote-mediated control of an anticoagulant aptamer in vivo. *Nat Biotechnol* 22:1423-1428.
80. Quiram, P. A., T. S. Hassan, and G. A. Williams. 2007. Treatment of naive lesions in neovascular age-related macular degeneration with pegaptanib. *Retina* 27:851-856.
81. Guo, K. T., A. Paul, C. Schichor, G. Ziemer, and H. P. Wendel. 2008. CELL-SELEX: Novel Perspectives of Aptamer-Based Therapeutics. *Int J Mol Sci* 9:668-678.
82. Keefe, A. D., S. Pai, and A. Ellington. 2010. Aptamers as therapeutics. *Nat Rev Drug Discov* 9:537-550.
83. Nawrot, B., M. Boczkowska, M. Wojcik, M. Sochacki, S. Kazmierski, and W. J. Stec. 1998. Novel internucleotide 3'-NH-P(CH₃)(O)-O-5' linkage.

- Oligo(deoxyribonucleoside methanephosphonamidates); synthesis, structure and hybridization properties. *Nucleic Acids Res* 26:2650-2658.
84. Gryaznov, S. M. 1999. Oligonucleotide N3'-->P5' phosphoramidates as potential therapeutic agents. *Biochim Biophys Acta* 1489:131-140.
85. Lupold, S. E., B. J. Hicke, Y. Lin, and D. S. Coffey. 2002. Identification and characterization of nuclease-stabilized RNA molecules that bind human prostate cancer cells via the prostate-specific membrane antigen. *Cancer Res* 62:4029-4033.
86. Teng, Y., A. C. Girvan, L. K. Casson, W. M. Pierce, Jr., M. Qian, S. D. Thomas, and P. J. Bates. 2007. AS1411 alters the localization of a complex containing protein arginine methyltransferase 5 and nucleolin. *Cancer Res* 67:10491-10500.
87. Cao, Z., R. Tong, A. Mishra, W. Xu, G. C. Wong, J. Cheng, and Y. Lu. 2009. Reversible cell-specific drug delivery with aptamer-functionalized liposomes. *Angew Chem Int Ed Engl* 48:6494-6498.
88. Farokhzad, O. C., J. Cheng, B. A. Teply, I. Sherifi, S. Jon, P. W. Kantoff, J. P. Richie, and R. Langer. 2006. Targeted nanoparticle-aptamer bioconjugates for cancer chemotherapy in vivo. *Proc Natl Acad Sci U S A* 103:6315-6320.
89. Yang, X., H. Wang, D. W. Beasley, D. E. Volk, X. Zhao, B. A. Luxon, L. O. Lomas, N. K. Herzog, J. F. Aronson, A. D. Barrett, J. F. Leary, and D. G.

- Gorenstein. 2006. Selection of thioaptamers for diagnostics and therapeutics. *Ann N Y Acad Sci* 1082:116-119.
90. Volk, D. E., Power, T.D., Gorenstein, D.G. and Luxon, B.A. 2002. An ab initio study of phosphorothioate and phosphorodithioate interactions with sodium cation. *Tetrahedron Lett.* 43:4443–4447.
 91. Monteith, D. K., R. S. Geary, J. M. Leeds, J. Johnston, B. P. Monia, and A. A. Levin. 1998. Preclinical evaluation of the effects of a novel antisense compound targeting C-raf kinase in mice and monkeys. *Toxicol Sci* 46:365-375.
 92. King, D. J., S. E. Bassett, X. Li, S. A. Fennewald, N. K. Herzog, B. A. Luxon, R. Shope, and D. G. Gorenstein. 2002. Combinatorial selection and binding of phosphorothioate aptamers targeting human NF-kappa B RelA(p65) and p50. *Biochemistry* 41:9696-9706.
 93. King, D. J., D. A. Ventura, A. R. Brasier, and D. G. Gorenstein. 1998. Novel combinatorial selection of phosphorothioate oligonucleotide aptamers. *Biochemistry* 37:16489-16493.
 94. Somasunderam, A., V. Thiviyathan, T. Tanaka, X. Li, M. Neerathilingam, G. L. Lokesh, A. Mann, Y. Peng, M. Ferrari, J. Klostergaard, and D. G. Gorenstein. 2010. Combinatorial selection of DNA thioaptamers targeted to the HA binding domain of human CD44. *Biochemistry* 49:9106-9112.

95. Mann, A. P., A. Somasunderam, R. Nieves-Alicea, X. Li, A. Hu, A. K. Sood, M. Ferrari, D. G. Gorenstein, and T. Tanaka. 2010. Identification of thioaptamer ligand against E-selectin: potential application for inflamed vasculature targeting. *PLoS One* 5.
96. Tanaka, T., L. S. Mangala, P. E. Vivas-Mejia, R. Nieves-Alicea, A. P. Mann, E. Mora, H. D. Han, M. M. Shahzad, X. Liu, R. Bhavane, J. Gu, J. R. Fakhoury, C. Chiappini, C. Lu, K. Matsuo, B. Godin, R. L. Stone, A. M. Nick, G. Lopez-Berestein, A. K. Sood, and M. Ferrari. 2010. Sustained small interfering RNA delivery by mesoporous silicon particles. *Cancer Res* 70:3687-3696.
97. Landen, C. N., Jr., A. Chavez-Reyes, C. Bucana, R. Schmandt, M. T. Deavers, G. Lopez-Berestein, and A. K. Sood. 2005. Therapeutic EphA2 gene targeting in vivo using neutral liposomal small interfering RNA delivery. *Cancer Res* 65:6910-6918.
98. Serda, R. E., B. Godin, E. Blanco, C. Chiappini, and M. Ferrari. 2010. Multi-stage delivery nano-particle systems for therapeutic applications. *Biochim Biophys Acta* 1810:317-329.
99. Bevilacqua, M. P. 1993. Endothelial-leukocyte adhesion molecules. *Annu Rev Immunol* 11:767-804.
100. Tanaka, T., K. S. Suh, A. M. Lo, and L. M. De Luca. 2007. p21WAF1/CIP1 is a common transcriptional target of retinoid receptors: pleiotropic regulatory mechanism through RAR/RXR

heterodimer and RXR/RXR homodimer. The Journal of biological chemistry.

101. Shao, R., and X. Guo. 2004. Human microvascular endothelial cells immortalized with human telomerase catalytic protein: a model for the study of in vitro angiogenesis. *Biochem Biophys Res Commun* 321:788-794.
102. Ades, E. W., F. J. Candal, R. A. Swerlick, V. G. George, S. Summers, D. C. Bosse, and T. J. Lawley. 1992. HMEC-1: establishment of an immortalized human microvascular endothelial cell line. *J Invest Dermatol* 99:683-690.
103. Zuker, M. 2003. Mfold web server for nucleic acid folding and hybridization prediction. *Nucleic Acids Res* 31:3406-3415.
104. Ananta, J. S., B. Godin, R. Sethi, L. Moriggi, X. Liu, R. E. Serda, R. Krishnamurthy, R. Muthupillai, R. D. Bolskar, L. Helm, M. Ferrari, L. J. Wilson, and P. Decuzzi. 2010. Geometrical confinement of gadolinium-based contrast agents in nanoporous particles enhances T1 contrast. *Nat Nanotechnol* 5:815-821.

Vita

Aman Mann was born in Agra, India on July 7th, 1981. He grew up in India and attended high school at Air Force Golden Jubilee Institute and graduated from Indian Institute of Technology, Delhi in 2005 with the dual Bachelors and Masters degrees in Biochemical Engineering and Biotechnology. After graduation, he did an internship at M.D. Anderson Cancer Center from 2005-2006. In fall 2006, Aman matriculated into the Graduate School of Biomedical Sciences at the University of Texas Health Science Center in Houston. In May 2007, he joined the laboratory of Dr. Mauro Ferrari at the Department of Nanomedicine and Biomedical Engineering, where he developed drug carriers for targeted delivery.